Federico Simoni, BSc

PETROLOGICAL INVESTIGATION OF THE GFÖHL GNEISS; BOHEMIAN MASSIF, AUSTRIA

Master Thesis

Thesis prepared for the degree of
Master of Science

submitted at

Karl Franzens Universität, Graz

Supervisor

Ao.Univ.-Prof. Mag. Dr.rer.nat., Christoph Hauzenberger

NAWI Graz Geozentrum
Petrology & Geochemistry

Graz, April 2017

to my family

and Lenny

DANKSAGUNG - RINGRAZIAMENTI

Nach einem sechsjährigen Studium schaue ich zurück und verstehe zum ersten Mal, was ich am meisten schätze, die Zeit. Diese Zeit ist nichts anderes gewesen als eine Turnhalle, die mich vorbereitet hat in die hektische Welt mit Neugierde und Selbstbewusstsein geschleudert zu werden. Die Wissenschaft sowie das Leben hat mir in diesen Jahren immer wieder die Möglichkeit geboten was Neues zu lernen und mich für was Neues zu begeistern. Ich bedanke mich also bei der Geologie und bei all den Leuten die einen Teil von Ihrer Zeit mit mir und für mich geteilt haben. An diese Leute möchte ich mit Bescheidenheit meine Arbeit widmen. Danke an Herr Kurt Bischof und Anton Pock für die technische Hilfe und für die Unterhaltungen, die nach mehreren anstrengenden Stunden im Labor ein Hauch Entspannung gebracht haben. Danke möchte ich auch Frau Margaret Grasser sagen, die leise und zuneigungsvoll mein Büro heimeliger gemacht hat. Ich bedanke mich bei Jürgen Neubauer und Prof. Karl Ettinger, die mit mir stundelang am Raster und an der Mikrosonde gesessen sind. Danke Professor Ettinger für die präzisen und konstruktiven Erklärungen und Ratschläge, die Sie mir gegeben haben. Danke an Herr Georg Stegmüller, ein Beispiel wenn man auf Zuverlässigkeit und Hilfsbereitschaft kommt. Danke an meinem Betreuer Ao.Univ.-Prof. Mag. Dr.rer.nat. Hauzenberger, für die logistische Unterstützung und das wertvolle Wissen, das er mir überträgt hat. Danke an meinen Kommilitonen Sara Raič, Gerhald Raab, Marlene Löberbauer, Isabella Haas, Felix Rauschenbusch, Max Weiss, Paul Petschnig, Lukas Belohlavek, Jensarin Vivatpinyo (Jeeb), Monika Moni Doubrawa, Sebastian Wiesmair; ihr habt alle dazu beigetragen Österreich zu meiner zweiten Heimat zu machen. Danke an den bunten und vielfältigen Petrologen-Team, von euch hab ich am meisten gelernt: danke Dominik für deine unkomplizierte und selbstlose Hilfe, danke Christian für deine Freundschaft und deine sympatischen aufgeregten Manieren, danke Philipp; man hat ein bisschen an der Oberfläche kratzen müssen, aber du bist dann ein wertvoller und geschätzter Freund geworden. Hvala Dragan, stariji brat s Balkana. Danke Simon, abgesehen von 6 Jahren gemeinsames studieren und gegenseitiges motivieren bist du mein bester Freund, nun bleibt nur mehr übrig in der gleichen Stadt zu wohnen und dass wir zwei Geologie Professoren werden, “ce lo siamo meritato“. Danke Silvia, mit deiner authentischen Selbstlosigkeit und unendlichen Zärtlichkeit machst du mich zum besseren Mensch, ich liebe

dich und ich sag auch deinen wunderbaren Eltern Maria und Anton danke. Danke Rasputin, dank dir werde ich mein eigenes schreiendes und weinendes Baby fast angenehm finden.

Grazie di cuore alla mia famiglia, grazie a te papà, hai un carattere tutto da decifrare e a volte da sopportare ma quello che resta alla fine di tutto è che sei unico, nessuno ha la fortuna di avere un padre così e che così tanto fa per me; se ad un papà un figlio maschio vuole bene a prescindere a te mamma voglio bene per essere l´ affettuosa e vulcanica stella polare mia e di tutta la famiglia; troppo poco spesso vieni riconosciuta per tutto cio´ che fai e che sacrifichi; sappi che in cuor mio ammiro la tua umiltà e il tuo altruismo: nella Treccani sotto la definizione di “Mamma” dovrebbe stare Francesca Busini da Bolzano. Grazie a Riccardo e Roberta, che prima o poi mi consentiranno di nuovo di essere considerato un fratello, vi voglio bene e sappiate che conosco e sosterrò il potenziale che c'è in ognuno di voi. Grazie alla mia veneranda sorella pelosa Lenny. Grazie alla nonna che in questi anni mi ha fornito e mi fornisce di energia con i suoi manicaretti e con il suo incontenibile affetto e modo di fare. Grazie a tutti quelli che mi regalano e mi hanno regalato il loro tempo, da Bolzano a Padova, Graz, Praiano, Stati Uniti, Irlanda.

Grazie alle persone che hanno interessi e voglia di fare, grazie alle persone umili, generose e coerenti, è grazie a voi che farò del mio meglio per vivere a pieno e godermi questa vita e ora (per la gioia di mio padre), AVANTI!

Table of content

ABSTRACT

The Gföhl gneiss is a high-grade metamorphic unit within the Moldanubian Zone, which is assigned to the south eastern Bohemian Massif, representing the easternmost border of the Variscan Orogenic belt. The studied lithology crops out in the Waldviertel, northern area of Lower Austria (AUT) at the border with Czech Republic. This work presents a detailed petrological study which aims to constrain and complete the state of the art regarding the nature and petrogenetic features of the Gföhl gneiss. The obtained data comprise the results of field work, quantitative and qualitative petrographic analysis, the application of conventional geothermobarometric methods and thermodynamic modelling. Whole rock chemistry as well as major and trace elements of the Gföhl gneiss have been also evaluated and compared to the Moldanubian granulite to study their common tectonometamorphic history. The PT conditions recovered for the *grt+sil(ky)+kfs+pl+bt+qz* peak assemblage are ~800 °C and ~9 kbar. A slight gradient in pressure from north to south is indicated by the predominant occurrence of kyanite in the southern part and the presence of only fibrolite and sillimanite in the northern part. In the south sillimanite is partly replaced by kyanite where a well-developed foliation and biotite growth is observed. The widespread presence of hydrous retrograde phases (e.g. chlorite, sericite) indicates a late stage low T overprint. The obtained results of this study allow finally two genetic models for the Gföhl gneiss. A first scenario suggests that Gföhl gneiss and Moldanubian granulite share a common PT-evolution which has been obscured by a strong metamorphic overprint (carboniferous HP-UHT event, *Friedl, 2011*). A second model proposes a different PT path followed by the two lithologies which have been subducted at different depths. The exhumation to middle and upper crustal level (*Finger, 2007*) of both Gföhl gneiss and Moldanubian granulites develops then along the same retrograde path.

Keywords: Variscan Orogen, Bohemian Massif, Moldanubian Zone, Gföhl gneiss, Granulite facies

KURZFASSUNG

Innerhalb der Böhmischen Masse bzw. des Moldanubikums stellt der Gflöhler Gneis eine hochgradige Einheit dar, deren geotektonische Position als auch die Relation zu den darunter liegenden Granuliten nicht gänzlich geklärt ist. Der Gföhler Gneis ist primär im nördlichen Teil Niederösterreichs (AUT) und dem südlichen Teil von Jihočeský kraj (CZ) aufgeschlossen. Die hier vorliegende Arbeit stellt eine ausführliche petrologische Untersuchung dar, wofür insgesamt 76 Proben genommen wurden, welche petrographisch, mineralchemisch und geochemisch analysiert wurden. Mit Hilfe von GASP und Granat-Biotit-Plagioklas-Quarz Barometrie, sowie Ti- in Biotit, Zweifeldspat, Granat – Monazit und Xenotim - Monazit Thermometrie, und mittels thermodynamischer Modellierung wurde versucht die die PT Bedingungen und die geodynamische Entwicklung dieser Lithologie zu bestimmen. Für die peak-Mineralparagenese *grt+sil(ky)+kfs+pl+bt+qz* wurden ca. ~800 °C und ~9 kbar bestimmt. Der Vergleich von Haupt- und Spurenelemente von Gföhler Gneis und Moldanubischem Granulite weist auf einen gemeinsamen Protolith hin. Außerdem konnte ein Druckgradient von Nord nach Süd festgestellt werden, welcher durch den Ersatz von Kyanit durch Sillimanit gekennzeichnet ist. Eine spätere LT Überprägung wird durch das vermehrte Auftreten von hydrierten retrograden Phasen in der Mineralparagenese im nördlichen Teil belegt. Aus den hier gewonnen Resultaten werden zwei genetische Modelle für den Gföhler Gneis vorgeschlagen: ein mögliches Szenario ist dass, Gföhler Gneis und Moldanubischer Granulit die gleiche PT Geschichte erlebt haben und um ca. 340 Ma (*Friedl, 2011*) von einem HP/UHT Event überprägt wurden. Eine andere Möglichkeit wäre ein unterschiedlicher PT-Pfad der beiden Lithologien und Subduktion auf unterschiedliche Tiefen. Die anschließend gemeinsame Exhumierung auf mittleres bis oberes Krustenniveau (*Finger, 2007*) des Gföhler Gneis und der Moldanubischen Granulite erfolgte entlang des gleichen retrograden Pfades.

Schlagwörter: Variszische Orogenese, Böhmische Masse, Moldanubische Zone, Gföhler Gneis, Granulit Fazies

INTRODUCTION

The Gföhl gneiss of the Moldanubian Zone (south-eastern Bohemian Massif) is a well-known unit within the Moldanubian nappe stack in eastern Austria but lacks a modern petrological study. The present study is meant to give some deeper knowledge on the petrology of the Gföhl gneiss.

As already observed by previous authors (*Tollmann, 1982, Matura, 1976*) the Gföhl gneiss is always associated with occurrences of Moldanubian granulite to the west (*Fuchs, 1971, 1976*); *Fuchs & Matura* in 1980 reported of local similarities between the two lithologies with the occurrence of gneiss-like parts within the granulites and granulitic layers in the Gföhl gneiss.

The petrogenetic, as well as the structural relationship, between Gföhl gneiss and Moldanubian granulite represents one of the most interesting features of the area, and, at the same time, a matter of strong debate. Solving this key question would allow geologists to either find constraints to the already existing theories, or to rethink the geodynamics and petrochemical history of part of the south-eastern area of the Bohemian Massif.

The study area is located in north-eastern Austria, in the region of Lower Austria, in the so-called “Waldviertel”. It covers an area of approximately 60 km^2 which goes from the Danube close to the city of Krems an der Donau, to about 10 km north of the Czech Republic border (see Fig. 1). The Waldviertel represents one of the south-eastern portions of the Bohemian Massif, which is the easternmost part of the unmodified Variscan orogenic belt. Its landscape is mostly made of forests, hills and cultivated fields. The typical smooth shape of the reliefs combined with the presence of thick soils is due to erosional processes that affect the area since millions of years and justifies the difficulties encountered by geologists in finding fresh and unaltered outcrops.

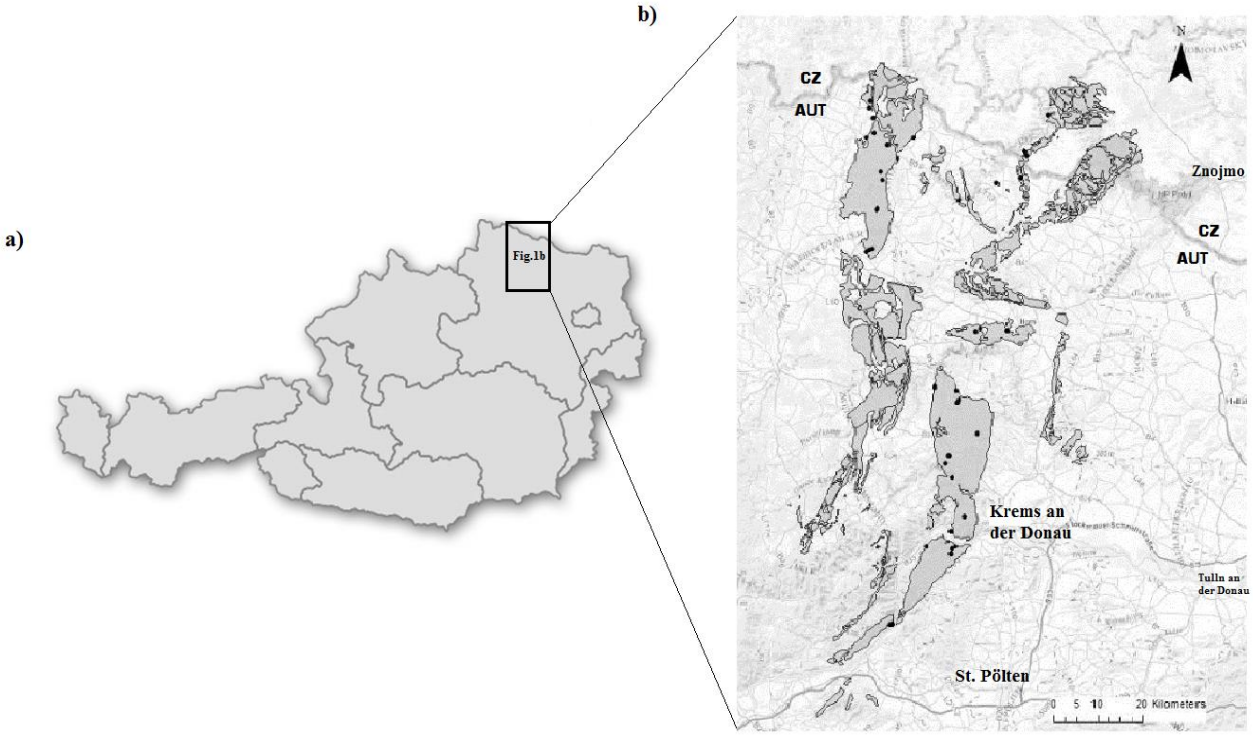

Fig. 1a-b a) Map of Austria indicating the studied area, b) shows the investigated gneiss bodies and sample locations (black dots).

GEOLOGICAL SETTING

Geodynamics

The Variscan orogenic belt stretches from the Appalachian (North America) in the west, to the Bohemian Massif in the east (Europe), resulting in an 8000 km broad and 1000 km wide discontinuous chain.

The entire orogeny evolves in early Ordovician (480 Ma) and lasts until the late Permian (250 Ma) (*Matte, 1986, 1991 & 2001; Burg et al., 1987; Ledru et al., 1989*).

In the early Paleozoic almost the whole continental crust present on the earth built up the supercontinent Gondwana. Between Laurentia and Baltica there were Avalonia and Armorica, intermediate continental microplates, formed by an Early Ordovician (480 Ma) detachment from Gondwana. The northward motion caused the progressive closure of the Iapetus Ocean between Avalonia, Laurentia and Baltica and the closure of its lateral branch (Tornqvist Ocean) between Avalonia and Baltica, leading to the collision and formation of a new continent: Laurussia (Fig. 2). The collision resulted in a belt formation called Caledonian orogeny in the Silurian (440Ma) (*Matte, 2001*).

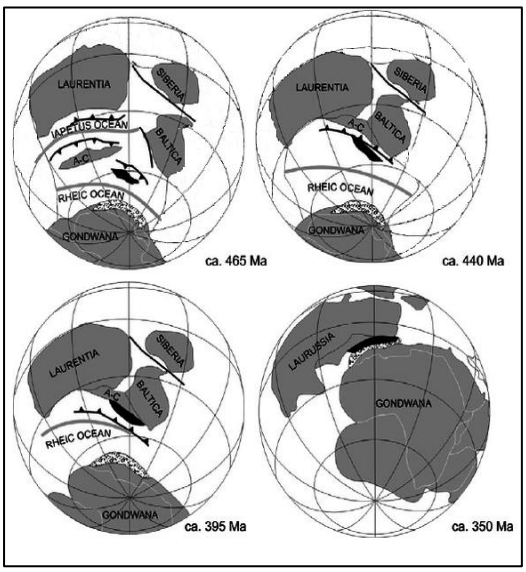

Fig. 2 Geodynamic sketch of the Early Palaeozoic. The black-filled continent is Armorica, A-C: Avalonia: (modified after Murphy, 2011). The portion of the sea between Avalonia and Baltica (465Ma) is the so-called Tornqvist Ocean (modified after Murphy, 2011).

Variscan Orogen

The southernmost part of Laurussia -Avalonia- and Armorica were divided by the Rheic Ocean. The closure of this ocean, accommodated by a bilateral subduction (*Franke 1984*), brought to the collision between Laurussia+Armorica -to the NW- and Gondwana -to the SE- leading to the Devonian Variscan orogeny.

The collision was followed by folding-, metamorphic-, intrusive- and uplift events that reached their maximum expression during the Carboniferous (*P.Matte, 2001*).

The closure of the Iapetus Ocean resulted also in the formation of the supercontinent Pangaea (300Ma). Between the early Jurassic (175 Ma) and late Cretaceous (60 Ma) Pangaea broke up leading to the current continental positioning.

Nowadays the Variscan belt can be distinguished based on its geographical position: the North-American- and the European Variscan belt.

The Appalachian and the Ouachita Mountains, along with areas with Variscan foldbelts such as New England, Nova Scotia and Newfoundland and Labrador represent the Variscan belt in USA and in Canada (*P. Matte, 2001)*

In Europe, the Variscan Belt includes a 3000 km-long chain that stretches from Portugal to the west through Spain, France (Brittany, Massif Central, Vosges and Corsica), Ireland, England, Germany (Harz and Black Forest) to Czech Republic and Austria in the Bohemian Massif (see Fig. 3), which represents the easternmost part of the belt (*Encyclopedia Britannica*).

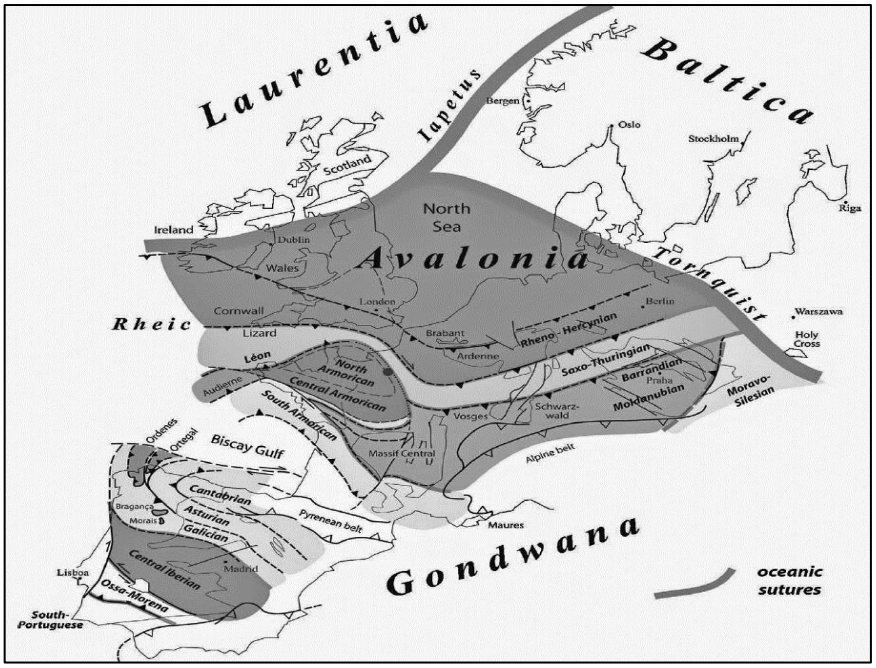

Fig. 3 Current subdivision of the main tectonic units of the Variscides in Europe. Detail of the Palaeozoic continents and suture zones (from Ballèvre, 2009).

Bohemian Massif - Moldanubian Zone

The eastern margin of the Bohemian Massif represents the metamorphic core of the Variscan Orogen and is made out of several basement segments that show substantial differences in age, lithology and metamorphic evolution (*Faryad, 2011*); the northernmost zone of the Bohemian Massif is the Saxo-Thuringian zone (*Kossmat, 1927*), that structurally belongs to the ATA (Armorican Terrane Assemblage) and consists mainly of Paleozoic pelagic and flysch sediments that were weakly metamorphosed during the Hercynian orogeny and of metamorphosed Ordovician MORB-type mafic rocks (*Franke, 2000*) (eclogite facies and MP metamorphic event, 395 Ma after *Dallmeyer et al., 1995,* 380 Ma from eclogites of Münchberg after *Stosch & Lugmair, 1990*). The southern part of the Saxo-Thuringian zone is characterized by the presence of massifs which expose felsic rocks and felsic to mafic rocks which have undergone HP to UHP (Saxonian Granulite Massif, Erzgebirge) dated at 340 Ma (*von Quadt, 1993*).The Saxo-Thuringian zone is delimited at south-east by the Teplá-Barrandian Zone made out of a well preserved Cadomian basement, Cambro-Ordovician intrusions (Central Bohemian Pluton) and metamorphic zones along with mantle rocks at its

northwestern and southeastern margin (Mariánská Lázně *eclogite complex, 365-380 Ma* after *Timmermann et al. 2004, Dallmeyer & Urban, 1998).*

The Teplá-Barrandian Zone is fault-bounded at south-east to the Moldanubian Zone, central unit of the Massif in which the studied Gföhl gneiss crops out. This zone will be discussed in detail further on.

At its easternmost part the Moldanubian zone is delimited by the Moravian Zone *(Suess, 1912, 1926).* This zone can be regarded as the western margin of a pre-Variscan block consolidated during the Cadomian Orogeny called Bruno-Vistulicum *(Dudek, 1980*) and comprises granitic bodies from the Cadomian plutonic suite and metasediments dated at 543 Ma *(Waldmann, 1951, Frasl, 1968, 1983).*

All the units and subunits which form the Bohemian Massif are tectonically bound by thrusts-system showing a predominant east-south-east vergence.

Although the characterization of the moldanubian units is still today a matter of debate *Dallmeyer et al.* (1995) and *Franke* (2000) subdivide in the most simplistic way the Moldanubian *s.s.* (*Finger et al.*, 2007) into three geological subunits: the Gföhl Unit at the top which overthrusts the Drosendorf Unit, which in turn lies on the overthrusted Ostrong Unit; this nappe system represents the pre-Variscan (Precambrian/Early Paleozoic) crust and was subsequently cut by Variscan intrusions (e.g. Durbachites, South Bohemian Batholith, 327-330 Ma after *Gerdes et al., 2003*) that are thought to be the result of delamination of the thickened lithospheric mantle during the Bavarian phase (330-315 Ma after Finger et al., 2007).

The Gföhl Unit is made of lower crustal rocks which underwent granulitic-facies metamorphism such as granulites s.s., orthogneisses, metasediments and mafic rocks; *(K. Petrakakis, 1997; Franke, 2000, P. Hasalova et al., 2007, Zeitlhofer et al., 2013)*.

The central Drosendorf Unit consists mainly of middle-grade metamorphosed rocks (up to amphibolite facies) formed in the middle crust namely orthogneisses (Dobra gneiss) and the so-called Variegated Series made out of amphibolites, metacarbonates (marbles), graphitic phyllites, quartzites and other mafic rocks.

The explanation for the high-grade Gföhl unit lying over the lower-graded Drosendorf unit is purely of tectonic nature: the Gföhl unit represents a nappe within the Bohemian thrust-system (see Fig. 4b) (*Finger, 2007*).

The lowest unit of the Moldanubian Zone is the Ostrong terrane (Fiala et al., 1995), which is also known in the older literature as Monotonous Series; the unit consists of migmatitic Grt-Bt-Sill paragneisses, orthogneisses, and amphibolites *(Hasalová et al., 2007)*. Although many authors refer to the Ostrong Terrane as an individual unit (*Faryad, 2010*), there are other authors that include it in a wider Drosendorf assemblage (*Seston et al., 2000*).

In this work a special focus is given to the Gföhl unit, in particular to one of its most occurring lithologies, i.e. the Gföhl gneiss.

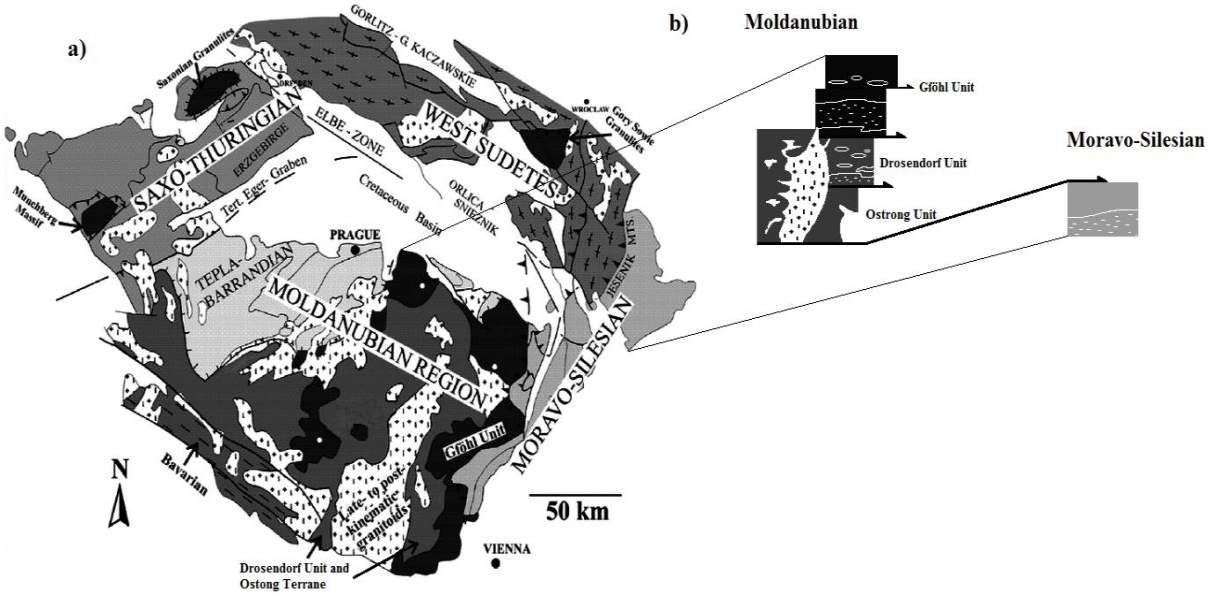

Fig. 4a-b a) General geological Map of the easternmost part of the Variscides, the Bohemian Massif (modified after *Faryad, 2010*). b) Focus on the stratigraphic section of the Moldanubian thrust system, which contains the Gföhl Unit including the studied lithology, the Gföhl Gneiss (Modified after *Linner, 2013*).

Gföhl Unit

The variety of the lithologies cropping out in the Moldanubian zone is reflected in the Gföhl unit, exhibiting rocks with different P-T-t histories that make the understanding of the petrogenesis and geodynamics of the unit not a trivial issue. Anyway, there is a main metamorphic episode represented by HT/HP metamorphosed felsic rocks (granulites) that have been equilibrated under lower crustal conditions *(Carswell & O´Brien, 1993, Cooke, 2000, Petrakakis, 1997, Kotkova, 2007, Zeitlhofer et al., 2013)*.

The structurally lower part of the Gföhl unit, the Raabs unit, is made out of rocks of sedimentary origin and a mafic protolith representing a Paleozoic oceanic domain between the Moravo-Silesian terrane and the remaining Moldanubian terrane that has undergone a medium-pressure metamorphism forming migmatitic gneiss and metasedimentary rocks intercalated by amphibolites and serpentinites (*Franke, 2000*). The overthrusting of the hot Gföhl subunits (*Timmerman, 2008*) onto the Raabs Unit led to a progressive increase of the metamorphic grade from the bottom to the top of the unit itself.

The Gföhl gneiss is made of high grade metamorphosed felsic rocks which protolith is an Ordovician granitoid (SHRIMP concordant zircon data, average 482±6 Ma, *Friedl et al., 1998*). The unit is represented mostly by one single lithology but its internal structure varies from massive to banded and in wide areas migmatic. The presence of migmatites points out to the partial melting of the rock due to high grade metamorphism. The Gföhl gneiss locally crops out along with HP-(UHP?)/UHT granulites that represent also the overlying unit of the whole Gföhl assembly. This so-called Moldanubian granulite occurs within the Moldanubian Zone as many isolated massifs (Dunkelsteiner Wald, St. Leonhard, Blumau, Blanský Les, Lišov, …) that have been interpreted to be klippen of an original extensive nappe (*Tollmann, 1995*).

ANALYTICAL TECHNIQUES

Fieldwork was conducted from spring till summer 2015 to collect samples for further petrological analysis. 65 samples were collected in the field whereas additionally 11 samples were further provided by successive expeditions in the study area.

The hand specimens were then reduced to polished thin sections and further analyzed under petrographic microscope using both transmitted- and polarized light microscopy. Quantitative mineral analyses (punctual measurements as well as mineral profiles and chemical mappings) were performed on selected representative carbon coated samples using a JEOL-JSM-6310 electron microscope provided with a LINK ISIS energy dispersive system and a MICROSPEC wavelength dispersive system. The facility was provided by the Institute of Earth Sciences, University of Graz, Austria.

In addition to that further analysis and 2D chemical mappings were made possible by the JEOL JXA-8200 electron microprobe from the Eugen Stumpfl Laboratory at the Montanuniversität of Leoben, Austria. The conditions of measurement were 6 nA at the Scanning Electron Microscope (SEM) and 12nA at the Electron Micro Probe Analyzer beam current per ca.1 µm beam diameter and 15 kV acceleration voltage. Standards purchased by the University were used for the calibration of the elements (for the standard used see Tab. 1).

For whole rock composition analysis 100g of every sample was crushed and prepared as glassy disk (“melt tab”). The major- and trace elements were measured by X-ray fluorescence with a WDXRF-spectrometer Bruke Pioneer S4.

The mineral abbreviations used for this work are after Whitney & Evans (2010) whereas in the equilibrium phase diagrams the mineral abbreviations used are after the thermodynamic data set of *Holland & Powell*, 1998.

Element	Standard	Location	Source	Reference
K, Si, Al	Adular		Naturhistorisches Museum Wien	
Ca, Ti	Titanite	Bundner Oberland	Collection, ETH-Zürich	Wori 1975 (SEMQ)
Mn	Rhodonite		Evans	
Fe, Mg	Garnet	Gore Mountain, Adiriondaks, New York	U.C. Berkeley	Levin, GSA Bull, 1960, 519-565
Cr	Chromite		U.S. Geological Survey	Analyst J.I. Dinnin
Na, Al, Si for Fsp	Albite			
Si, Al for Garnet	Almandine	Southern France		European Journal of Mineralogy 1995, 7, 187-194
Cl	Atacamite		Naturhistorisches Museum Wien	
F	synhetic F-Phlogopite		Bucher-Basel	Analyst Evans

Element	Standard	Location	Source	Reference
Ca	Plagioclase			
Na, Al, Si	Jadeite	China		
Ti	Titanite	Bundner Oberland	Collection, ETH-Zürich	Wori 1975 (SEMQ)
Mn	Rhodonite		Evans	
Fe, Mg	Garnet (Pyrope-Almandine)	Gore Mountain, Adiriondaks, New York	U.C. Berkeley	Levin, GSA Bull, 1960, 519-565
Fe	Bustamite	Broken Hill, N.S.W. Australia		
Cr	Chromite		U.S. Geological Survey	Analyst J.I. Dinnin
Na, Al, Si	Albite			
Fe, Al, Mg, Si	Almandine		New York State, USA	
Cl	Atacamite		Naturhistorisches Museum Wien	
	Benitoite	Benitoite Mine, San Benito Co. California	U.C. Berkeley	Louderback 1907 Bull Dep. Geol. U. Cal Vol. 5, p. 149-153 and 331-381
F,K, Mg	synhetic F-Phlogopite		Bucher-Basel	Analyst Evans
F	F-Topaz	Schneckstein		
K, Ba	Sanidin	Hohenfels, Germany		
Zr	Cubic Zircona			
Ce, Nd, La	Monazite			
Y	synthetic YAG	USA	Atomergic Chemetals Corp.	

Tab. 1a-b Standard used for a) SEM- and b) EPMA-analysis.

PETROGRAPHY AND MINERAL CHEMISTRY

Macroscopically most of the samples display a certain stage of weathering and are pale to grayish in colour, fine-grained with a coarse to well-developed foliation. The single minerals are mostly visible with the naked eye. The lighter bands and lenses include quartz, K-feldspar and plagioclase whereas the darker parts mostly comprise biotite. Garnets occur as porphyroblasts within the finer groundmass showing a partly irregular shape. Aluminum silicate grains are also occasionally visible. Some samples show the typical gneissic banding, due to the alternation of lighter and darker bands, some show a more massive texture. The rock exhibits recurrent intergrowth structures.

As described in the older literature and confirmed by the present study the Gföhl Gneiss is a fine-grained orthogneiss that shows the typical paragenesis of grt+sil (ky)+kfs+pl+bt+qz (see Fig. 5).

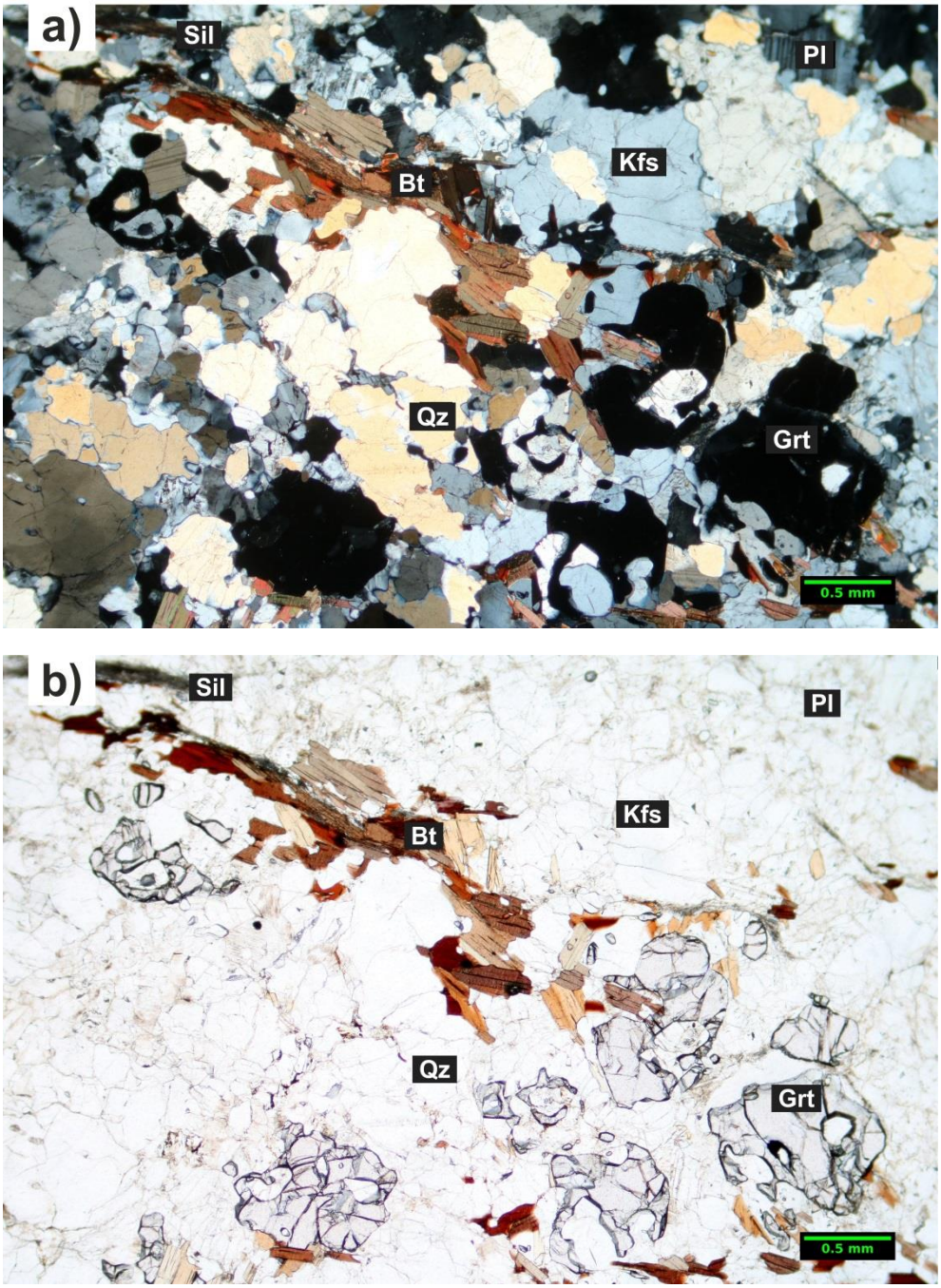

Fig. 5a-b Photomicrograph taken under the microscope on a) crossed and b) parallel Nicols showing the characteristic mineral assemblage of the Gföhl gneiss, Moldanubian Zone. Sample G96.

Garnet

Garnet shows a subhedral-euhedral shape and is characterized by a poikiloblastic texture and irregular cracks within the single grains. The size varies from more than 1mm (up to 5mm) for equilibrium garnets and less than 200 μm for recrystallized ones. Texturally stable garnets are almost absent; the approximate contours and irregular shape suggests a considerable resorption of the garnet by other phases or rapid growth along grain boundaries. The inclusions occupy in some cases greater parts of the core giving the garnet an atoll shape as shown by the first two images (sample G16a and G31) of Fig. 6. Inclusions such as apatite, quartz, K-feldspars and biotite occur with a higher frequency than rare-earth phosphates (monazite) and Fe-Ti-oxides (rutile, ilmenite).

Petrographic observations and mineral chemistry analysis did not allow identifying some kind of zoning pattern within the garnet although a slight variation in the Xgrs amount from core to the rim has been detected (sample G28_2 from Fig. 6, Fig. 7, Tab. 2). In garnet profile from sample G28_2 (Fig. 6) this variation can be more clearly observed; Xgrs measured at the core is 0.21 whereas at the rim is 0.42.

While garnet is frequently found in samples from the southern part of the investigated area (Danube valley), it was only rarely found in the northern part (close to Czech boundary). A more consistent sampling could be useful for determining an eventual decreasing trend from south to north.

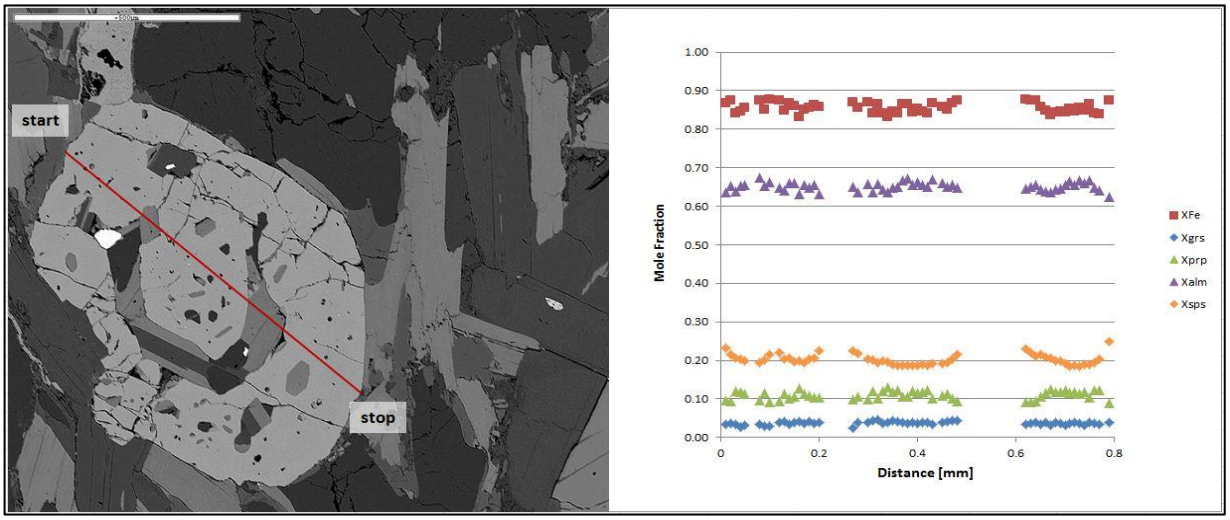
start
stop
Mole Fraction
Distance [mm]
XFe
Xgrs
Xprp
Xalm
Xsps

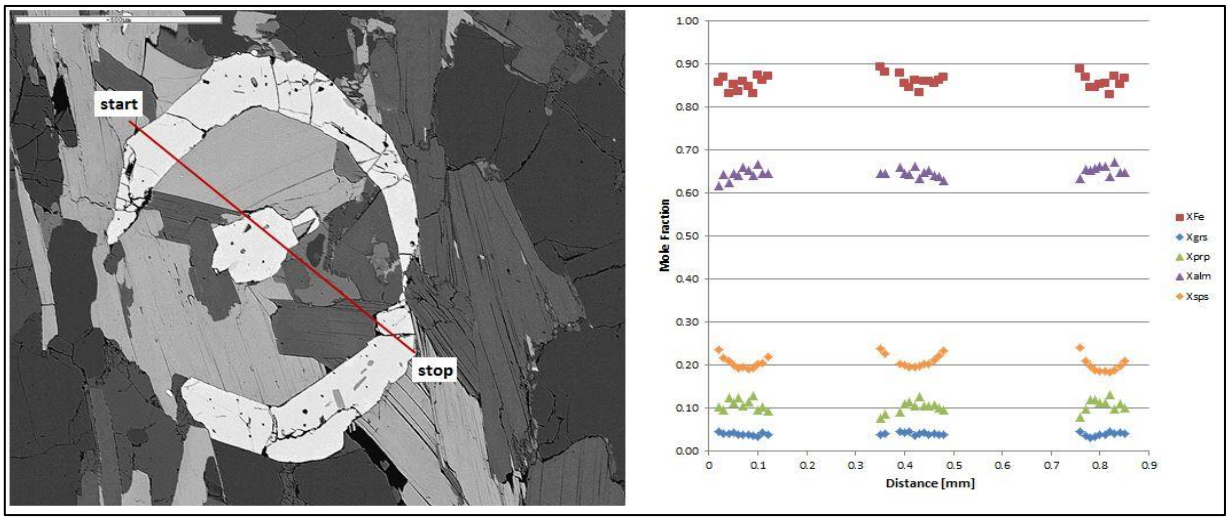
start
stop
Mole Fraction
Distance [mm]
XFe
Xgrs
Xprp
Xalm
Xsps

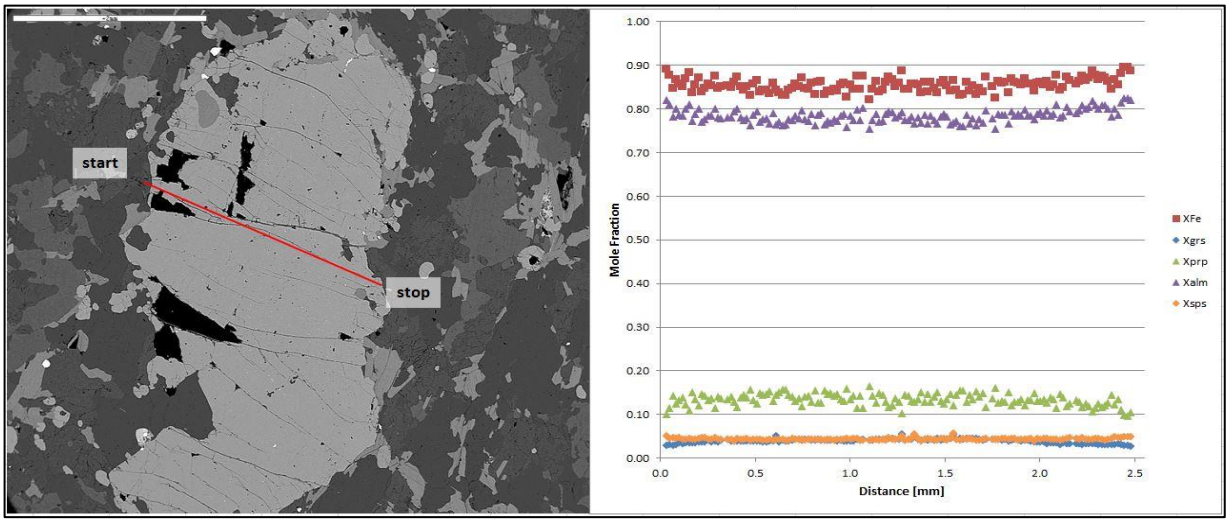
start
stop
Mole Fraction
Distance [mm]
XFe
Xgrs
Xprp
Xalm
Xsps

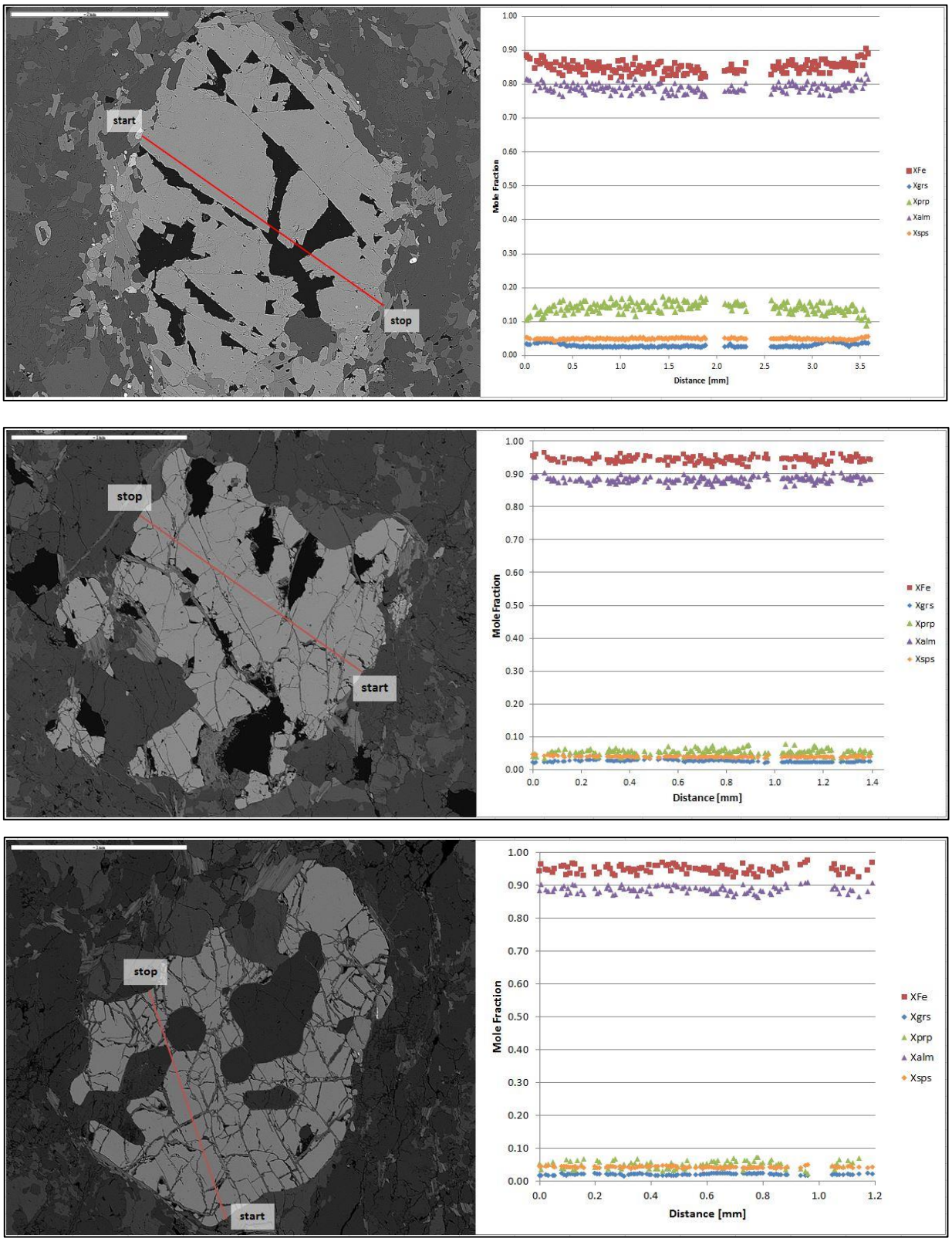

Fig. 6 BSE image of garnets from sample G16a (0.88 mm), G31 (0.96 mm) G28_1 (4.21 mm), G28_2 (3.82 mm), G6_1 (1.53 mm), G6_2 (1.95 mm) (from top of page 14 to bottom of present page). The thin red lines show the path followed by the compositional profile on the right

Tab. 2 Representative chemical analyses of garnets from Gföhl gneiss of the Moldanubian Zone.

sample	G1_1		G4_3		G8_3		G16a_1		G28_4		G31_2		G96_4		WG216_2		WG221_1	
position	core	rim	core	rim	core	rim	core	rim	core	rim	core	rim	core	rim	core	rim	core	rim
(wt%)																		
SiO2	36.26	36.60	35.23	35.67	37.60	37.48	36.86	36.30	37.54	37.42	37.09	36.60	36.59	36.78	37.89	37.02	36.82	36.94
TiO2	b.d.l.	b.d.l.	b.d.l.	b.d.l.	b.d.l.	b.d.l.	b.d.l.	b.d.l.	b.l.d.	b.l.d.	0.02	0.00	0.02	0.02	0.00	0.04	0.02	0.06
Al2O3	19.85	20.04	20.40	20.66	21.48	21.01	20.03	20.33	21.26	21.11	21.13	20.78	21.02	20.91	21.27	20.96	20.87	20.8
Cr2O3	b.d.l.	b.d.l.	b.d.l.	b.d.l.	b.d.l.	0.09	b.d.l.	b.d.l.	b.l.d.	b.l.d.	0.00	0.03	0.02	0.00	0.04	0.00	0.01	0.07
FeO	39.82	39.75	38.53	38.81	34.29	34.93	39.17	39.58	35.43	35.27	35.48	35.54	37.30	37.15	34.05	34.75	35.41	37.18
MgO	1.03	0.96	0.75	0.87	4.58	4.15	1.19	1.42	3.63	3.77	1.30	1.87	2.34	2.28	2.93	2.59	3.91	2.76
MnO	1.52	1.46	2.50	2.38	1.17	1.19	1.68	2.01	1.81	1.73	4.26	4.38	1.53	1.50	0.76	1.04	1.21	1.88
CaO	0.56	0.52	0.47	0.52	1.24	0.77	0.84	0.74	1.20	1.38	0.93	0.85	1.15	0.96	3.71	3.26	1.11	0.79
Total	99.04	99.33	97.88	98.91	100.36	99.62	99.77	100.38	100.87	100.73	100.21	100.05	100.00	99.62	100.68	99.67	99.36	100.48
(apfu) on the basis of 12 O																		
Si	3.010	3.027	2.959	2.962	2.986	3.010	3.030	2.964	2.990	2.982	3.012	2.980	2.967	2.995	3.013	2.990	2.972	2.979
Ti	0.000	0.000	0.000	0.000	0.000	0.000	0.000	0.000	0.000	0.003	0.001	0.000	0.001	0.001	0.000	0.002	0.001	0.004
Al	1.942	1.953	2.020	2.022	2.010	1.988	1.940	1.956	1.995	1.982	2.022	1.994	2.009	2.007	1.993	1.995	1.986	1.977
Cr	0.000	0.000	0.000	0.000	0.000	0.006	0.000	0.000	0.000	0.000	0.000	0.002	0.001	0	0.003	0.000	0.001	0.004
Fe2	2.726	2.749	2.645	2.640	2.259	2.346	2.693	2.587	2.334	2.302	2.409	2.377	2.475	2.528	2.264	2.325	2.324	2.454
Fe3	0.039	0.000	0.061	0.055	0.018	0.000	0.000	0.115	0.026	0.048	0.000	0.043	0.055	0.002	0.000	0.022	0.066	0.053
Mg	0.127	0.118	0.094	0.108	0.542	0.497	0.146	0.173	0.431	0.448	0.157	0.227	0.283	0.277	0.347	0.312	0.471	0.332
Mn	0.107	0.102	0.178	0.167	0.079	0.081	0.117	0.139	0.122	0.117	0.293	0.302	0.105	0.103	0.051	0.071	0.083	0.128
Ca	0.050	0.046	0.042	0.046	0.106	0.066	0.074	0.065	0.102	0.118	0.081	0.074	0.1	0.084	0.316	0.282	0.096	0.068
cations	8.001	7.995	8.000	8.000	8.000	7.993	8.000	8.000	8.000	8.000	7.976	8.000	7.996	7.997	7.991	8.000	8.000	8.000
Xgrs	0.017	0.015	0.014	0.016	0.035	0.022	0.024	0.022	0.034	0.039	0.028	0.025	0.034	0.028	0.026	0.094	0.032	0.023
Xalm	0.906	0.912	0.894	0.891	0.757	0.785	0.889	0.873	0.781	0.771	0.819	0.798	0.835	0.845	0.760	0.778	0.782	0.823
Xsps	0.036	0.034	0.060	0.057	0.026	0.027	0.039	0.047	0.041	0.039	0.100	0.101	0.035	0.034	0.017	0.024	0.028	0.043
Xprp	0.042	0.039	0.032	0.036	0.182	0.166	0.048	0.058	0.144	0.150	0.054	0.076	0.096	0.093	0.760	0.778	0.158	0.111
XMg	0.045	0.041	0.034	0.039	0.194	0.175	0.051	0.063	0.156	0.163	0.061	0.087	0.103	0.099	0.133	0.118	0.169	0.119
XFe	0.955	0.959	0.966	0.961	0.806	0.825	0.949	0.937	0.844	0.837	0.939	0.913	0.897	0.901	0.867	0.882	0.831	0.881

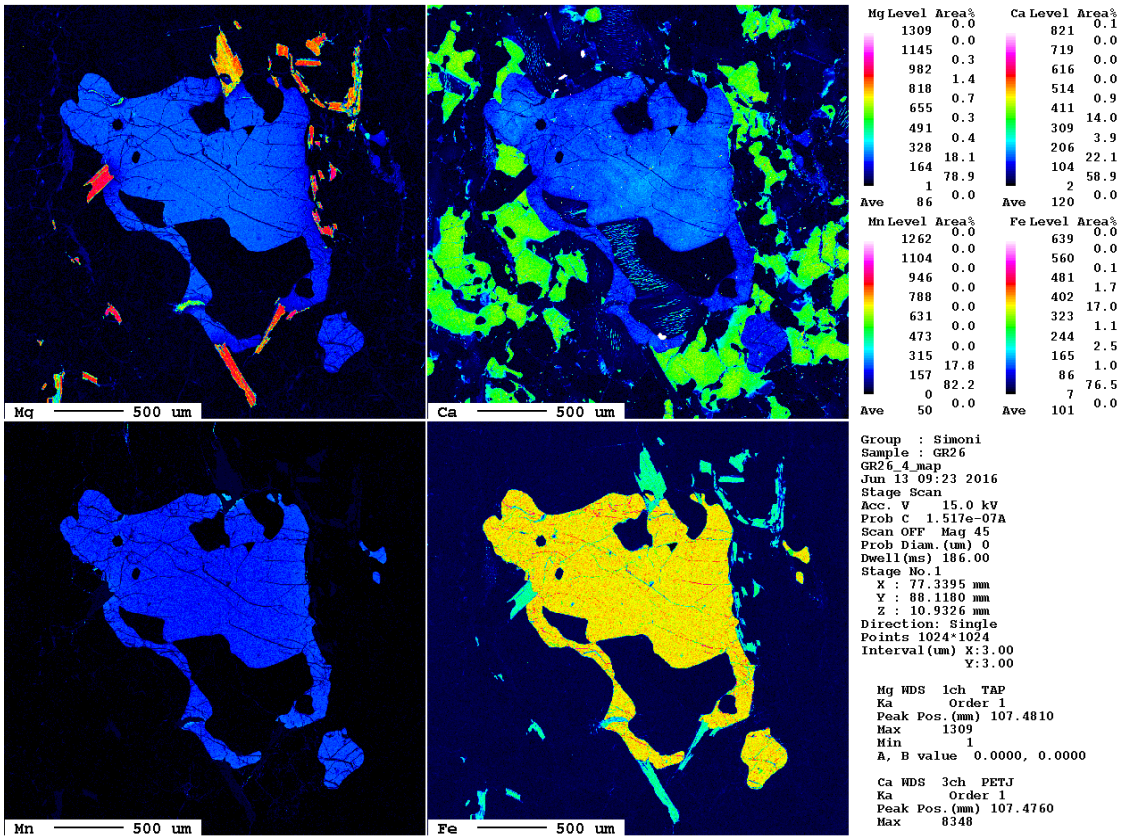

Fig. 7 Element distribution maps of Mg-Ca-Mn-Fe in a garnet crystal from sample G26. Note the slight variation of Ca distribution whereas the other elements show a more homogeneous pattern.

Feldspars and quartz

Feldspars together with quartz have an anhedral shape and make up the framework of the rock: a rough statistical analysis under the microscope suggests the K-feldspar to be the most recurrent Feldspar with a ratio of about 9:1 relative to plagioclase. K-feldspar as well as plagioclase can be found mainly as part of the matrix but can also appear as inclusion in garnet. Matrix feldspars are mostly fine- to middle grained (size up to 7mm) and exhibit subhedral habitus. K-feldspars show frequently their characteristic cross-hatched- twinning, which is typical for microcline, along with Carlsbad twinning; plagioclases are mostly identifiable based on the polysynthetic twinning (see Fig. 8a).

Perthites are also frequent and are mostly rather thin (≤7µm) and elongated. Exsolutions within K-feldspars occur typically during cooling. Due to decreasing temperature that doesn´t allow anymore the substitution of K (1.33Å) and Na (0.97Å) into the same crystal lattice, the ternary feldspar starts to form a K-rich- and a Na-rich phase (*Dutch, 1999*).

The presence of two generations of perthites differing in their crystallographic orientation (by 90°) (Fig. 8d) indicates that exsolution occurred at different temperatures during the retrograde cooling path of the Gföhl gneiss. Blebs of albitic plagioclase occur also as a kind of exsolution in K-feldspar (see Fig. 8b-c).

Mineral chemical analysis yield an average composition *of* $Xab_{0\text{-}0.22}$ -$Xan_{0\text{-}0.01}$ -$Xor_{0.75\text{-}0.93}$ for K-feldspar and $Xab_{0.65\text{-}0.90}$ -$Xan_{0.10\text{-}0.45}$ -$Xor_{0\text{-}0.2}$ for plagioclase (oligoclase). Gneisses sampled in the northern portion of the investigated area have higher anorthite components (Xan=0.45) in contrast to samples of the central and southern part which show a lower Xan (0.1-0.3) (see Fig. 9).

For chemical compositions see Tab. 3.

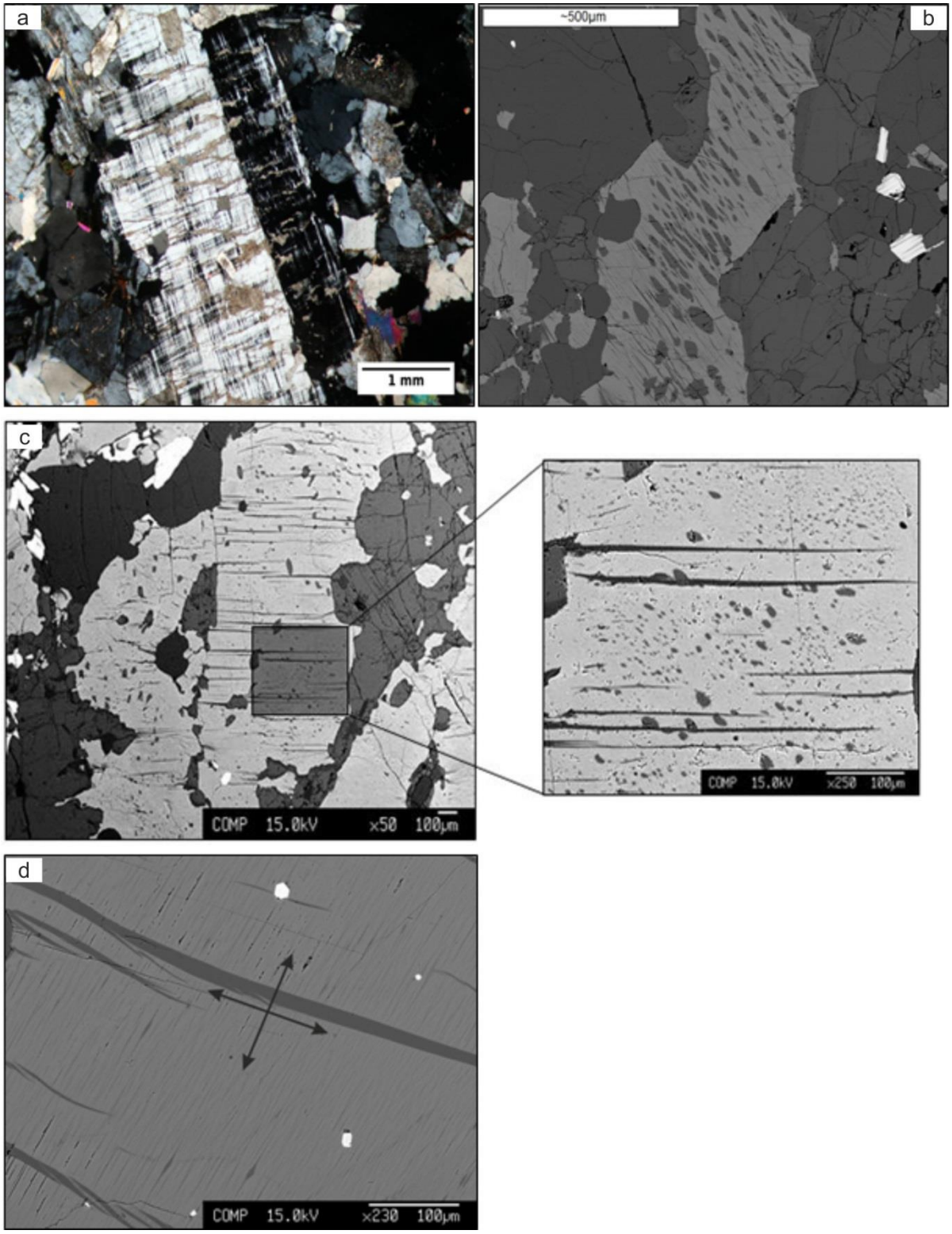

Fig. 8 a-b-c-d a) Detail of a K-Feldspar including both Carlsbad- and Microcline twinning, Sample G24. b) K-feldspars with iso-oriented perthitic exsolutions varying in size (from lamellae to blebs). Sample G26. c) EBS image of a K-feldspar showing perthitic exsolutions, heterogeneously distributed along the grain. The detail shows another type of exsolution characterised by tiny blebs of albitic plagioclase. Sample G26. d) Electron microprobe photo indicating two distinct generations of perthites forming an angle of 90° from each other. Sample G98.

Tab. 3 Representative chemical composition of feldspars from the Gföhl Gneiss.

sample	G8_2	G26_9	G28_4	G31_3	GG57_3	G8_1	G26_9	G28_4	G31_2_Plag	GG57_6
mineral-position	kfs-inclusion in grt	kfs-matrix	kfs-matrix	kfs-matrix	kfs-matrix	pl-perthite	pl-inclusion in kfs	pl-matrix	pl-matrix	pl-matrix
(wt%)										
SiO2	64.79	64.98	64.91	65.58	64.88	61.18	66.19	63.36	64.22	61.07
Al2O3	18.89	18.52	18.38	18.08	18.04	25.57	20.40	23.08	22.80	25.24
Fe2O3	0.22	b.d.l.	b.d.l.	b.d.l.	0.11	b.d.l.	b.d.l.	b.d.l.	b.d.l.	0.13
CaO	0.04	b.d.l.	0.07	b.d.l.	b.d.l.	5.76	1.63	3.89	3.34	6.92
Na2O	1.33	0.85	2.15	1.38	1.10	7.71	10.71	9.77	10.02	7.39
K2O	14.86	16.10	13.95	15.35	15.21	0.28	0.14	0.40	0.16	0.15
BaO	0.38	0.08	0.14	0.11	0.50	0.00	0.00	0.00		0.00
Total	100.51	100.53	99.60	100.50	99.86	100.50	99.07	100.50	100.54	100.90
(apfu) on the basis of 8 O										
Si	2.976	2.991	2.994	3.010	3.005	2.698	2.931	2.794	2.821	2.691
Al	1.023	1.005	0.999	0.978	0.985	1.329	1.065	1.200	1.180	1.311
Fe3	0.008	0.000	0.000	0.000	0.004	0.000	0.000	0.000	0.000	0.004
Ca	0.002	0.000	0.003	0.000	0.000	0.272	0.077	0.184	0.157	0.327
Na	0.118	0.076	0.192	0.123	0.099	0.659	0.920	0.835	0.853	0.631
K	0.871	0.945	0.821	0.899	0.899	0.016	0.008	0.023	0.009	0.008
Ba	0.007	0.001	0.003	0.002	0.009	0.000	0.000	0.000	0.000	0.000
cations	5.004	5.018	5.013	5.012	5.000	4.975	5.000	5.035	5.020	4.972
Xab	0.120	0.074	0.189	0.120	0.099	0.696	0.915	0.802	0.837	0.653
Xan	0.002	0.000	0.003	0.000	0.000	0.287	0.077	0.176	0.154	0.338
Xor	0.879	0.926	0.807	0.880	0.901	0.017	0.008	0.022	0.009	0.009

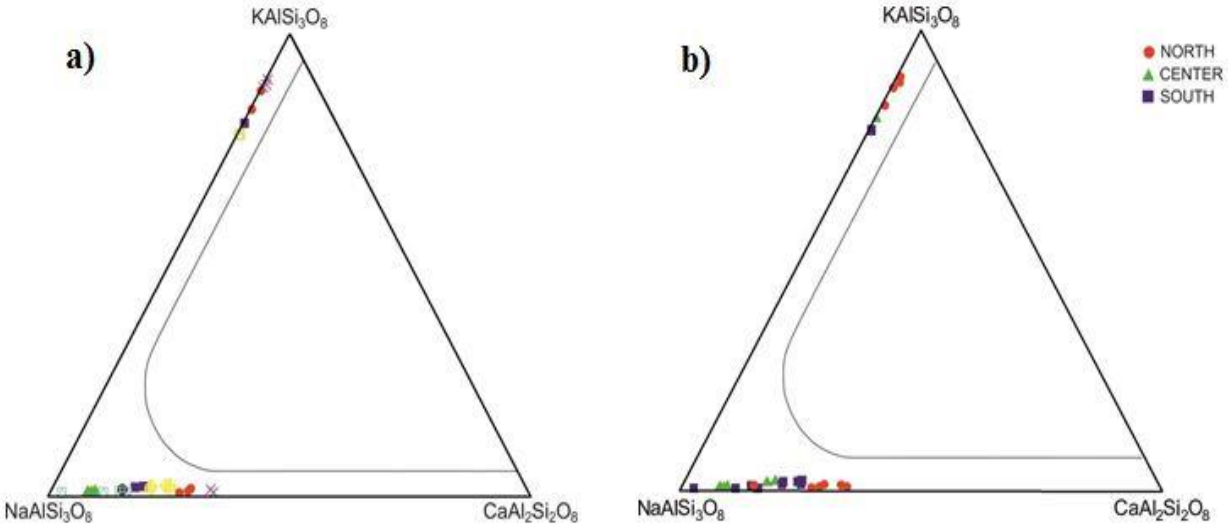

Fig. 9 Ternary classification diagrams Ab-An-Or representing (a) the composition of K-feldspar and plagioclase of samples from the study area. In (b) the plotted samples are labelled as a function of their spatial distribution

Aluminum silicates (kyanite/sillimanite)

Al-silicates also occur with varying abundances within the whole gneissic body. The most common Al-silicate is the high T-polymorph sillimanite, which occurs mostly in “clouds” of fibrous aggregates (fibrolite) or thin prismatic needles and less frequently as coarser subhedral-shaped prismatic crystals that reach up to 800µm. Kyanite is barely observed; it occurs only in the south of the Gföhl gneiss body with an euhedral habitus and the characteristic columnar shape (Fig. 10 and Fig. 12).

Fibrolite and fine grained prismatic sillimanite are observed in thin section partly oriented parallel to scistosity, partly growing perpendicular to the planes of scistosity; prismatic sillimanite also grows at the expense of kyanite (Fig. 11).

A handful of samples (G96, G98) from the south show some subhedral-euhedral crystals of kyanite in addition to sillimanite identified by their typical blue coloration (Fig. 10b).

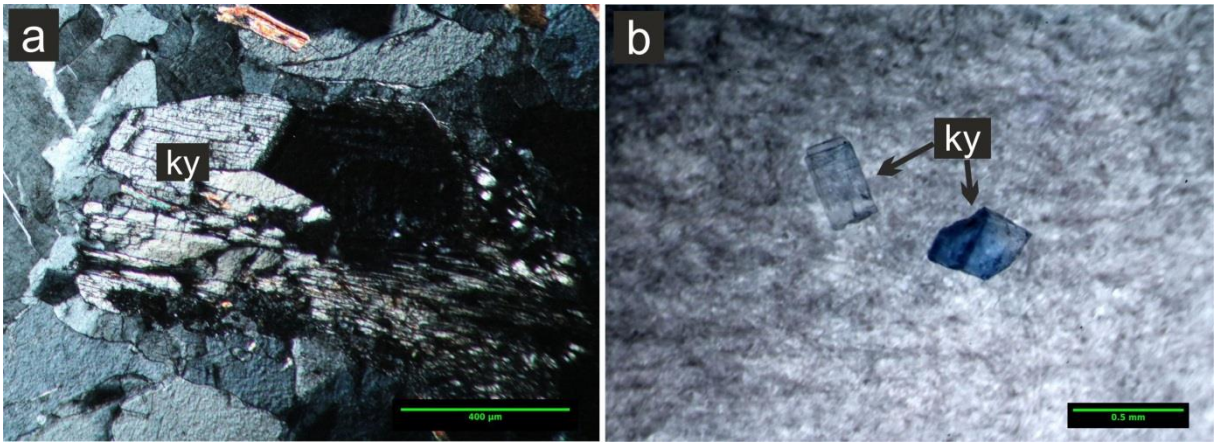

Fig. 10a-b Microphotographs of a) kyanite under thin section at crossed Nicols and of b) euhedral isolated crystals of kyanite taken from the south of the Gföhl gneiss-body near Mautern an der Donau. Notice the typical blue colouring. Sample G98.

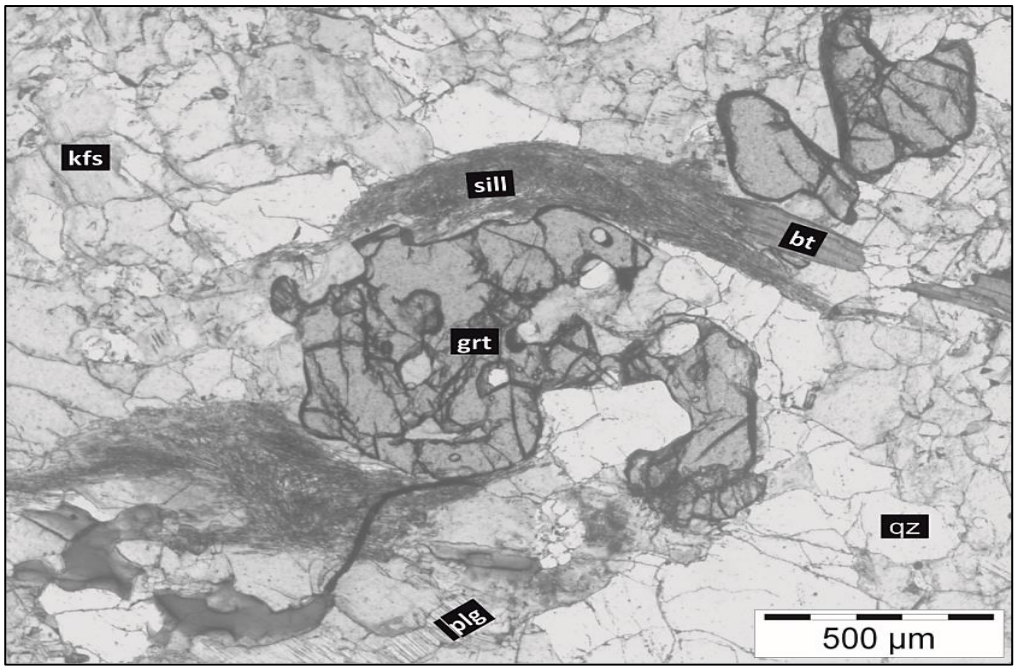

Fig. 11 Fibrous aggregates of sillimanite growing at the expenses of a garnet. In the picture the (retrograde and T°-dependent) reaction $\boldsymbol{Grt + kfs + H_2O \rightarrow Sill + bt + qz}$ is represented. Sample GG82

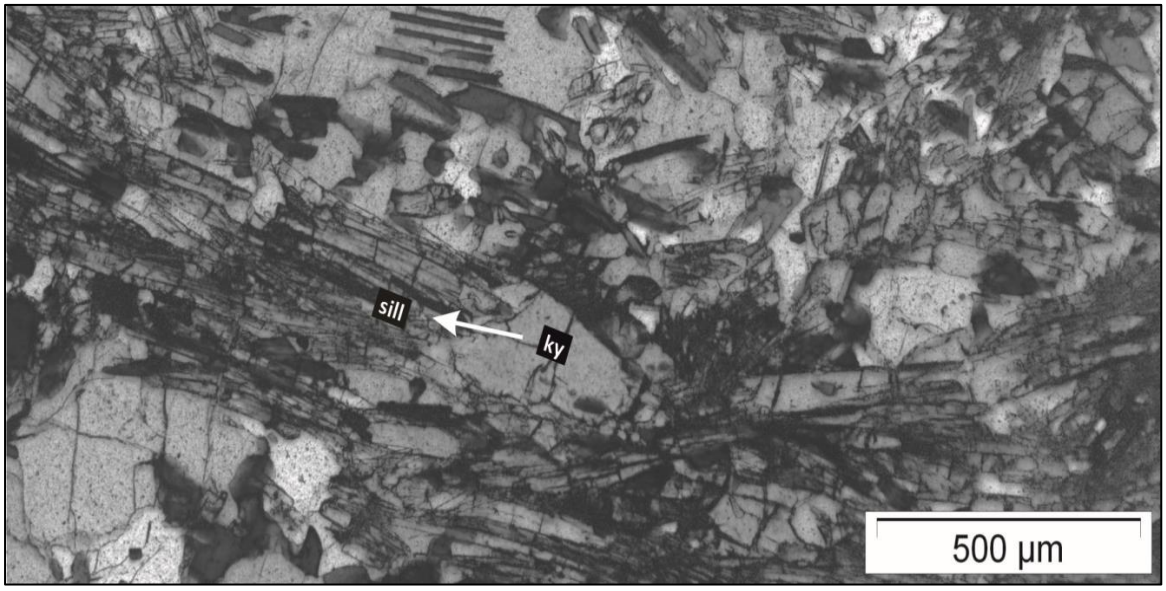

Fig. 12 Kyanite is decomposed by sillimanite. An example of decompression reaction from the southern sample WG221

Biotite

Biotite is the only mica building up the peak assemblage of the Gföhl gneiss and is usually oriented parallel to foliation. In some places it occurs also as isolated nests. The chemical composition of biotite is relatively homogeneous within samples but differs between samples with Xmg between 0.25 and 0.64, TiO2 values of 1-5.5 wt% and F (Tab. 4), which values ranges between 0.09 to 2.83 wt%. The Ti-richest samples were collected in the northern-central part of the study area (G28, GG57) whereas the samples from the south have basically lower Ti values. F doesn't indicate any trend from north to south. Fig. 13 shows the composition of biotite after a classification of Guidotti, 1984.

Muscovite and Chlorite

Muscovite and chlorite can be observed as retrograde phases as well as secondary alteration by a reaction with an aqueous fluid. Plagioclase frequently undergoes sericitization with the formation of fine grained muscovite (i.e. sericite) (Fig. 16).

Tab. 4 Representative chemical compositions of biotite from Gföhl gneiss.

sample	G4	G8	G16a	G28	G31	G96	GG57	GG82	WG216	WG219
(wt%)										
SiO2	34.87	35.57	35.01	35.22	33.88	34.18	36.53	35.01	37.77	35.13
TiO2	2.57	3.99	2.93	4.11	3.11	1.80	5.59	2.18	0.63	3.97
Al2O3	18.69	17.63	20.23	17.83	17.80	19.79	16.04	19.17	24.43	17.17
Cr2O3	0.06	0.00	0.04	0.08	0.05	0.00	b.d.l.	0.00	0.04	b.d.l.
FeO	25.03	17.79	20.71	21.26	21.11	22.91	13.47	21.73	17.73	21.52
MgO	4.59	10.13	7.59	7.03	7.82	7.22	13.41	6.55	6.26	8.10
MnO	0.01	b.d.l.	b.d.l.	b.d.l.	0.19	0.02	b.d.l.	b.d.l.	b.d.l.	b.d.l.
Na2O	0.08	0.08	0.06	0.10	0.16	9.58	0.09	0.07	3.51	0.07
K2O	9.50	9.60	9.44	10.00	9.68	0.07	9.99	9.61	4.91	9.74
F	2.83	0.90	b.d.l.	1.10	1.56	b.d.l.	0.49	2.25	b.d.l.	b.d.l.
Cl	0.48	0.13	b.d.l.	0.12	0.10	b.d.l.	b.d.l.	b.d.l.	b.d.l.	b.d.l.
Total	98.70	95.82	96.01	96.85	95.46	95.63	95.61	96.57	95.27	95.65
(apfu) on the basis of 11 O										
Si	2.727	2.708	2.657	2.710	2.666	2.643	2.724	2.725	2.762	2.705
Ti	0.151	0.228	0.167	0.238	0.184	0.105	0.313	0.128	0.035	0.230
Al	1.723	1.582	1.809	1.617	1.651	1.804	1.410	1.759	2.106	1.558
Cr	0.004	0.000	0.002	0.005	0.003	0.000	0.000	0.000	0.002	0.000
Fe2	1.637	1.133	1.314	1.368	1.389	1.482	0.840	1.414	1.084	1.385
Mg	0.535	1.150	0.859	0.806	0.918	0.832	1.490	0.760	0.682	0.930
Mn	0.001	0.000	0.000	0.000	0.013	0.001	0.000	0.000	0.000	0.000
Na	0.011	0.012	0.008	0.015	0.024	0.945	0.013	0.011	0.498	0.010
K	0.948	0.932	0.914	0.982	0.972	0.010	0.950	0.954	0.458	0.956
F	0.699	0.217	0.000	0.268	0.388	0.000	0.115	0.554	0.000	0.000
Cl	0.063	0.017	0.000	0.016	0.013	0.000	0.000	0.000	0.000	0.000
cations	7.738	7.979	7.731	7.740	7.821	7.828	7.740	7.751	7.627	7.771
Xmg	0.246	0.504	0.395	0.371	0.398	0.360	0.639	0.350	0.386	0.402

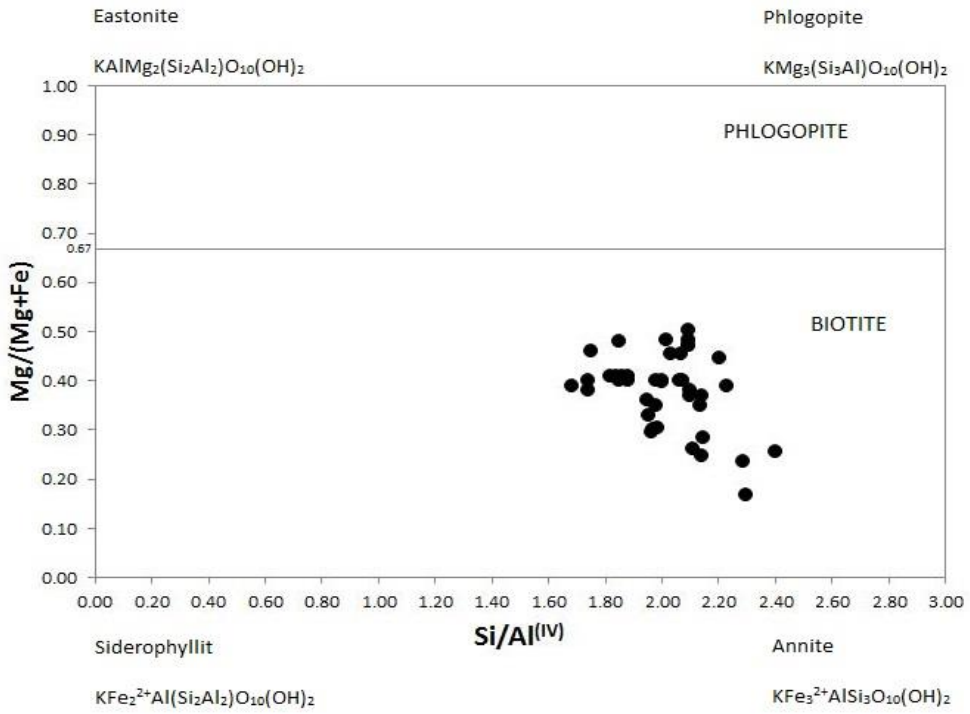

Fig. 13 Classification of biotite via Mg/(Mg+Fe) versus $Si/Al^{(IV)}$ diagram (modified after Guidotti, 1984).

Accessory phases

The accessory phases that have been observed are mostly apatite, zircon, monazite (along with its thorium end-member huttonite) (Fig. 14), pyrite, and oxides Phosphates occur in matrix as well as inclusions in feldspar, garnet and biotite and reach a maximum size of 1mm. Zircon and monazite produce typical pleochroic haloes in biotite crystals.

The identification of Ti-(Fe)-oxides in the peak assemblage allows qualitative pressure estimation where ilmenite occurs at lower pressures and rutile at elevated pressures. The small amount of Ti in the rock (~ 0.3 wt %) is incorporated in biotite leaving insufficient Ti for the formation of large ilmenite or rutile crystals. Anyway detailed petrography allowed to locate small crystals of rutile in the matrix and included in garnets. Ilmenite was observed exclusively as exsolution phase in biotite (i.e. not in equilibrium with the peak assemblage). X-ray powder diffraction analysis has been done in order to distinguish the Ti-oxides but failed since the peaks are too weak and got caught in the background noise.

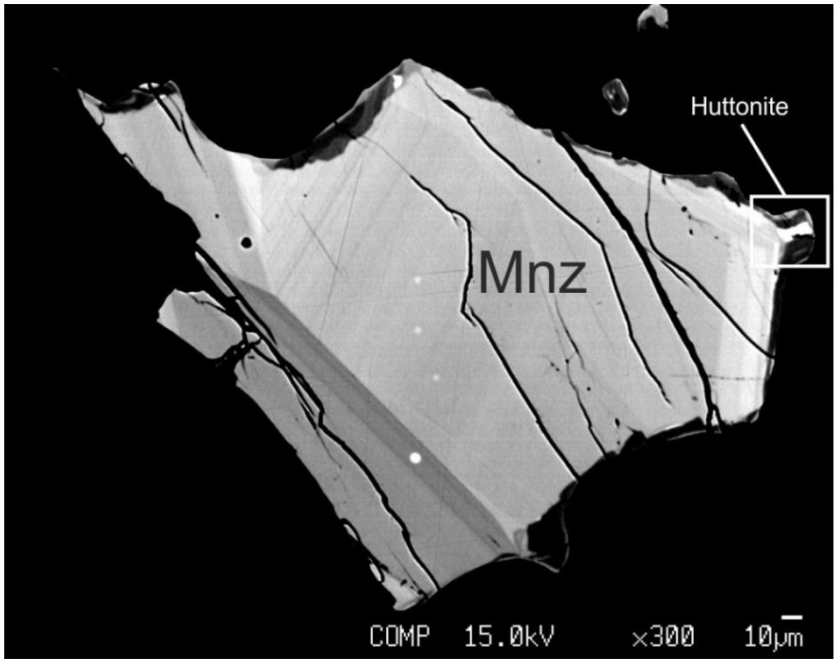

Fig. 14 BSE picture of a monazite with highlighted Th-silicate huttonite.

Melt related textures

As indicated above, recurring partial melting has affected the Gföhl gneisses as indicated by the occurrence of migmatised sections in the rock: at those positions the lighter parts (leucosomes) formed by mineral assemblages such as kalifeldspar, plagioclase and quartz are alternating to darker restites (melanosomes) formed in most cases by biotite. Many samples contain also other typical textures of partial molten rocks such as myrmekites, where rods of quartz are worm-like intergrown with plagioclase/K-feldspar (Fig. 15).

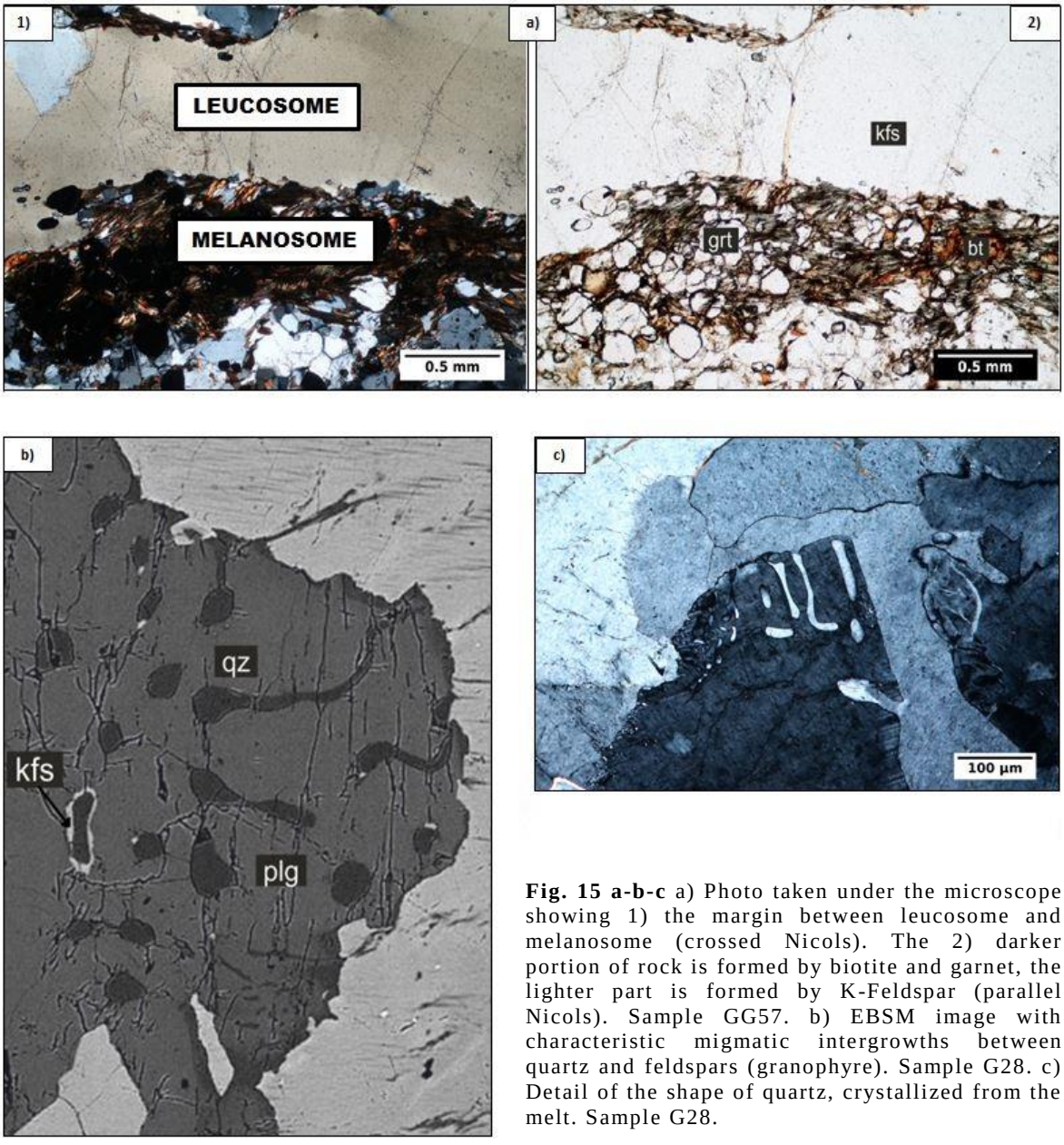

Fig. 15 a-b-c a) Photo taken under the microscope showing 1) the margin between leucosome and melanosome (crossed Nicols). The 2) darker portion of rock is formed by biotite and garnet, the lighter part is formed by K-Feldspar (parallel Nicols). Sample GG57. b) EBSM image with characteristic migmatic intergrowths between quartz and feldspars (granophyre). Sample G28. c) Detail of the shape of quartz, crystallized from the melt. Sample G28.

Late stage Overprint

The rocks from the north show a stronger retrograde overprint than the southern one as indicated by the higher occurrence of sericite and chlorite replacing feldspar and biotite/garnet, respectively (Fig. 16). Fluid infiltration during the retrograde path acts as a reaction booster facilitating retrograde metamorphism. One example is given in the northern-central part of the study area in which retrograde fibrolite grows recurrently at the expenses of garnet (Fig. 11) following the reaction:

$$sil + qz + bt \leftrightarrow grt + kfs + H_2O$$

Eq. 1

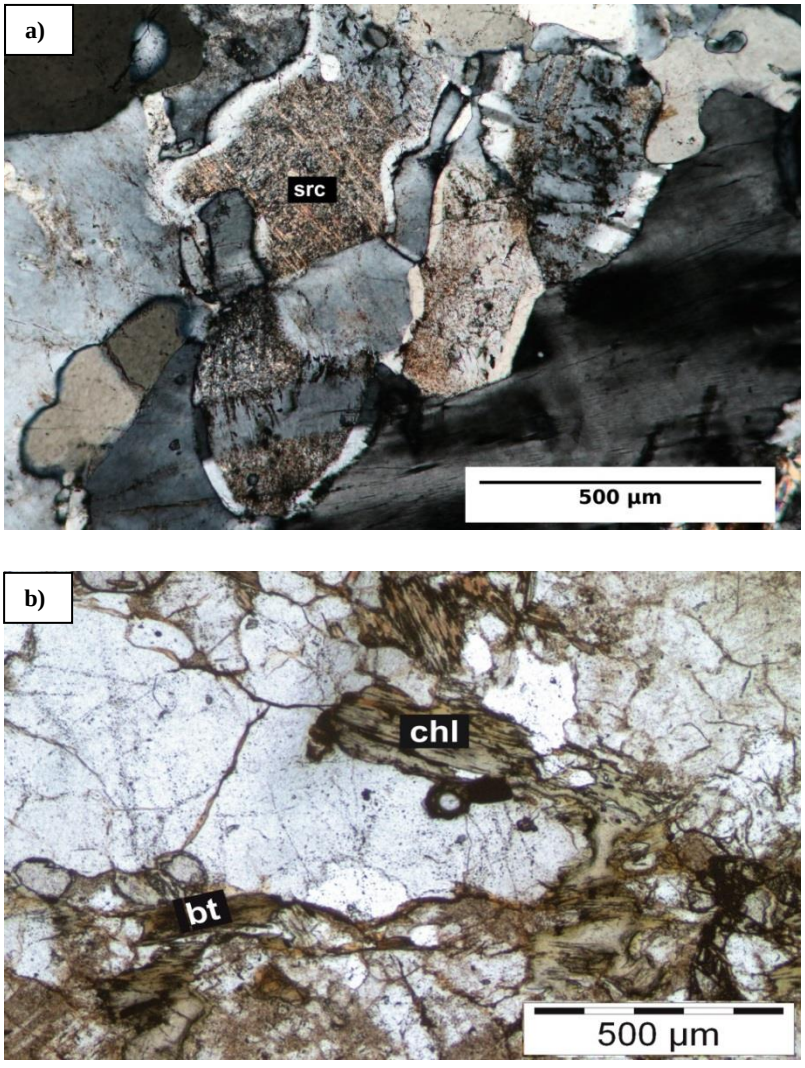

Fig. 16a-b Two examples of retrograde alteration patterns: chloritisation (a) and sericitization (b). Samples GG60 (a) and GG78 (b).

MAJOR- AND TRACE - ELEMENT WHOLE ROCK CHEMISTRY

Although there is still a certain grade of uncertainty about the ages of the moldanubian protolith (/s?) for the Gföhl gneiss (*Franke, 2000*), its petrologic nature is well known and has been confirmed over the years by the literature (*Tollmann, 1982, Matura; 1976, 2003*).

In order to obtain additional geochemical data for characterizing the Gföhl gneiss, especially its relationship with the overlying granulites 20 different samples have been analyzed by XRF (X-Ray Fluorescence Analysis). The data collected show consistent results relative to the older ones;

The protolith of the Gföhl gneiss is a fractionated subalkaline granite-granodiorite with SiO_2-content ranging between 65.68 and 76.45 wt% (Fig. 17). The AFM diagram (*Irvine & Baragar, 1971*) shows a calc-alkaline trend which is underlined in the Harker diagrams by a decrease in major elements TiO_2, Al_2O_3, MgO and CaO with ongoing fractionation (increasing SiO_2) (Fig. 18 and Tab. 5). Regarding the trace elements incompatible Rb shows a positive correlation with increasing SiO_2 whereas Ba and Sr indicate a negative scattered correlation with increasing SiO_2, as they were incorporated in crystallizing feldspars. Ce and Nd show also a decreasing trend with increasing SiO_2 content since they are incorporated in phosphates (apatite and monazite). Zr also shows a negative correlation with increasing SiO_2 pointing out at a conspicuous zircon fractionation (Tab. 6). K/Rb values indicate typical crustal level (~0.023).

Loss on ignition (LOI) shows values between 0.32 and 2.05%.For further compositions see. Tab. 7.

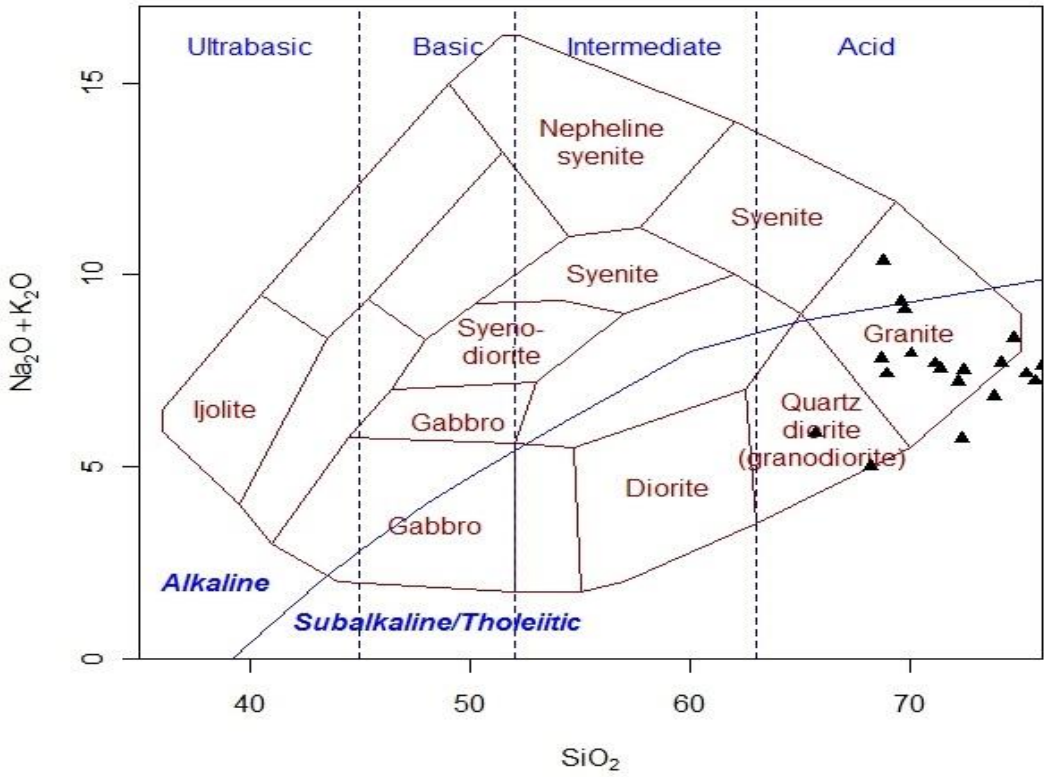

Fig. 17 TAS diagram after Cox et al., 1979

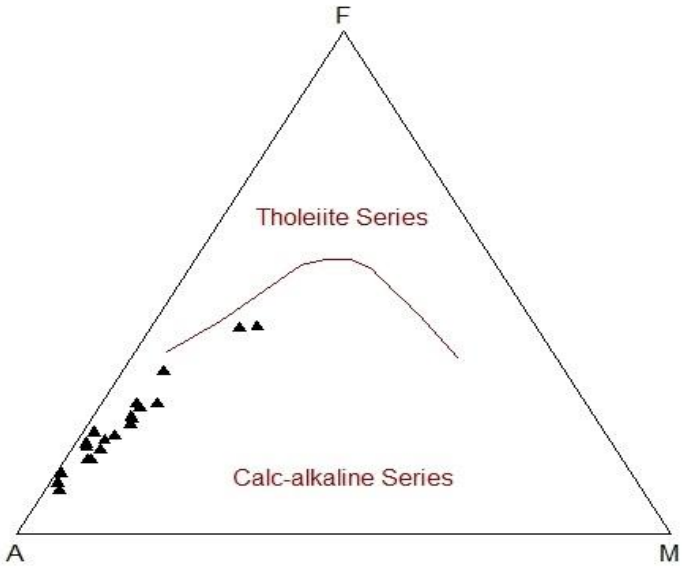

Fig. 18 AFM diagram after Irvine and Baragar, 1971.

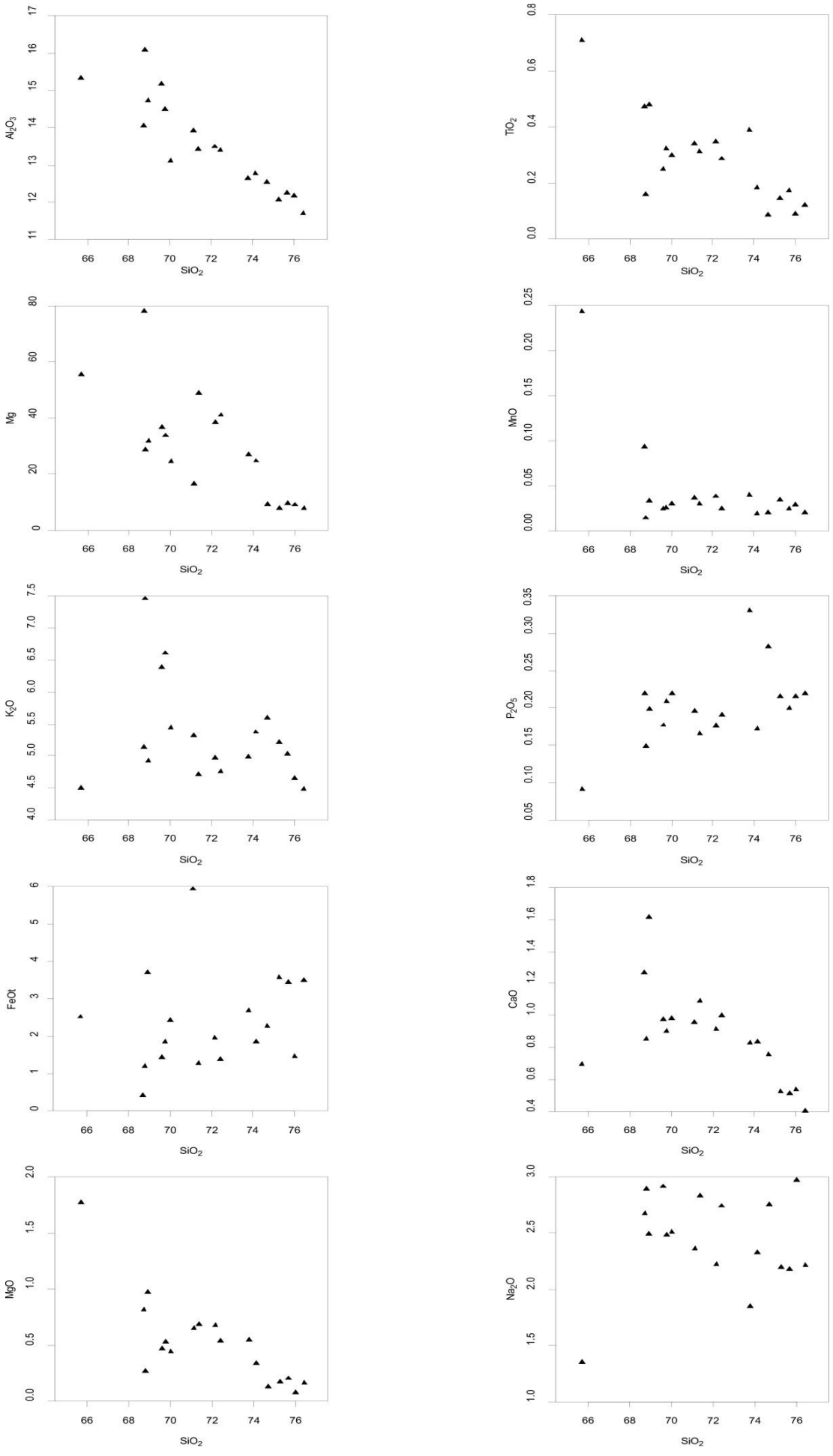

Tab. 5 Binary diagrams showing SiO2 versus major element oxides (wt %)

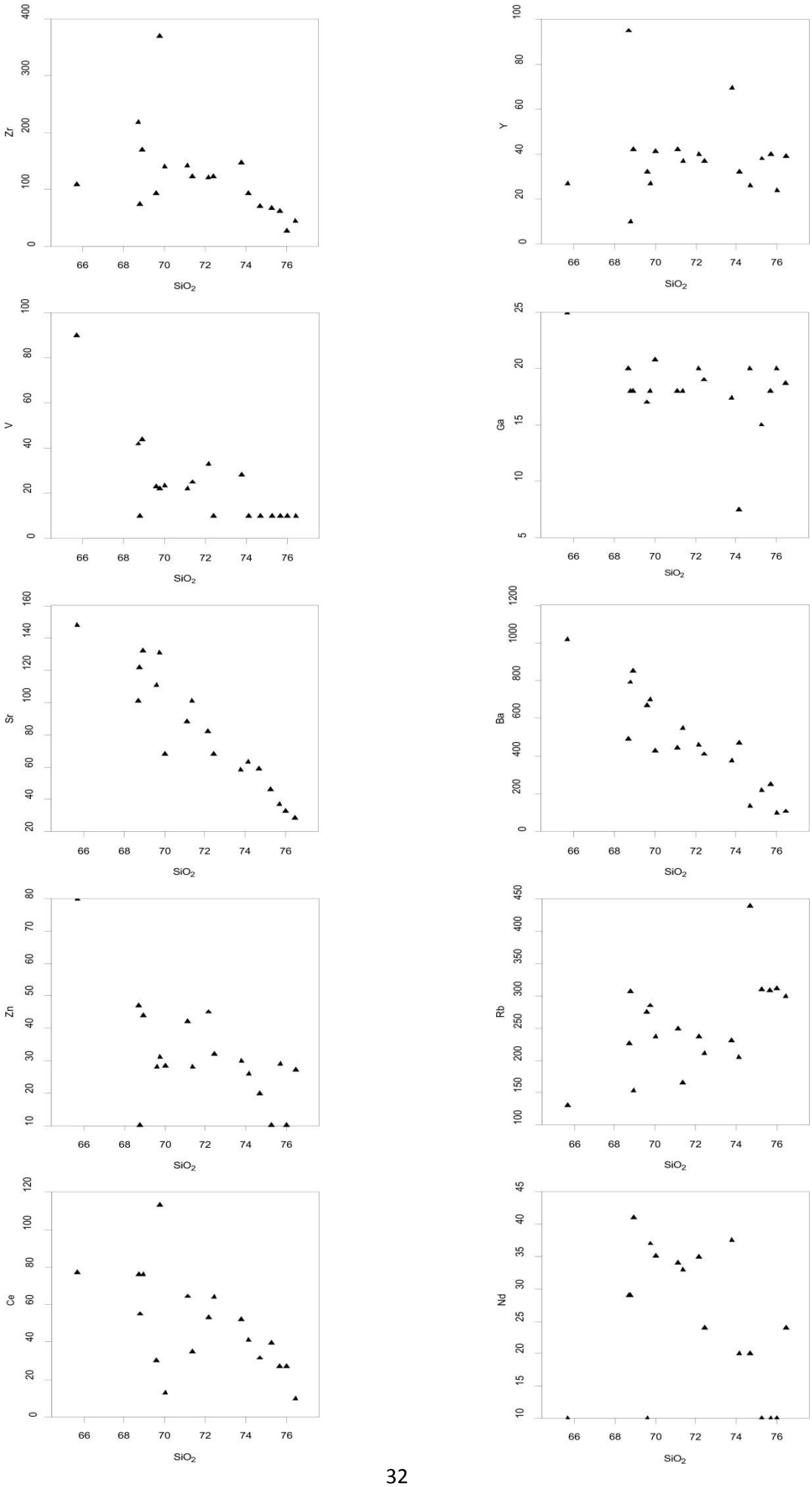

Tab. 6 Binary diagrams showing SiO_2 versus selected trace elements.

Tab. 7 Whole rock geochemical data of samples from the Gföhl gneiss homogeneously distributed along the study area.

sample	G1	G4	G6	G8	G16a	G24	G25	G26	G28	G30	G31	G33	GG57	WG215	WG216	WG217	WG219	WG221	G96	G98
(wt%)																				
SiO_2	76.45	75.68	75.27	68.92	65.68	72.33	74.69	76.01	68.71	74.14	72.43	71.37	68.17	71.12	69.76	69.60	68.78	72.16	70.02	73.78
TiO_2	0.12	0.18	0.15	0.48	0.71	0.28	0.09	0.09	0.47	0.18	0.29	0.31	0.67	0.34	0.32	0.25	0.16	0.35	0.30	0.39
Al_2O_3	11.70	12.26	12.06	14.74	15.34	13.85	12.55	12.18	14.05	12.77	13.40	13.43	14.24	13.94	14.49	15.19	16.09	13.49	13.12	12.64
FeOt	2.26	1.85	1.44	1.19	3.50	1.46	1.86	1.38	1.28	0.41	3.44	3.58	1.95	2.52	3.71	5.94	2.42	2.68	2.12	2.84
MnO	0.02	0.02	0.03	0.03	0.24	0.03	0.02	0.03	0.09	0.02	0.02	0.03	0.08	0.04	0.03	0.02	0.01	0.04	0.03	0.04
MgO	0.17	0.20	0.17	0.98	1.77	0.53	0.13	0.08	0.82	0.34	0.54	0.69	1.92	0.65	0.53	0.47	0.27	0.68	0.44	0.55
CaO	0.40	0.51	0.52	1.61	0.70	2.16	0.76	0.54	1.27	0.84	1.00	1.09	2.30	0.96	0.90	0.98	0.86	0.91	0.98	0.83
Na_2O	2.21	2.18	2.19	2.49	1.36	3.99	2.75	2.97	2.68	2.33	2.74	2.83	2.24	2.36	2.48	2.91	2.89	2.22	2.51	1.85
K_2O	4.48	5.04	5.22	4.92	4.50	1.73	5.60	4.66	5.14	5.38	4.77	4.71	2.76	5.32	6.61	6.39	7.46	4.98	5.45	4.98
P_2O_5	0.22	0.20	0.22	0.20	0.09	0.18	0.28	0.22	0.22	0.17	0.19	0.17	0.08	0.20	0.21	0.18	0.15	0.18	0.22	0.33
H_2O^+/LOI	0.92	0.43	0.74	0.60	2.05	0.86	0.56	0.53	0.39	0.50	0.60	1.04	0.68	0.58	0.59	0.41	0.32	0.49	0.54	0.54
Total	98.76	98.58	98.56	98.46	98.59	98.18	98.59	98.58	98.57	98.37	98.41	98.42	98.82	98.54	98.34	98.49	98.35	98.65	96.01	98.41
(ppm)																				
Ba	107	251	217	853	1017	130	138	97	492	472	410	549	883	444	701	667	791	458	430	378
Cr	<20	<20	<20	<20	59	<20	50	<20	<20	<20	<20	<20	60	<20	<20	<20	<20	51	<20	<20
Cs	<20	32	<20	<20	<20	<20	<20	<20	<20	<20	<20	<20	<20	<20	<20	<20	<20	<20	<20	<20
Cu	<20	<20	<20	<20	38	<20	<20	<20	<20	<20	<20	<20	<20	<20	<20	<20	<20	<20	<20	<20
Ga	19	18	15	18	25	19	20	20	20	<15	19	18	15	18	18	17	18	20	21	17
La	28	<20	26	50	51	29	14	14	20	27	51	<20	<20	31	52	24	41	38	69	79
Nb	<20	<20	<20	<20	<20	<20	<20	<20	<20	<20	<20	<20	<20	<20	<20	<20	<20	<20	<20	<20
Nd	24	<20	<20	41	<20	<20	20	<20	29	20	24	33	<20	34	37	<20	29	35	35	38
Ni	<20	<20	<20	<20	<20	<20	<20	<20	<20	<20	<20	<20	<20	<20	<20	<20	<20	<20	<20	<20
Pb	<20	20	<20	<20	<20	<20	<20	<20	<20	21	26	<20	<20	<20	<20	25	28	<20	<20	<20
Rb	299	308	310	153	131	104	440	311	227	205	211	165	58	249	285	275	307	237	238	231
Sc	<20	<20	<20	<20	<20	<20	<20	<20	20	<20	<20	<20	<20	<20	<20	<20	<20	<20	<20	<20
Sr	29	37	46	132	148	72	59	33	101	63	68	101	256	88	131	111	122	82	68	58
Th	<20	21	<20	20	<20	22	<20	<20	20	<20	<20	<20	<20	20	30	<20	<20	<20	<20	<20
U	<20	<20	<20	<20	<20	<20	<20	<20	<20	<20	<20	<20	<20	<20	<20	<20	<20	<20	<20	<20
V	<20	<20	<20	44	90	<20	<20	<20	42	<20	<20	25	74	22	22	23	<20	33	23	28
Y	39	40	38	42	27	31	26	24	95	32	37	37	27	42	27	32	<20	40	41	70
Zn	27	29	<20	44	80	29	20	<20	47	26	32	28	42	42	31	28	<20	45	28	30
Zr	44	62	67	169	109	90	70	27	219	93	123	122	227	142	369	93	73	120	140	147

It has been initially thought that the migmatization of the rock could have led to a change in its chemistry resulting in the different observed mineral paragenesis since garnet and Al_2SiO_5-phases don´t occur everywhere within the gneissic body. The partial melting of a rock presumes a melt extraction from the system, where possible, that could modify its original chemical composition. For this reason the whole rock chemistry of a series of migmatised samples has been compared to that of non-migmatic ones (Tab. 8). The chemical composition of both sample types is similar indicating that melt extraction did not play an important role during migmatization.

	MIGMATISED			NON-MIGMATISED		
sample	G8	G24	G26	WG216	WG221	G96
(wt%)						
SiO2	68.92	72.33	76.01	69.76	72.16	70.02
TiO2	0.48	0.28	0.09	0.32	0.35	0.3
Al2O3	14.74	13.85	12.18	14.49	13.49	13.12
FeOt	1.19	1.46	1.38	3.71	2.68	2.12
MnO	0.03	0.03	0.03	0.03	0.04	0.03
MgO	0.98	0.53	0.08	0.53	0.68	0.44
CaO	1.61	2.16	0.54	0.9	0.91	0.98
Na2O	2.49	3.99	2.97	2.48	2.22	2.51
K2O	4.92	1.73	4.66	6.61	4.98	5.45
P2O5	0.2	0.18	0.22	0.21	0.18	0.22
H2O+/LOI	0.6	0.86	0.53	0.59	0.49	0.54
Total	98.46	98.18	98.58	98.34	98.65	96.01
(ppm)						
Ba	853	130	97	701	458	430
Cr	<20	<20	<20	<20	51	<20
Cs	<20	<20	<20	<20	<20	<20
Cu	<20	<20	<20	<20	<20	<20
Ga	18	19	20	18	20	21
La	50	29	14	52	38	69
Nb	<20	<20	<20	<20	<20	<20
Nd	41	<20	<20	37	35	35
Ni	<20	<20	<20	<20	<20	<20
Pb	<20	<20	<20	<20	<20	<20
Rb	153	104	311	285	237	238
Sc	<20	<20	<20	<20	<20	<20
Sr	132	72	33	131	82	68
Th	20	22	<20	30	<20	<20
U	<20	<20	<20	<20	<20	<20
V	44	<20	<20	22	33	23
Y	42	31	24	27	40	41
Zn	44	29	<20	31	45	28
Zr	169	90	27	369	120	140

Tab. 8 Whole rock chemistry of selected migmatised and non-migmatised samples from the Gföhl gneiss

GEOTHERMOBAROMETRY

Geothermobarometric analysis is a powerful tool in the service of a petrologist in order to reconstruct the P-T-history based on the fact that mineral assemblages (two or more) modify their composition as a function of pressure and temperature. Accordingly to the final results it should be then possible not only to track down the P-T-path followed by the observed lithology but also to set up a specific tectonic scenario. In the specific case of the Gföhl gneiss the geothermobarometry alone is inadequate because of the strong retrograde overprinting and alteration. This kind of analysis needs hence to be reinforced and constraint by a second analytic method namely thermodynamic modelling with the aid of the so called pseudosections. Those equilibrium phase diagrams display the different stable phase assemblages for a single bulk-rock composition in a P-T grid and will be discussed in detail in the next chapter. In principle, once the peak mineral assemblage has been determined under the optical microscope it will correspond to one stability field on the pseudosection. Now, in ideal cases P/T punctual analyses from the geothermobarometry will plot into that field.

The geobarometers that have been applied to the Gföhl Gneiss are the GASP (*Koziol, 1989*) and the Garnet-Biotite-Plagioclase-Quartz (*Hoisch, 1990*).

Following geothermometers have been used: a monazite-garnet thermometer (*Pyle & Spear et. al.2001*), a monazite-xenotime thermometer (*Gratz & Heinrich, 1997*), a two-feldspar thermometer (*Putirka, 2008*) and titanium in biotite thermometer (*Henry et al., 2005*). The garnet – biotite Fe-Mg exchange thermometer was excluded since diffusional resetting always affected this thermometer in the high grade Gföhl gneiss. The calculation of the geothermobarometers was executed with the support of PET, a Mathematica package for petrologists (*Dachs, 2004*). For the calculation of the pseudosections two petrological software packages have been used: PERPLEX (*Connolly*, *2005*) and Theriak/Domino (*DeCapitani & Petrakakis, 2010*).

GEOBAROMETRY

GASP barometer

The GASP barometer is best suited for metapelites (Franz, 2016) in which garnet has middle to high X_{Grs} values. The Gföhl gneiss is a high grade metamorphosed rock of magmatic origin and has very low X_{Grs}, Therefore obtained results include a larger error due to uncertainties in the activity of grossular component.

For the GASP geobarometry the refined version of *Koziol & Newton* (1988) has been considered and 7 homogeneously distributed samples have been analyzed. Although the flatness of the reaction lines should point at an acceptable geobarometer the pressure range covered by the samples is wide with ΔP = 5 kbar (Fig. 19). From Fig. 19 and Fig. 20 can be observed that the highest concentration of reaction lines plots, at an estimated T of 750 °C, between 9.7-10.9 kbar (ΔP ~1.2kbar). Fig. 20 could partially explain the wide P interval identifying among the samples those which were collected in the north, center and south. It appears to be present at least a trend between northern and southern samples. For further observations see the chapter *Discussion and Conclusions.*

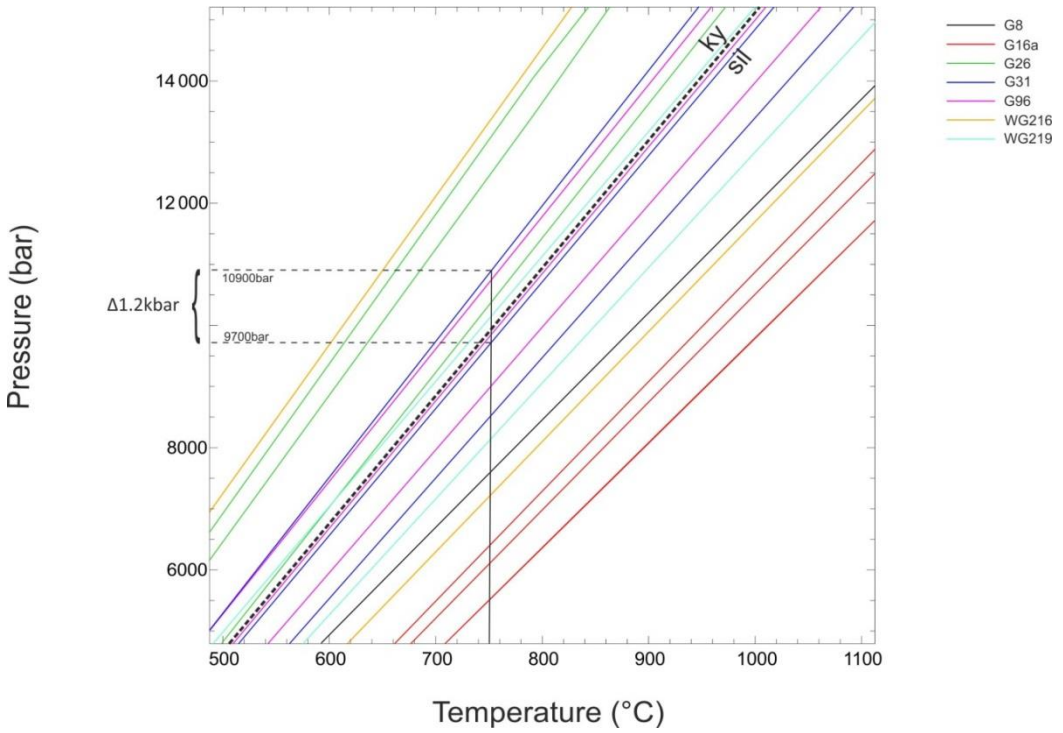

Fig. 19 GASP barometer for P estimation (Koziol, 1989). Different colored lines show the different sample analyzed. The reaction lines represent following reaction: 3CaAl2Si2O8 ↔ Ca3Al2Si3O12+ 2Al2SiO5+SiO2.

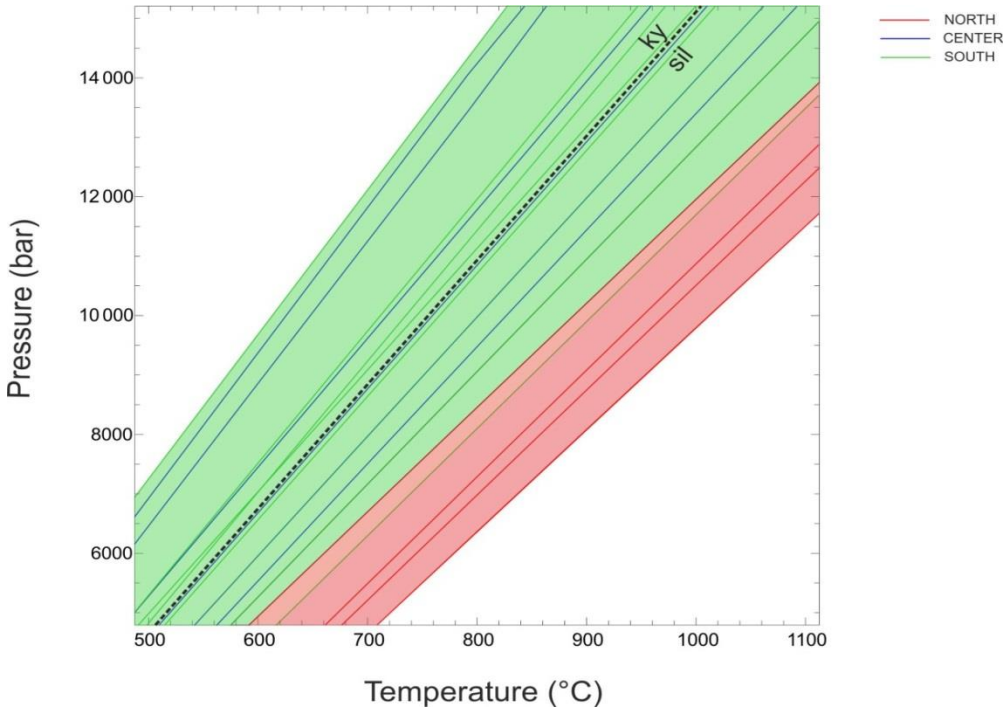

Fig. 20 GASP barometry distinguishing samples taken from the southern- central- and northern part of the studied area. Shadowed domains show the presence of a pressure trend which varies from north to south suggesting an eventual subdivision of the gneissic body.

Garnet-plagioclase-biotite-quartz barometer

Besides using the GASP reaction, a second geobarometer, based on the equilibrium reaction between garnet, plagioclase, biotite and quartz was used to constrain the pressure. As well as for the GASP barometer 7 samples have been considered.

From the six equilibria calibrated as geobarometers in the work of Thomas Hoisch (1990) two were taken into account namely the reaction involving the Mg- and Fe-endmembers of garnet and biotite (Eq. 2 a-b). However, both reactions also include grossular and the same uncertainty as for the GASP reaction, caused by the low activity of grossular, applied here.

(a) $\frac{1}{3}Pyrope + \frac{2}{3}Grossular + Eastonite + 2Quartz \leftrightarrow 2Anorthite + Phlogopite$

(b) $\frac{1}{3}Almandine + \frac{2}{3}Grossular + Siderophyllite + 2Quartz \leftrightarrow 2Anorthite + Annite$

Eq. 2 a-b

Results from Eq. 2b are more reliable since Mg-reactions are less sensitive to diffusion processes. For the Mg-reaction 3 samples out of 7 show higher pressures of 8.3-9.1 kbar (Fig. 21). Although the P range covered by all samples is quite wide there still seems to be a NS-trend with increasing pressure from north to south (Fig. 22).

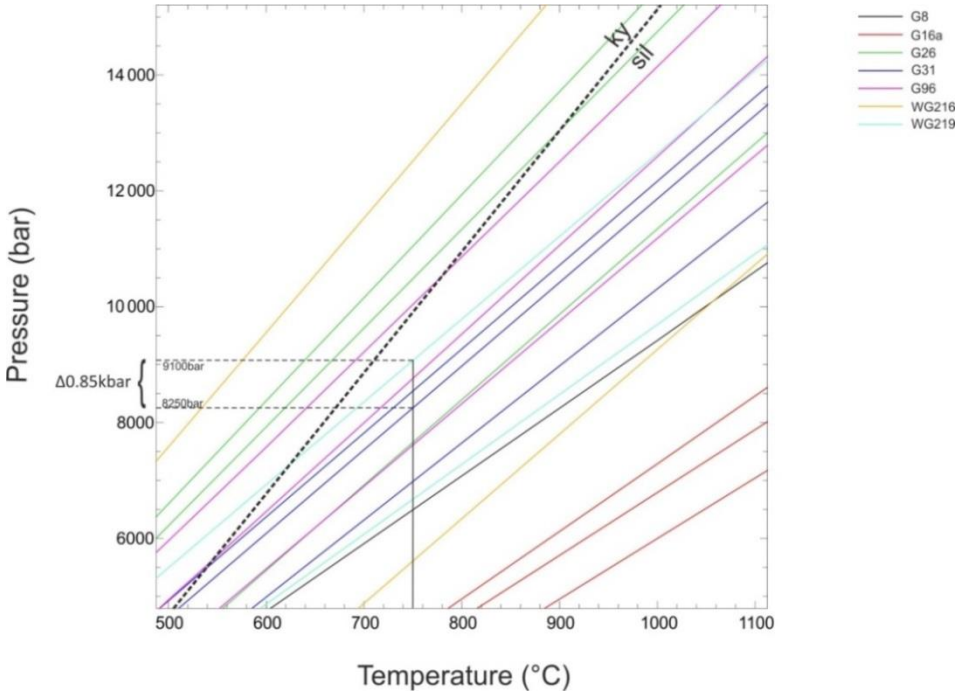

Fig. 21 Application of the Garnet-Plagioclase-Biotite-Quartz barometer for P estimation (*Hoisch, 1990*). Different colored lines show the different sample analyzed. The reaction lines represent following reaction:

$$\frac{1}{3}Mg_3Al_2Si_3O_{12} + \frac{2}{3}Ca_3Al_2Si_3O_{12} + K(Mg_2Al)(Si_2Al_2)O_{10}(OH)_2 + 2SiO_2 \leftrightarrow 2CaAl_2Si_2O_8 + KMg_3(AlSi_3)O_{10}(OH)_2$$

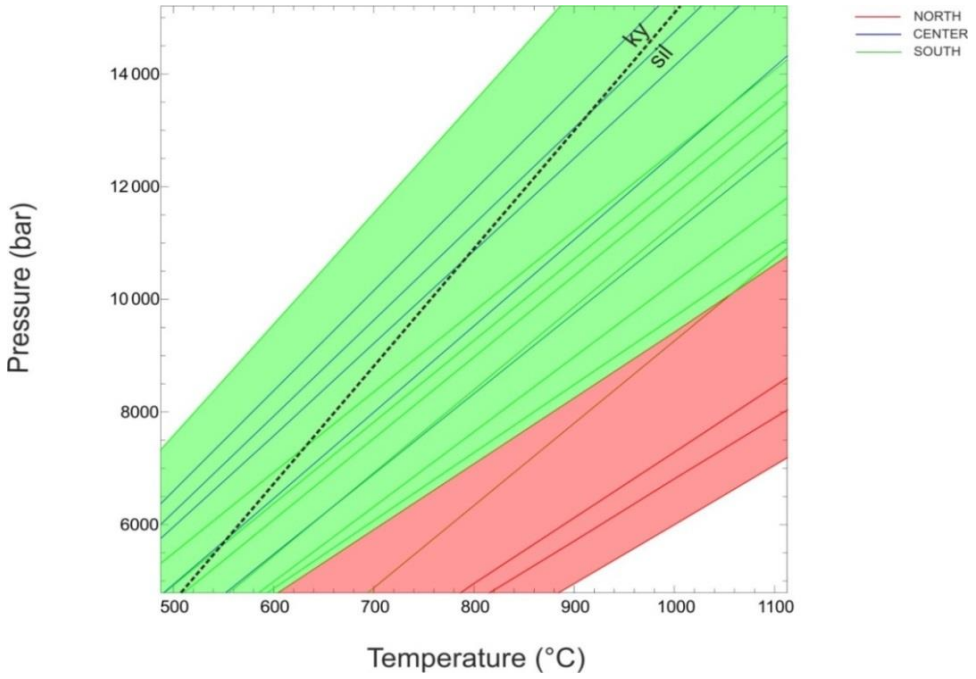

Fig. 22 Garnet-Plagioclase-Biotite-Quartz barometry distinguishing samples taken from the southern- central- and northern part of the studied area. Shadowed domains show the presence of a pressure trend which varies from north to south suggesting an eventual subdivision of the gneissic body.

The equilibrium reaction calibrated as geobarometer in which the Fe-endmembers of garnet and biotite occur shows similar P values as the GASP analysis. The major part of the samples hit an area included between 8.7-10.13 kbar with ΔP= 1.43kbar and a NS-trend is still visible (Fig. 23 and Fig. 24).

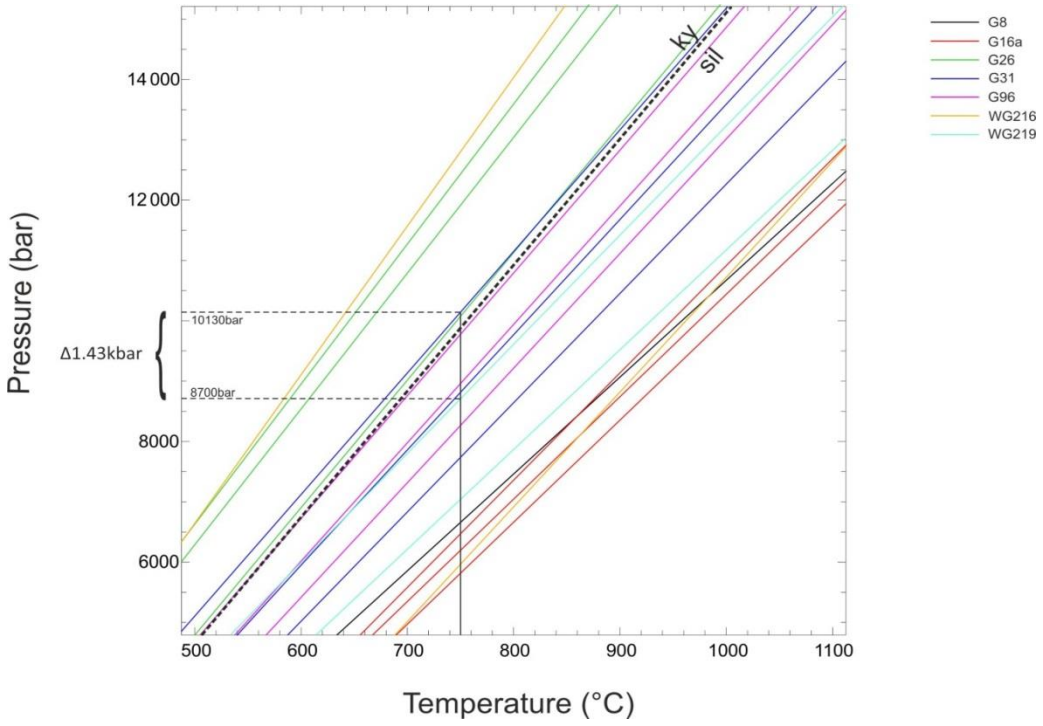

Fig. 23 Application of the Garnet-Plagioclase-Biotite-Quartz barometer for P estimation (*Koziol, 1989*). Different colored lines show the different sample analyzed. The reaction lines represent following reaction:

$$\frac{1}{3}Fe_3Al_2Si_3O_{12} + \frac{2}{3}Ca_3Al_2Si_3O_{12} + K(Fe_2Al)(Si_2Al_2)O_{10}(OH)_2 + 2SiO_2 \leftrightarrow 2CaAl_2Si_2O_8 + KFe_3(AlSi_3)O_{10}(OH)_2$$

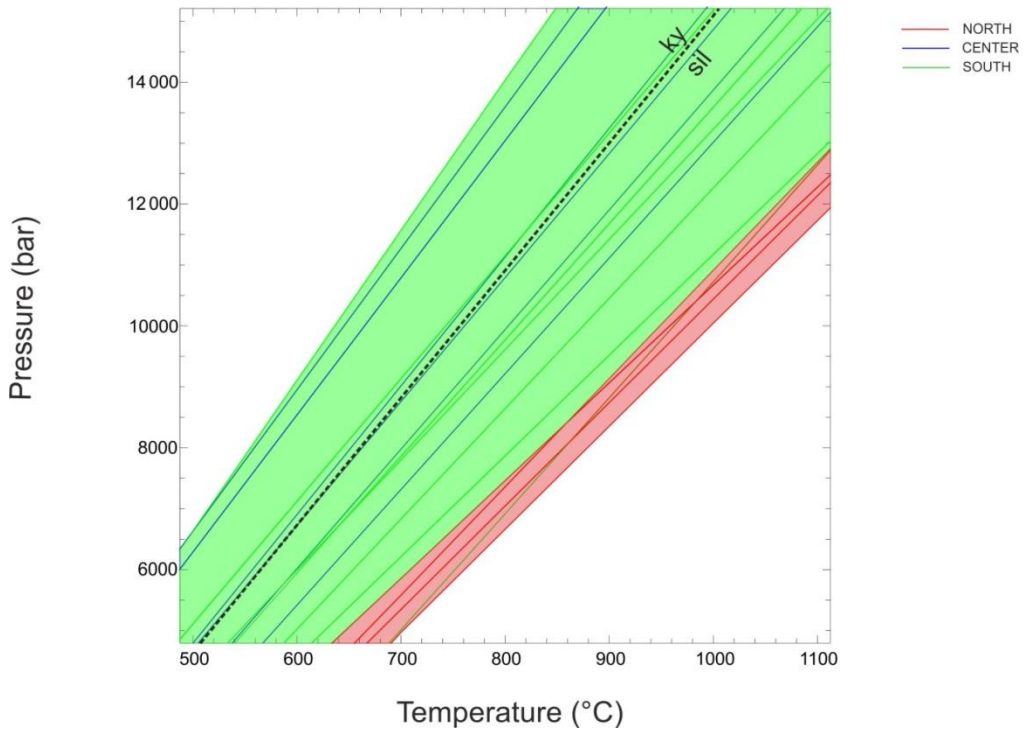

Fig. 24 Garnet-Plagioclase-Biotite-Quartz barometry distinguishing samples taken from the southern- central- and northern part of the studied area. Shadowed domains show the presence of a pressure trend which varies from north to south suggesting an eventual subdivision of the gneissic body**.**

GEOTHERMOMETRY

Monazite-garnet thermometer

As the work of *Pyle and Spear* in 2001 confirmed, monazite and garnet show a systematic relationship as a function of temperature. The thermometer they proposed is based on the partitioning of yttrium between those two phases both recurring in the Gföhl gneiss too.

The mass transfer reaction between monazite and garnet involves other mineral phases as shown below (Eq. 3):

$$Y_3Al_2Al_3O_{12} + Ca_5(PO_4)_3(OH) + \left(\frac{25}{4}\right)SiO_2 = \left(\frac{5}{4}\right)Ca_3Al_2Si_3O_{12} + \left(\frac{5}{4}\right)Ca\,Al_2Si_2O_8 + 3YPO_4 + \left(\frac{1}{2}\right)H_2O$$

(YAG in Grt) (OH-Ap in Ap) Qtz grs in Grt an in Plg $YPO_{4\text{ in Monazite}}$ Fluid

Eq. 3

The parameters listed in Tab. 10 the equilibrium reaction have been used to calculate the equilibrium constant K_{Eq}, which is a function of composition.

YAG in garnet, OH in apatite, grossular in garnet, anorthite in plagioclase and yttrium in monazite were measured with the electron microprob. The water fugacity was calculated with Perplex at P and T using the modified compensated Redlich-Kwong equation of Holland & Powell, 1991, 1998. Quartz is assumed to be pure. Pressure was fixed at 8 kbar.

$$T(°C) = \left[\frac{-1.45P(bar) + 447772(\pm 32052)}{567(\pm 40) - Rln(K_{Eq})}\right] - 273.15$$

Eq. 4

The table shows the calculated parameters and the temperatures carried out by the relationship for the equilibrium between temperature and K_{Eq} expressed above (Eq. 3, Eq. 4, Tab. 9). Three samples were taken into account.

The temperatures don´t fit in any way the values suggested by the literature (750°-900°C). The data could be erroneous due to the fact that this thermometer is calibrated on metapelites having different bulk chemistry from the Gföhl gneiss (especially water content). The scarcity of the data collected for the apatites due to its irregular occurrence could play an important role since even a small variation of X OH in apatite coincides with a strong variation in the resulting equilibrium constant K_{Eq}.

Sample	G8	G16a	G26
X grs, Grt	0.029	0.022	0.080
X an, Plg	0.280	0.205	0.079
X Y, Mnz	0.141	0.072	0.109
FH2o	5664.700	5664.700	5664.700
X Y, Grt	0.056	0.026	0.054
X OH, Ap	0.543	0.543	0.543
X grs, grt ^(15/4)	0.0000017	0.00000068	0.0000770
X an,plg^(5/4)	0.2037000	0.1379000	0.0418800
X Y, mnz^3	0.002800	0.000373	0.0012900
f H2O^1/2 [bar]	237.993	237.993	237.993
X Y, grt^3	0.000175	0.000017	0.0001570
X OH, ap	0.543	0.543	0.543
Keq	0.002448421	0.0009031	0.011613197
P[bar]	8000		
R[J/molK]	8.314		
T[°C]	**434**	**424**	**449**

Tab. 9

Monazite-xenotime thermometer

This geothermo(-baro)meter offers the opportunity to measure the temperature of an igneous or metamorphic rock on the basis of the existing miscibility gap between monazite and xenotime that is due to that different crystal structure of the two phosphates (*Gratz & Heinrich, 1997*)(Fig. 25). Both coexisting phases can incorporate yttrium, to a different extent, in their octahedral position as a function of temperature and pressure.

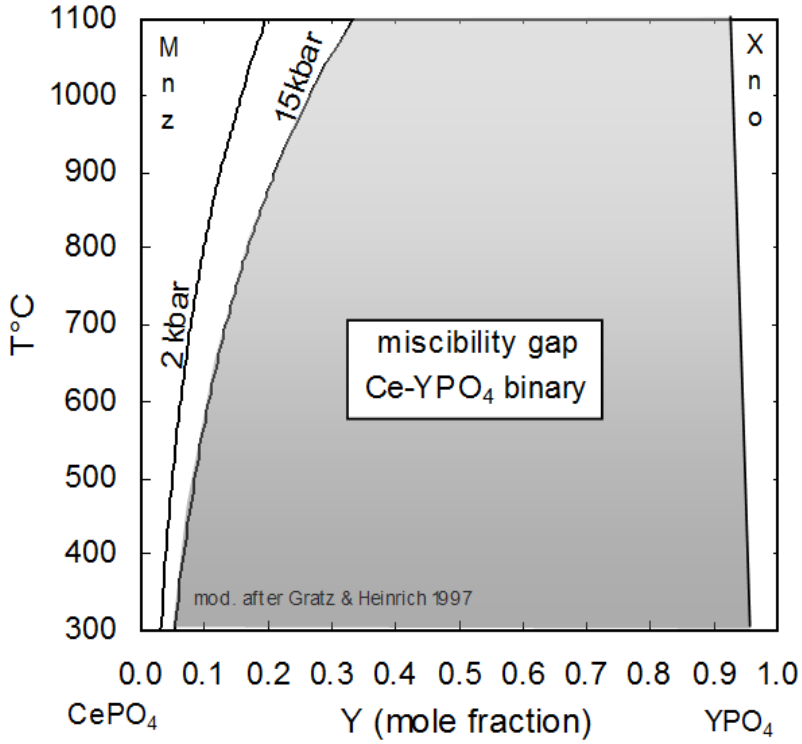

Fig. 25 Diagram showing the miscibility gap in the binary system $Ce(PO)_4$ -$Y(PO)_4$ (Finger, 2015).

Temperature conditions were calculated starting from Eq. 5 where P is given in kbar and T in °C:

$$X_Y^{monazite} = \frac{(1.459 + 0.0852P)e^{0.002274T}}{100}$$

Eq. 5

The geothermometer was applied to 3 samples that in the bulk chemistry indicate the highest values for Ce and Y. An excel sheet was created (Tab. 10) in which $X_{yttrium}$ in monazite was first calculated and then applied to the equation (Eq. 5) at fixed pressures of 7, 7.5, 8, 8.5, 9 kbar.

The temperatures carried out by the monazite-xenotime thermometer are consistent with the peak assemblage of the rock. A variation in the temperature along an N-S axis seems not to be present whereas the strong zonation of most investigated monazites leads to a variation of the temperature within the single crystals (Fig. 26). Measures made at the rim yielded temperatures (sample G8_2p3, Tab. 10) about 550 °C at 8 kbar and temperatures from the core are set at about 800 °C. The results also get along with the experimental analysis of *Gratz & Heinrich* in which was observed that the Y content in monazite increases with increasing metamorphic grade (i.e. in the core).

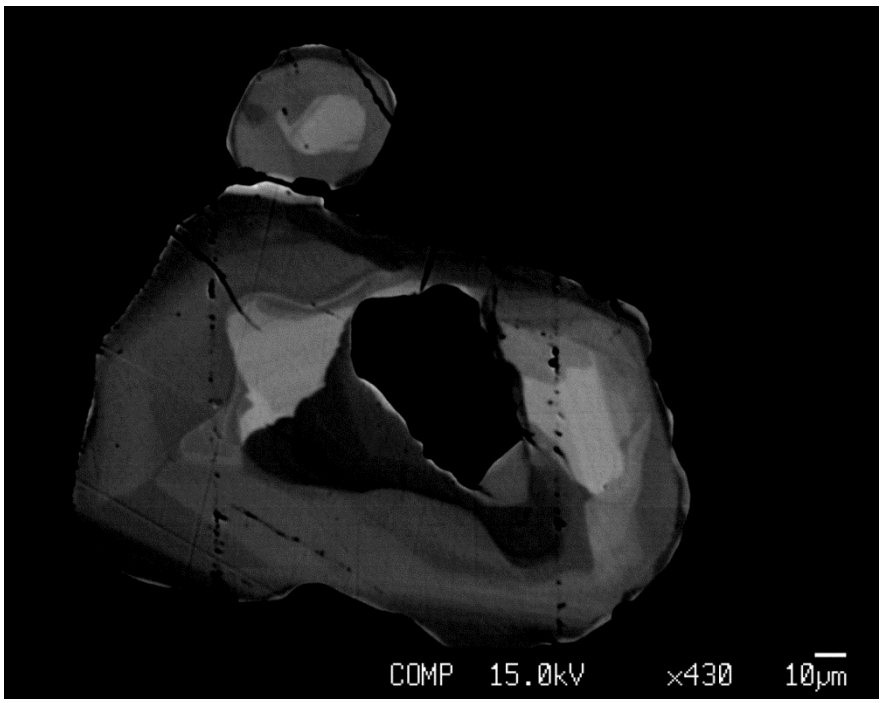

Fig. 26 Strong zoned Monazite. Yttrium content in monazite tends to be higher at the core resembling peak metamorphism conditions and lower at the rim. Sample WG216.

Sample	G8_2 p1	G8_2 p2	G8_2 p3	G16a_e p1.2	G26_1 p1	G26_2 p1
	CORE	CORE	RIM	CORE	CORE	CORE
SiO2	0.20	0.20	0.23	0.46	0.30	0.20
P2O5	30.02	29.94	30.11	29.58	30.28	30.34
Ce2O3	28.99	29.18	29.60	29.92	29.64	32.49
PbO	0.12	0.12	0.10	0.12	0.22	0.19
Al2O3	b.d.l.	b.d.l.	b.d.l.	b.d.l.	b.d.l.	b.d.l.
Y2O3	2.97	3.31	1.66	1.63	2.51	2.34
La2O3	13.19	12.66	12.88	13.67	10.40	12.18
UO2	0.53	0.52	0.53	1.23	1.59	2.67
CaO	1.27	1.28	1.14	0.94	2.02	1.52
Nd2O3	10.55	10.40	11.47	10.54	9.59	8.76
ThO2	5.79	5.93	5.29	3.88	8.60	4.88
Sm2O3	1.73	1.59	2.10	2.05	2.03	1.68
Pr2O3	3.36	3.33	3.73	3.54	3.58	3.43
Total	98.72	98.44	98.83	97.55	100.75	100.66
Si	0.008	0.008	0.009	0.018	0.012	0.008
P	0.995	0.994	0.999	0.994	0.989	0.992
Ce3	0.416	0.419	0.425	0.435	0.419	0.459
Pb	0.001	0.001	0.001	0.001	0.002	0.002
Al	0.000	0.000	0.000	0.000	0.000	0.000
Y	0.062	0.069	0.035	0.034	0.051	0.048
La	0.190	0.183	0.186	0.200	0.148	0.173
U	0.005	0.004	0.005	0.011	0.014	0.023
Ca	0.053	0.054	0.048	0.040	0.084	0.063
Nd	0.147	0.146	0.161	0.149	0.132	0.121
Th	0.052	0.053	0.047	0.035	0.075	0.043
Sm	0.023	0.021	0.028	0.028	0.027	0.022
Pr	0.048	0.048	0.053	0.051	0.050	0.048
Xy (Y/Y+Ce)	0.130	0.141	0.076	0.072	0.109	0.095
T[°C] at 9 kbar	775	813	541	520	697	637
T[°C] at 8.5 kbar	784	822	549	528	705	645
T[°C] at 8 kbar	793	831	558	537	714	654
T[°C] at 7.5 kbar	801	839	567	546	723	663
T[°C] at 7 kbar	810	848	576	555	732	672

Tab. 10

Two-feldspar thermometer

A two feldspar thermometer (*Fuhrman & Lindsley, 1988, Putirka, 2008, Benisek, 2010*) was used in attempt to constrain furthermore the temperature experienced by the Gföhl gneiss. The thermometer is based on the miscibility gap between K-feldspar and albite.

Because of the granulitic facies conditions enhancing diffusion and flexibility of the lattice structure the feldspar structure can accommodate both K and Na building up a solid solution known as ternary feldspar; under cooling conditions the ternary feldspar intercepts the solvus curve and K-feldspar and albitic plagioclase are formed.

This method yields a minimum temperature since it gives the possibility to recover the conditions in which the ternary feldspar started to give up Na to form albitic plagioclase by cooling (solvus intersection) but not the conditions in which it was actually formed.

In order to apply this thermometer the composition of feldspars, of their perthitic exsolutions and of surrounding plagioclases have been measured at the electron microprobe.

The first part of the reintegration of the ternary feldspar consisted in reintegrating the albitic perthites with their host mineral. This step was made following an excel spreadsheet made available after Artur Benisek. The second and final reintegration of the feldspar with a surrounding plagioclase was made basing on the work of *Putirka*, 2008.

Two equations were used both derived by the experimental data of *Elkins* and *Grove*, 1990. The first equation (Eq. 6) was calibrated from 30 of 41 experiments and recovers T to ± 23 °C. The second equation (Eq. 7) represents instead a global calibration from all 41 experimental observations recovering T to ±30 °C (*Putirka, 2008*).

$$\frac{10^4}{T(^\circ C)} = 9.8 - 0.098P(kbar) - 2.46\ln\left(\frac{X_{Ab}^{kfs}}{X_{Ab}^{plg}}\right) - 14.2\left(X_{Si}^{kfs}\right) + 423\left(X_{Ca}^{kfs}\right) - 2.42\ln\left(X_{An}^{kfs}\right) - 11.4(X_{An}^{plg}X_{Ab}^{plg})$$

Eq. 6

$$T(°C) = \frac{-442 - 3.72P(kbar)}{-0.11 + 0.1\ln\left(\frac{X_{Ab}^{kfs}}{X_{Ab}^{plg}}\right) - 3.27\left(X_{An}^{kfs}\right) + 0.098\ln\left(X_{An}^{kfs}\right) + 0.52(X_{An}^{plg}X_{Ab}^{plg})}$$

Eq. 7

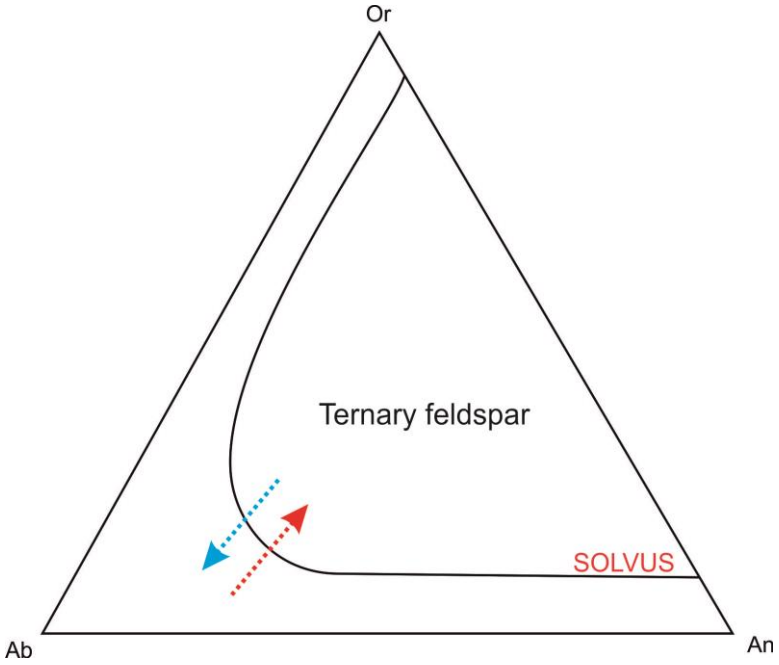

Fig. 27 Diagram showing the solvus curve that delimits the stability field of the ternary feldspar. The blue arrow represents a cooling path (retrograde) whereas the red arrow a heating one (prograde path) (modified after Seck, 1972).

At a fixed pressure of 8 kbar, the temperature carried out by the thermometer fit in an acceptable way the previous collected data. No trend has been recognized within the N-S displaced gneissic body. The apparently most reliable equation infers a temperature comprised between 770 and 840 °C.

Although the samples listed in Tab. 11 indicate good data most samples are too low in temperature to indicate the granulitic conditions that are pointed out by the displayed peak assemblage of the Gföhl gneiss, by the textural observations, by the calculated geothermometry as well as by the indications in the literature.

A possible source of error for this method could be the erroneous reintegration of the albitic exsolutions within the k-feldspar. The thinness of the perthites could have led to inaccurate measurements at the electron microprobe. It should also be considered that the error could also not be analytical: the low temperatures measured could derive from the slow cooling of the rock. The slower the cooling, the lower the temperature in which the diffusion between the perthitic exsolution and the K-feldspar has frozen. Errors can also generate by the recrystallization of feldspars during the cooling path resetting the original composition and carrying out lower temperatures.

	G98_1		G98_2		WG219_1	
	REINTEGRATED FELDSPAR	PLAGIOCLASE	REINTEGRATED FELDSPAR	PLAGIOCLASE	REINTEGRATED FELDSPAR	PLAGIOCLASE
SiO2	65,16	64.93	64,97	64.55	65,92	64.32
Al2O3	19,18	22.12	19,65	22.00	19,13	22.90
CaO	0,91	3.15	0,89	3.14	0,15	3.66
K2O	11,00	0.32	10,45	0.25	10,59	0.26
Na2O	3,75	9.32	4,03	9.54	4,21	9.12
XNa	0,240	0.827	0,262	0.834	0,282	0.806
XCa	0,058	0.154	0,058	0.152	0,010	0.178
XK	0,703	0.019	0,680	0.014	0,708	0.016
T[°C] after Eq. 27a	815		831		836	
T[°C] after Eq. 27b	759		768		721	
P[kbar]	8					

	WG219_2		G8_1	
	REINTEGRATED FELDSPAR	PLAGIOCLASE	REINTEGRATED FELDSPAR	PLAGIOCLASE
SiO2	66,08	64.26	64.79	61.64
Al2O3	18,99	23.06	18.89	25.23
CaO	0,10	3.94	0.38	5.64
K2O	10,73	0.20	14.86	0.19
Na2O	4,11	9.17	1.33	7.75
XNa	0,275	0.799	0.120	0.705
XCa	0,006	0.190	0.002	0.284
XK	0,718	0.011	0.879	0.011
T[°C] after Eq. 27a	793		776	
T[°C] after Eq. 27b	689		699	
P[kbar]	8			

Tab. 11

Ti in biotite thermometer

Biotites from the Gföhl gneiss show a proper chemical composition that allow the application of the Ti in biotite thermometer (*Henry et al., 2005*) that can be only employed under restraining conditions:

The rock should present following phases in its assemblage:

- Ilmenite or rutile
- Graphite
- Quartz
- Aluminous minerals (i.e. $Al_2SiO_2O_5$ polymorphs, etc.)

Biotite should also have a composition between XMg=0.275-1.0 and Ti=0.04-0.6 apfu.

The temperatures calculated correspond to a minimum temperature due to the absence of graphite in the Gföhl gneiss which causes an underestimation of the actual temperatures of ~50°C (*Henry et al., 2005*).

The pressure range in which the Ti in Biotite thermometer has been calibrated is set between 4-6 kbar whereas the Gföhl gneiss experienced pressures between 8-10 kbar; this matter of fact leads to a lower Ti content in the studied rocks and consequently to lower Ti in biotite temperatures (*Henry et al., 2005*).The temperatures have been determined with the following expression (Eq. 8):

$$T(^{\circ}C) = \left([\ln(Ti) - (-2.3594) - (-1.7283)\left(X_{Mg}\right)^{3}]/4.6482^{-9}\right)^{0.333}$$

a ***c*** ***b***

Eq. 8

Where *a, b, c* are experimental coefficients, *Ti* is the atom per formula unit normalized to 22 oxygens and X_{Mg} is Mg/(Mg+Fe).

An average temperature was set at 716 ± 44 °C. Keeping in mind that the Ti-in-Biotite geothermometer is best fitted for peraluminous metapelites that have equilibrated at 4-6 kbar, the temperatures obtained seem to fit sufficiently the previous calculated data constraining once more the (minimum) temperature range experienced by the Gföhl gneiss (Tab. 12).

	GG57_Bt	G8_Bt	G16a_Bt
	NORMALIZED TO 22 OXYGENES	NORMALIZED TO 22 OXYGENES	NORMALIZED TO 22 OXYGENES
	Ti 0.627	Ti 0.546	Ti 0.334
	XMg 0.640	XMg 0.472	XMg 0.395
T°[°C]	796	747	665

	G31_Bt	G28_Bt	G96_Bt
	NORMALIZED TO 22 OXYGENES	NORMALIZED TO 22 OXYGENES	NORMALIZED TO 22 OXYGENES
	Ti 0.368	Ti 0.476	Ti 0.420
	XMg 0.398	XMg 0.371	XMg 0.297
T°[°C]	681	716	692

	WG219_Bt
	NORMALIZED TO 22 OXYGENES
	Ti 0.460
	XMg 0.383
T°[°C]	712

Tab. 12

THERMODYNAMIC MODELLING

Thermodynamic modelling is based on multiphase equilibrium calculations and on Gibbs free energy minimization.

Unlike the conventional geothermobarometry that utilizes for each geothermobarometer its own thermodynamic dataset, the multiphase equilibrium calculations put together all the reactions between phases considered in a given bulk chemistry.

The conventional geothermobarometry gives in the case of the Gföhl gneiss a more generalized overview on the P-T conditions experienced by the rock due to high variance mineral assemblages and the fact that Fe-Mg exchange equilibria are unsuitable for granulite facies rocks and two feldspar thermometry could not be used in many cases.

Equilibrium phase diagrams are therefore used in the attempt to constrain PT-conditions of the peak assemblage and the PT-path followed by the rock.

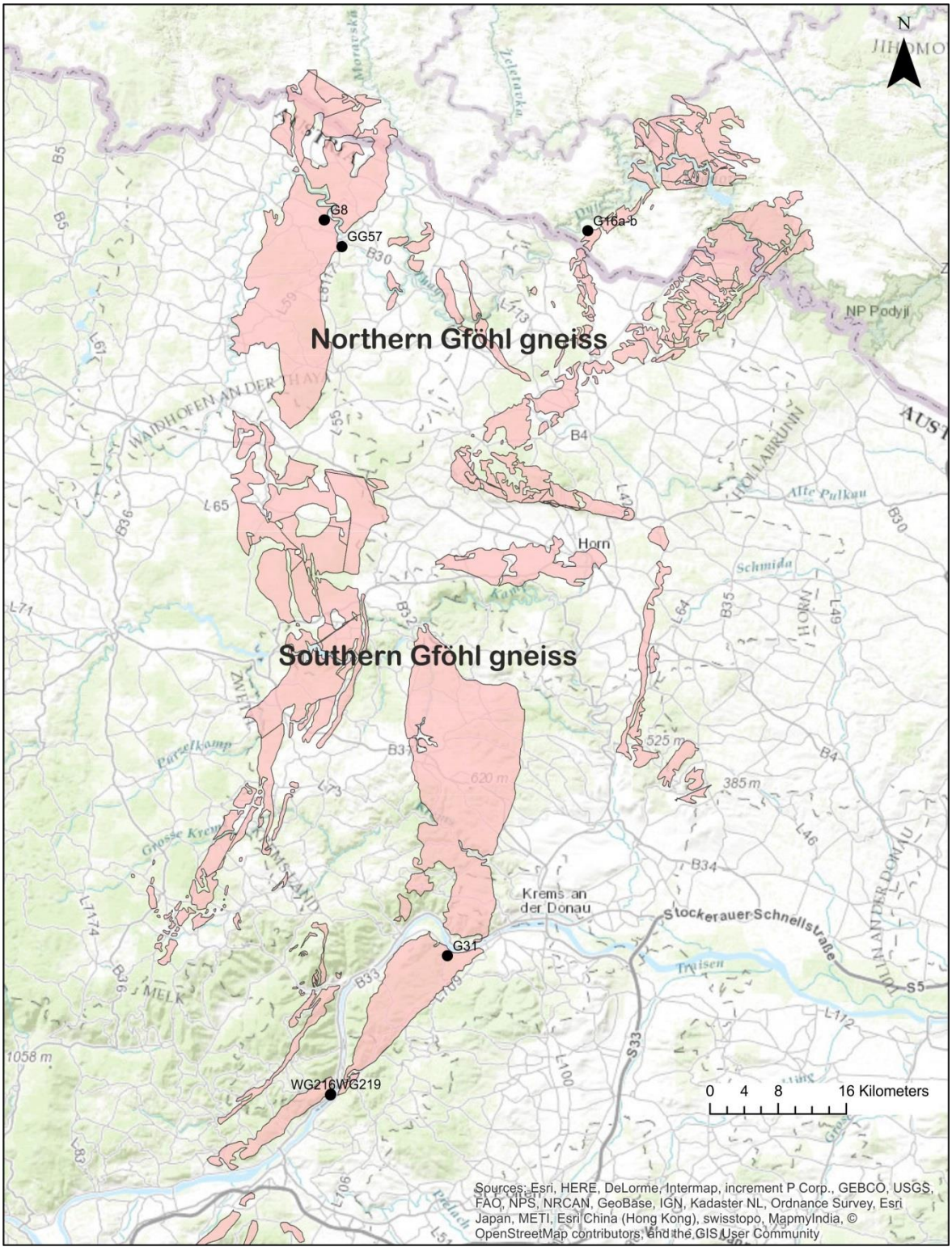

Fig. 28 Geographic sketch of the Waldviertel area with overlying geologic map of the Gföhl Gneiss. The geothermobarometry and the thermodynamic modelling point out at differentiation between a northern and a southern part within the studied lithology.

Pseudosections

The equilibrium phase diagrams (a.k.a. Pseudosections) showing the fields of stability of different equilibrium mineral assemblages for a single bulk-rock composition (*serc.carleton.edu*) were calculated alternatively by two software packages: Perplex_X (*Connolly, 2005*) and Theriak Domino (*Capitani & Petrakakis, 2010*). Both softwares are based on Gibbs free energy minimization.

The analysis done with Perplex were performed with the thermodynamic data file hp11ver.dat of Holland & Powell, 2011; the solution models for garnet, feldspar, biotite, melt, mica, cordierite, orthopyroxene and chlorite were used after WHITE et al., 2014. The solution model used for spinel is after WHITE, POWELL & CLARKE, 2002.

The pseudosections calculated with Theriak Domino have been analyzed with following solutions models: garnet, HOLLAND & POWELL, 1998; feldspar, BENISEK et al., 2010; biotite, WHITE, POWELL & HOLLAND, 2007; melt, WHITE et al., 2007; mica, COGGON & HOLLAND, 2002; cordierite, HOLLAND & POWELL, 1998; orthopyroxene, HOLLAND & POWELL, 1999; chlorite, GAIDIES et al., 2008; spinel, WHITE et al., 2007; All the calculations were performed in the ten component chemical system NCKFMASHTiMn. In all samples 15% of Fe is assumed to be ferric (Fe_2O_3). The RFA data are given in weight percent (wt %) normalized to 100. For thermodynamic modelling with Theriak Domino these values are converted in mole.

Water content estimation

The lack of hydrous phases in the peak assemblage of the rock (only biotite) allows only a rough estimation of the water content.

To constrain a plausible water content for the Gföhl gneiss diagrams where temperature plots against water content (with H_2O wt% = 0 to 5 at a fixed pressure of 8 and 9 kbar) were created (Fig. 29). Sample WG221 was chosen since it approximates well the average chemical composition of the Gföhl gneiss. The whole rock analysis yields a composition of SiO_2= 72.16 wt%, TiO_2= 0.35 wt%, Al_2O_3= 13.49 wt%, FeO= 2.23 wt%, MnO= 0.04 wt%, MgO= 0.68 wt%, CaO= 0.91 wt%, Na_2O= 2.22 wt%, K_2O= 4.98 wt%, P_2O_5= 0.18 wt% and LOI= 0.49 wt%. The stability field of the peak assemblage is wide and ranges from 0 wt% to more than

5 wt% in water content at different pressures. Therefore there is no way to set an absolute value but at least there is more freedom to take an arbitrary one. Basedd on the calculated T-X diagrams the water content set for all calculations of the pseudosections is 1 wt%.

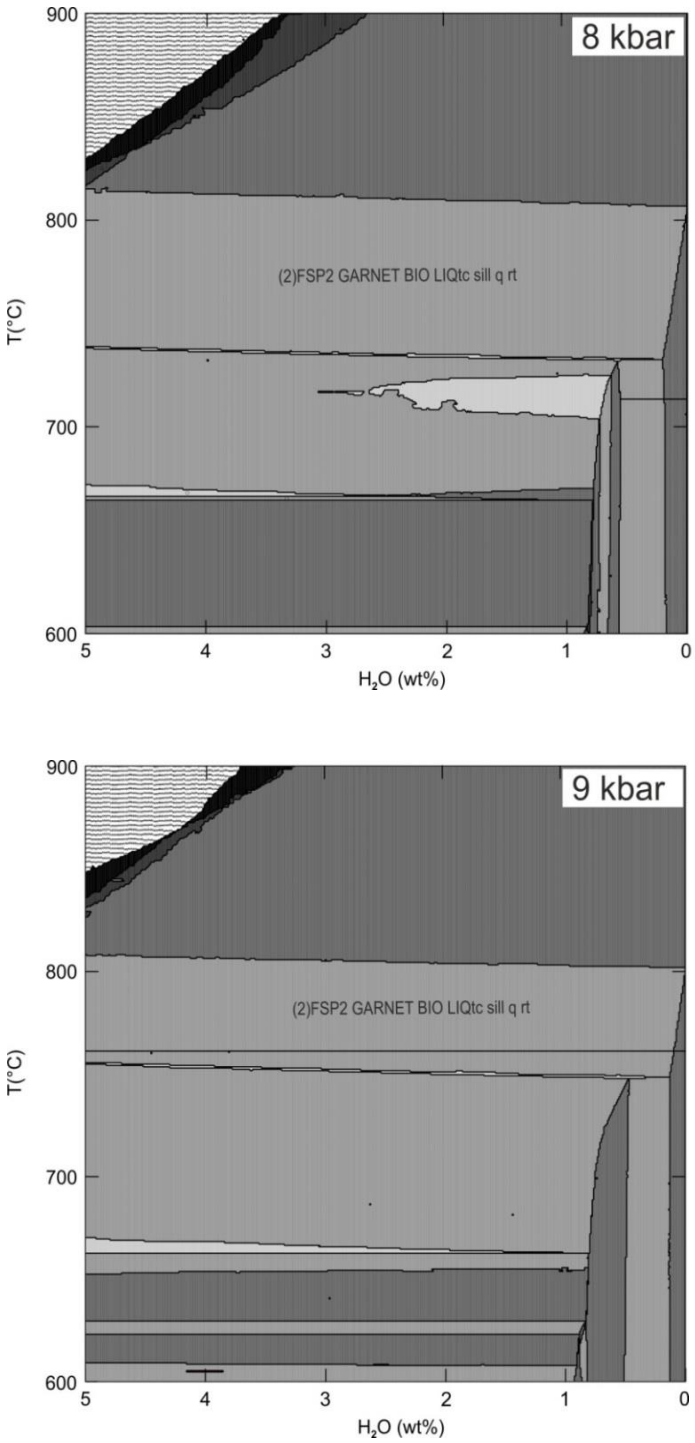

Fig. 29 T-X diagrams in which temperature plots against water content at fixed pressures 8 and 9 kbar.

PT- pseudosections

6 Samples were chosen for thermodynamic modelling of the peak metamorphic event of the Gföhl gneiss.

Samples G8, G16a and GG57 (Fig. 30, Fig. 31, Fig. 32) were collected in the north, samples G31, WG216, WG219 (Fig. 33Fig. 34Fig. 35) in the southern part of the study-area.

North

The whole rock analysis of sample G8 yields a chemical composition of SiO_2= 68.92 wt%, TiO_2= 0.48 wt%, Al_2O_3= 14,74 wt%, FeO= 2.48 wt%, MnO= 0.03 wt%, MgO= 0.98 wt%, CaO= 1.61 wt%, Na_2O= 2.49 wt%, K_2O= 4.92 wt%, P_2O_5= 0.20 wt% and LOI= 0.60 wt.

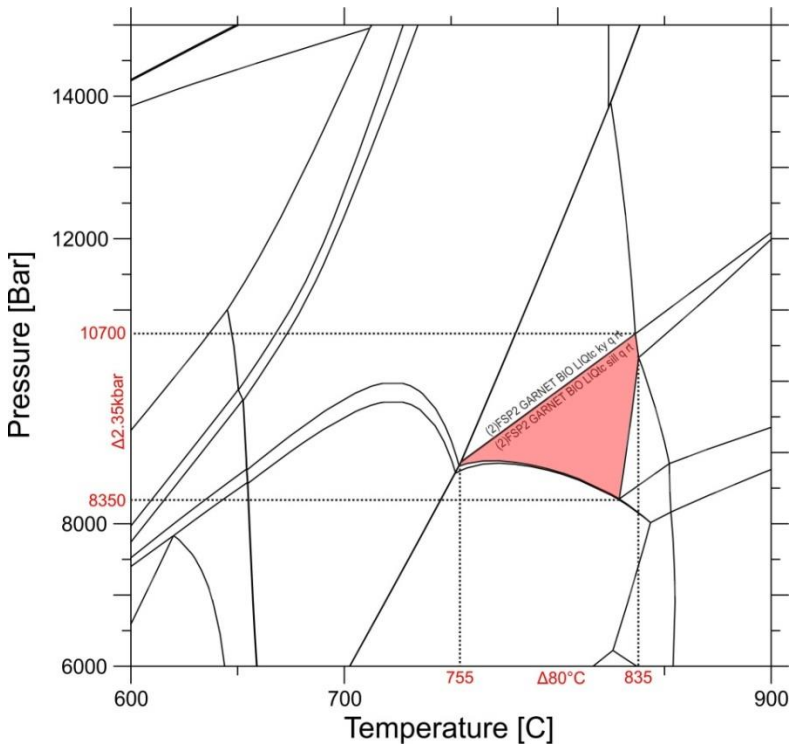

Fig. 30 Pseudosections showing the stability field of the observed peak assemblage from sample G8 calculated in the NCKFMASHTiMn-system. Element composition of the sample in mole cations: SI(1.1471)TI(0.0060)AL(0.2891)CA(0.0288)MG(0.0242)FE(0.0345)K(0.1045)NA(0.0804)MN(0.0005)H(0.1110)

The whole rock analysis of sample G16a yields a chemical composition of SiO_2= 65.68 wt%, TiO_2= 0.71 wt%, Al_2O_3= 15.34 wt%, FeO= 4.48 wt%, MnO= 0.24 wt%, MgO= 1.77 wt%, CaO= 0.70 wt%, Na_2O= 1.36 wt%, K_2O= 4.50 wt%, P_2O_5= 0.09 wt% and LOI= 2.05 wt%.

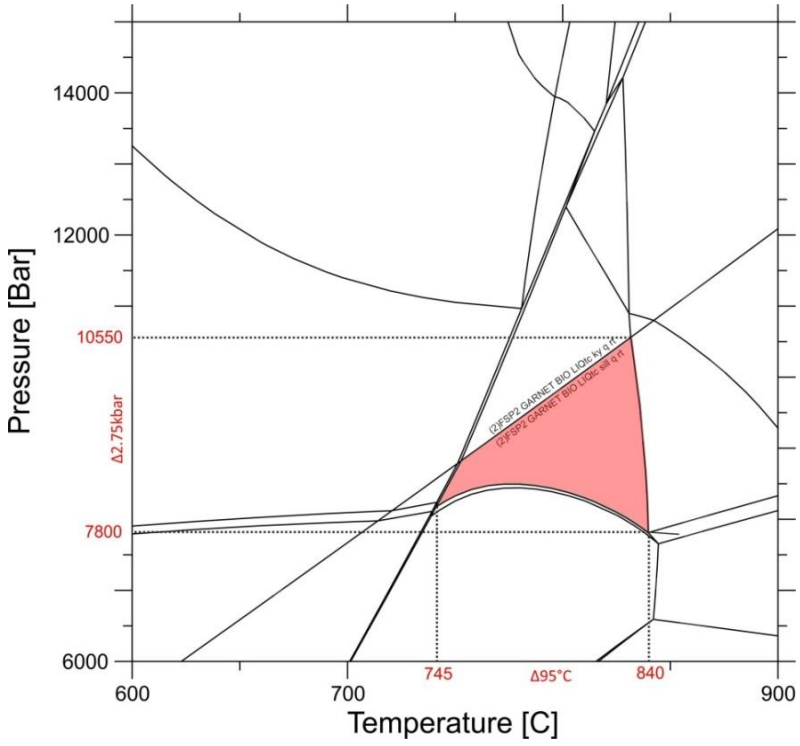

Fig. 31 Pseudosections showing the stability field of the observed peak assemblage from sample G16a calculated in the NCKFMASHTiMn-system. Element composition of the sample in mole cations:
SI(1.0932)TI(0.0089)AL(0.3009)CA(0.0124)MG(0.0440)FE(0.0624)K(0.0954)NA(0.0437)MN(0.0034)H(0.1110)

The whole rock analysis of sample GG57 yields a chemical composition of SiO_2= 68.17 wt%, TiO_2= 0.67 wt%, Al_2O_3= 14.24 wt%, FeO= 5.96 wt%, MnO= 0.08 wt%, MgO= 1.92 wt%, CaO= 2.30 wt%, Na_2O= 2.24 wt%, K_2O= 2.76 wt%, P_2O_5= 0.08 wt% and LOI= 0.68 wt%.

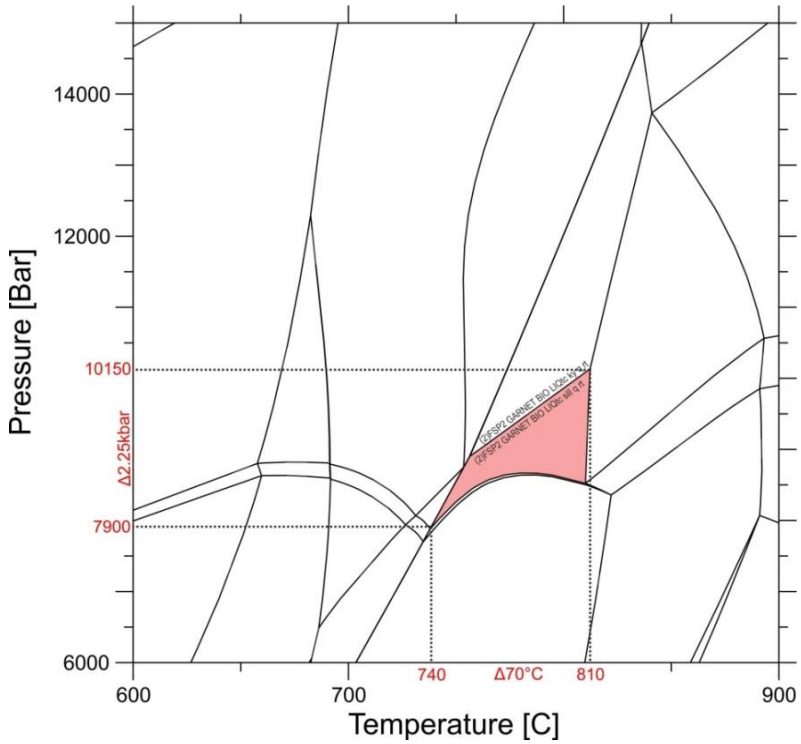

Fig. 32 Pseudosections showing the stability field of the observed peak assemblage from sample GG57 calculated in the NCKFMASHTiMn-system. Element composition of the sample in mole cations:
SI(1.1346)TI(0.0084)AL(0.2794)CA(0.0410)MG(0.0476)FE(0.0572)K(0.0587)NA(0.0721)MN(0.0012)H(0.1110)

South

Since the stability field of the peak paragenesis in the south covers a wider P-range the pseudosections will only indicate the T-range. The visual determination of the resumed pressure along the southern Gföhl gneiss will be made explicit at the end of this chapter by showing the overlap area of all the stability fields of the paragenesis in a P-T diagram (Fig. 36).

The whole rock analysis of sample G31 yields a chemical composition of SiO_2= 72.43 wt%, TiO_2= 0.29 wt%, Al_2O_3= 13.40 wt%, FeO= 2.40 wt%, MnO= 0.02 wt%, MgO= 0.54 wt%, CaO= 1.00 wt%, Na_2O= 2.74 wt%, K_2O= 4.77 wt%, P_2O_5= 0.19 wt% and LOI= 0.60 wt%.

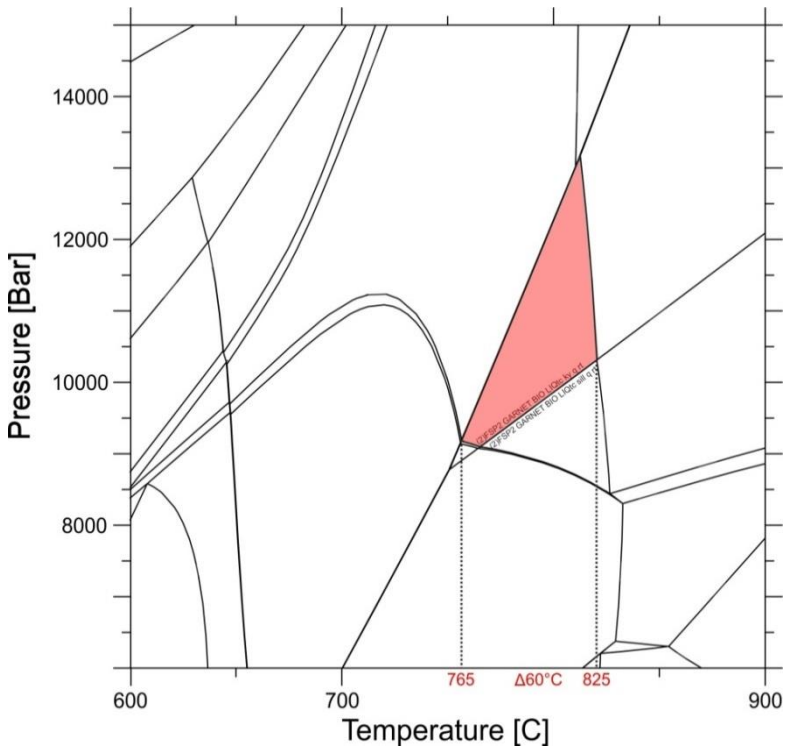

Fig. 33 Pseudosections showing the stability field of the observed peak assemblage from sample G31a calculated in the NCKFMASHTiMn-system. Element composition of the sample in mole cations: SI(1.2054)TI(0.0036)AL(0.2629)CA(0.0178)MG(0.0134)FE(0.0230)K(0.1012)NA(0.0884)MN(0.0003)H(0.1110)

The whole rock analysis of sample WG216 yields a chemical composition of SiO_2= 69.76 wt%, TiO_2= 0.32 wt%, Al_2O_3= 14.49 wt%, FeO= 2.37 wt%, MnO= 0.03 wt%, MgO= 0.53 wt%, CaO= 2.30 wt%, Na_2O= 2.48 wt%, K_2O= 6.61 wt%, P_2O_5= 0.21 wt% and LOI= 0.59 wt%.

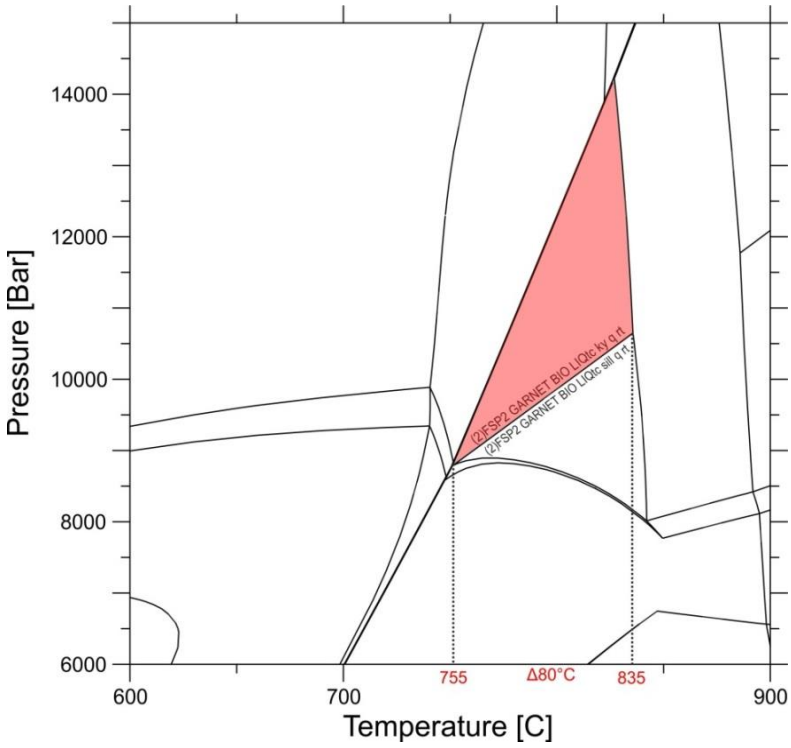

Fig. 34 Pseudosections showing the stability field of the observed peak assemblage from sample WG216 calculated in the NCKFMASHTiMn-system. Element composition of the sample in mole cations:
SI(1.1940)TI(0.0041)AL(0.2923)CA(0.0114)MG(0.0134)FE(0.0227)K(0.1444)NA(0.0823)MN(0.0004)H(0.0110)

The whole rock analysis of sampleWG219 yields a chemical composition of SiO_2= 68.78 wt%, TiO_2= 0.16 wt%, Al_2O_3= 16.10 wt%, FeO= 1.23 wt%, MnO= 0.01 wt%, MgO= 0.27 wt%, CaO= 0.85 wt%, Na_2O= 2.89 wt%, K_2O= 7.46 wt%, P_2O_5= 0.15 wt% and LOI= 0.32 wt%.

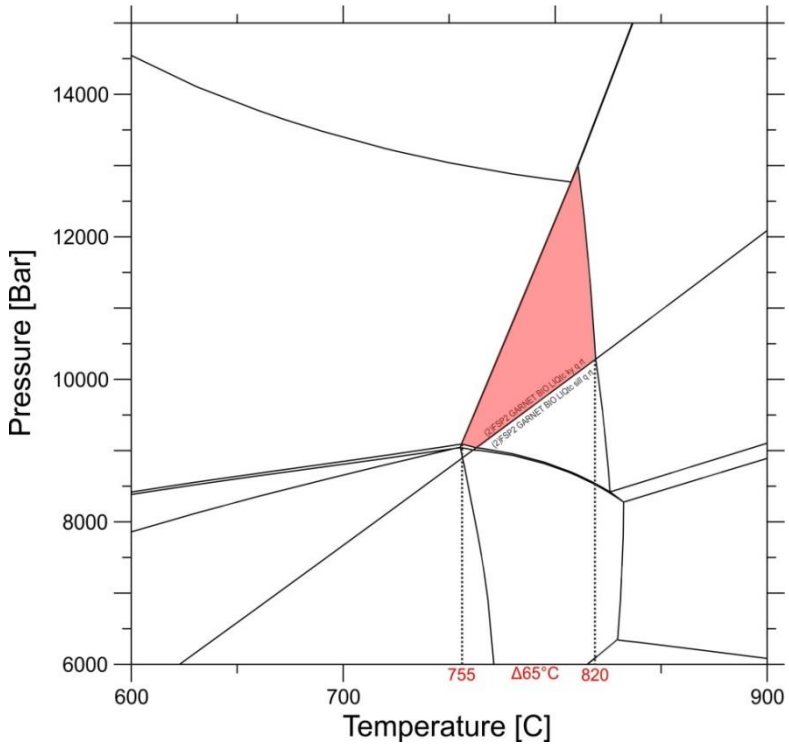

Fig. 35 Pseudosections showing the stability field of the observed peak assemblage from sample WG219 calculated in the NCKFMASHTiMn-system. Element composition of the sample in mole cations: SI(1.1447)TI(0.0020)AL(0.3156)CA(0.0152)MG(0.0067)FE(0.0117)K(0.1584)NA(0.0934)MN(0.0002)H(0.0110)

Two different peak assemblages were observed from north to south pointing out at two different P-T conditions within the same lithology. In the south kyanite makes its first appearance. Apart from that, in order to constrain and clarify even further the P- and T-ranges experienced by the northern and southern rocks, one P-T diagram showing the overlapping stability fields of the two peak assemblages observed have been made (Fig. 36).

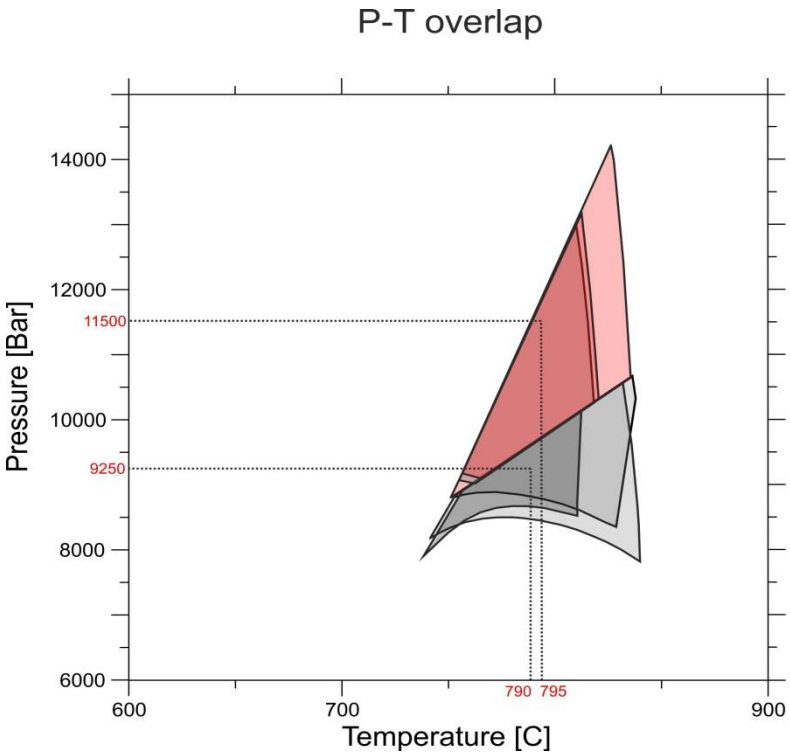

Fig. 36 P-T overlap obtained by plotting together samples from the north G8, G16a and GG57 (gray shades) and from the south WG216, WG219 and G31 (red shades).

The stability fields fit in an acceptable way with one another and express following P-T ranges:

Northern Gföhl gneiss → P= 9.2 ±1.4 kbar T= 790 ±50°C

Southern Gföhl gneiss → P= 11.5 ±2.7 kbar T= 795 ±45°C

The data point out at almost identical temperatures between northern and southern samples whereas the pressure increases slightly from north to south (Fig. 28).

DISCUSSION AND CONCLUSION

Defining the petrology and the petrogenetic conditions of the Gföhl gneiss represents a key aspect that could help decipher the geodynamic setting of the entire moldanubian area.

Defining the peak assemblage

The distribution of the investigated Gföhl gneiss in the field extends from Znojmo (CZ) in the north, to Melk (AUT) in the south (Fig. 28)

In the field and under the transmitted light microscope a change in peak assemblage from south to north was found. Samples from the north contain grt+sil+kfs+pl+bt+qz as peak assemblage where garnet´s frequency of occurrence is lower than in the south as well as the occurrence of Al-silicate. Al-silicate occurs in the north exclusively as fibrolite. The border between northern and southern domain is marked by the occurrence of sub-euhedral sillimanite instead of fibrolite and an increasing abundance of garnet. In the southern area of the Gföhl gneiss sillimanite is less common and if there replaces kyanite, which is the dominant Al_2SiO_5 phase. Large euhedral garnets are also more common.

P-T conditions

Equilibrium phase diagrams have been used to constrain P-T conditions in addition to the applied geothermobarometers. The interpretation of GASP and Garnet-plagioclase-biotite barometers allowed identifying a slight gradient from N to S. (Fig. 20, Fig. 22, Fig. 24).

Three of the four applied geothermometers (*Monazite-Xenotime thermometer after Gratz & Heinrich, 1997,* two feldspars thermometer after *Putirka, 2008* and Ti in biotite after *Henry et al., 2005*) gave consistent temperatures with values from 710-810 °C at P=8 kbar (Tab. 13). The temperatures calculated are minimum temperatures as explained in the chapter *Geothermobarometry* (Tab. 13).

Results from thermodynamic modelling show consistent P-T conditions and strengthen the presence of a slight pressure gradient from north to south. (Fig. 36) with ~9 kbar and 790 ±50°C in the north and ~11.5 kbar and 795 ±45.

GEOBAROMETER	yielded P [kbar]	
	North	South
Garnet-plagioclase-Al2SiO5-quart (GASP) after *Koziol, 1989*	8.4	9.1
Garnet-plagioclase-biotite-quartz after *Hoisch, 1990*	8.3	9.8
GEOTHERMOMETER	yielded T°	
Monazite-Garnet after *Pyle & Spear, 2001*	436	
Monazite-Xenotime after *Gratz & Heinrich, 1997*	780	
Two feldspars after *Putirka, 2008*	810	
Ti in biotite after *Henry et al., 2005*	716	

Tab. 13 The table lists all the Geothermobarometer used in the present study. Pleas notice that the temperatures reported are average minimum temperatures and are not divided between north and south since only a pressure gradient is observed.

Gföhl gneiss and Moldanubian granulite, a common history?

This work is meant to give some more suggestions about the genesis of the Gföhl gneiss and to compare it with the granulite unit. Two approaches are made here (1) comparison of geochemical data of the Gföhl gneiss and the Moldanubian granulite in order to determine if both units were derived from the magmatic arc and (2) compare the petrological evolution of both units.

Comparison of geochemistry

The analyzed Gföhl gneiss and Moldanubian granulite are subalkaline, intermediate to acid with SiO_2 values of respectively 65.7 to 76.40 wt % and 62.9 to 76.7 wt % (*Schantl, 2015*). As shown by the TAS diagram after *Cox et al.* (1979) (Fig. 37) both show a compositional range from granite to granodiorite and a typical calc-alkaline trend (AFM diagram after *Irvine & Baragar, 1971*) (Fig. 38). Harker diagrams indicate the same negative correlation for SiO_2 vs. TiO_2, Al_2O_3, MgO; CaO and FeO whereas K_2O (as well as K_2O/Na_2O ratio) increases with increasing fractionation (Fig. 39; Fig. 40). LOI-values cover in Gföhl gneiss a wider range and are generally higher (0.3 - 2.85 wt %) than in Moldanubian granulite (mainly < 1 wt %) due probably to a stronger retrograde overprint and alteration that the gneiss experienced.

A trace elements comparison shows the same increase of Rb and negative correlation of Ba and Sr with increasing SiO_2 (Fig. 40). Zirconium is also characterized by the same low values and by a negative correlation with increasing SiO_2

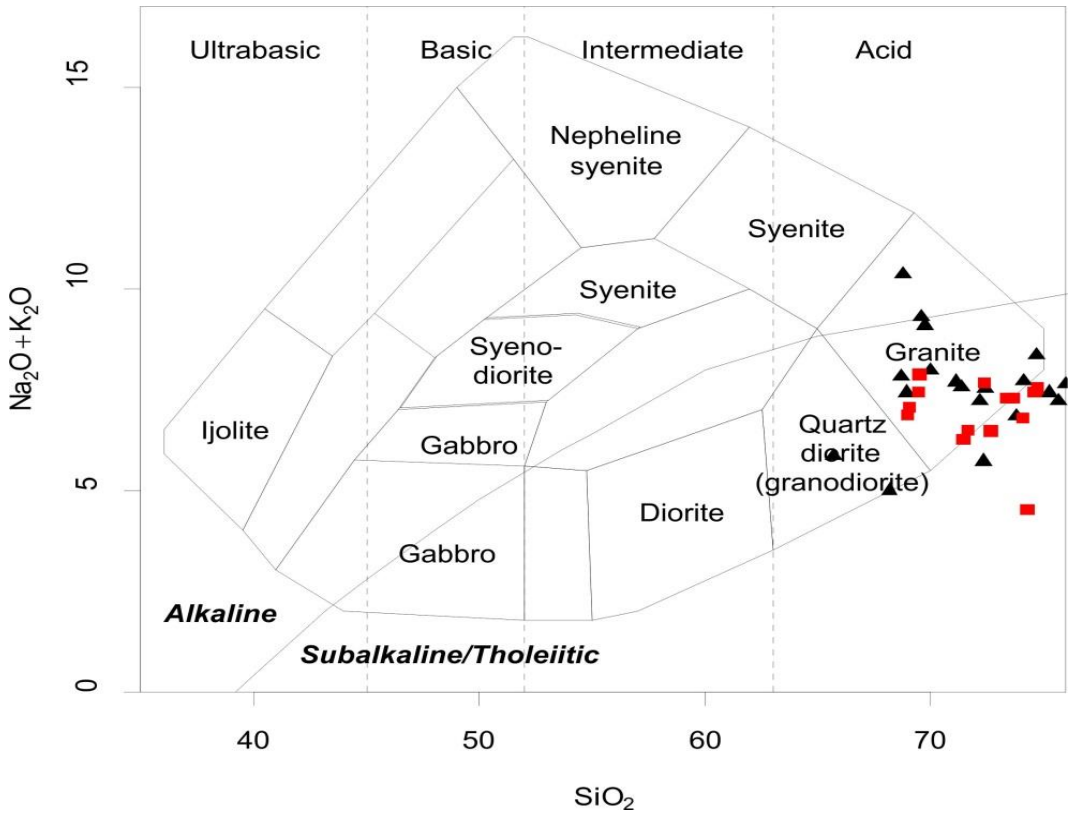

Fig. 37 TAS diagram (*Cox et al., 1979*) of representative samples of Moldanubian granulites (*Schantl, 2015*) and Gföhl gneiss. The red squares represent the granulites whereas the black triangles sampled gneisses.

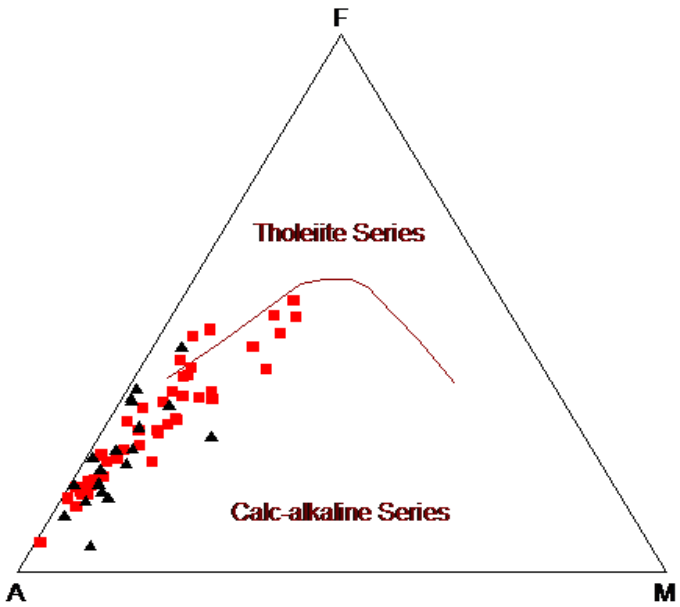

Fig. 38 AFM-diagram (*Irvine & Baragar, 1971*) of representative samples of Moldanubian granulites (*Schantl, 2015*) and Gföhl gneiss. The red squares represent the granulites whereas the black triangles sampled gneisses.

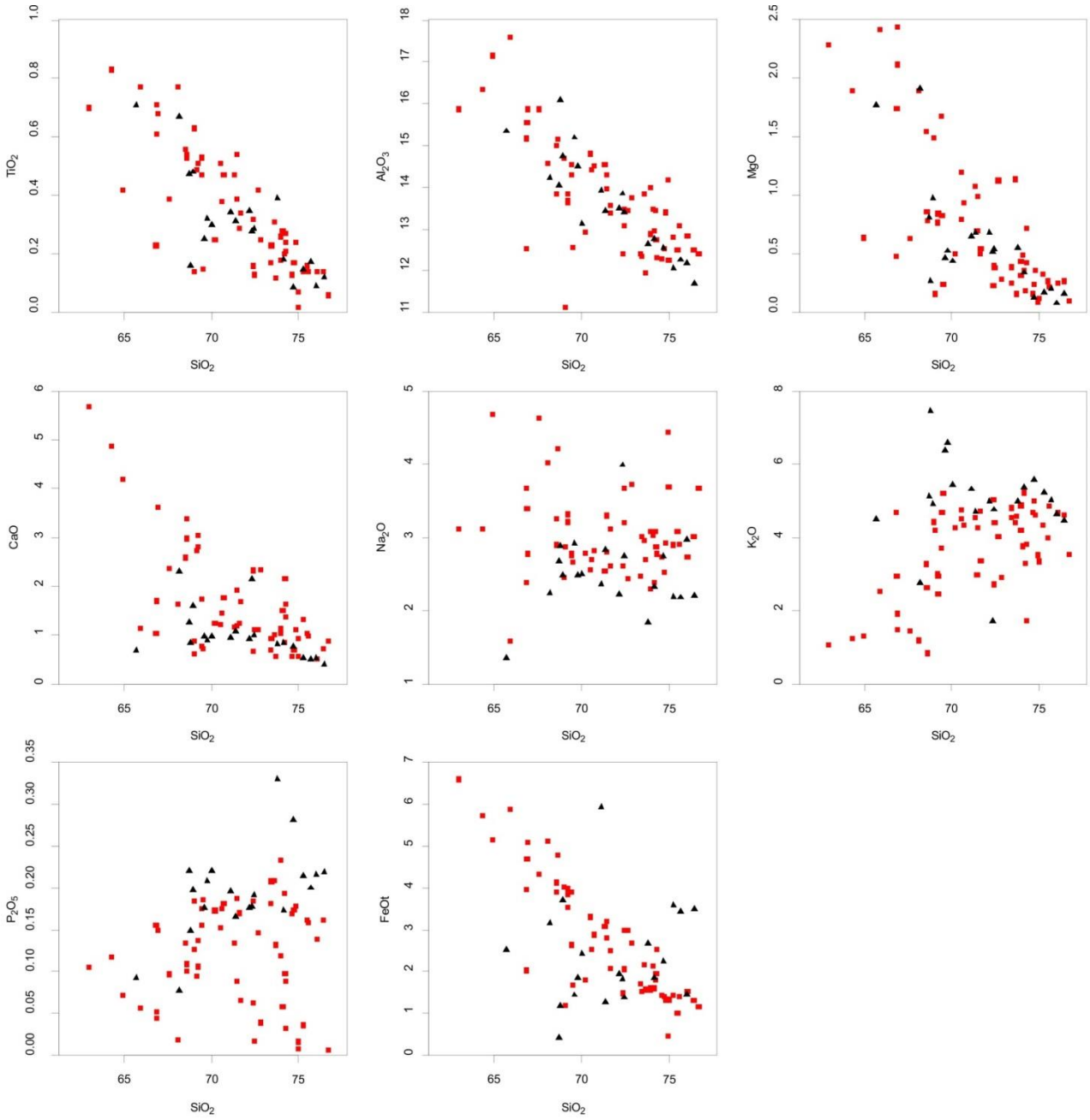

Fig. 39 Binary diagrams showing the major element oxides vs. SiO_2 (wt %). The black triangles indicate the Gföhl gneiss, the red squares symbolize the moldanubian granulites.

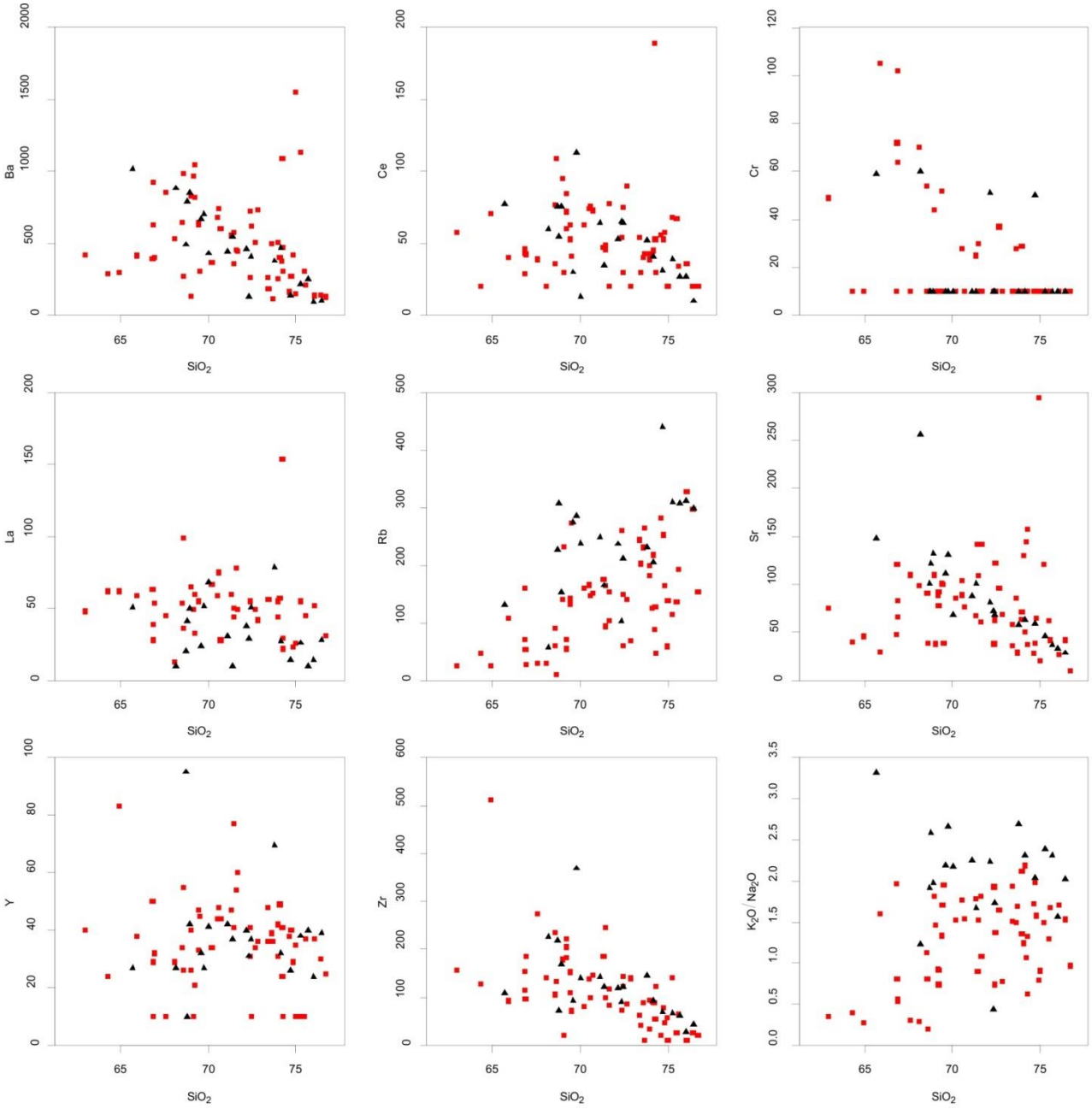

Fig. 40 Binary diagrams showing the trace elements and K2O/Na2O vs. SiO2 (wt %). The black triangles indicate the Gföhl gneiss, the red squares symbolize the moldanubian granulites.

Comparison of metamorphic evolution

A petrological investigation of the Moldanubian granulite (Dunkelsteinerwald-, Pöchlarn-Wieselburg- and Zöbing granulite bodies) of the Gföhl Nappe made by *Schantl* (2015) gives PT conditions of ~1050 °C and ~16 kbar which are significantly higher than the peak metamorphic conditions recovered in this study for the Gföhl gneiss, 750 ±50 °C and ~9 kbar.

The later MP-HT metamorphic overprint at ~760 °C and ~8 kbar experienced by the granulite during the exhumation stage (*Schantl, 2015*) is similar to the peak conditions recovered for the Gföhl gneiss leading to two potential scenarios for the evolution of the two lithologies.

1. Gföhl gneiss and Moldanubian granulite share a common evolution that is not seen anymore since diffusive processes during a Carboniferous HP-UHT event (Becker, 1996; Klötzli et al., 1999; Friedl et al., 2011) modified and largely obliterated the mineral phases. Gföhl gneiss is the product of the retrograde re-equilibration of the Moldanubian granulite during the exhumation to middle crustal levels (*Cooke & O´Brien*, *2001*).

In this case it could be appropriate to abandon the present tectonic distinction that separates Gföhl gneiss from Moldanubian granulite into two separate unit packages and group them under the same tectonic unit.

The petrological distinction (along with its nomenclature) between leucocratic Moldanubian granulite and Gföhl gneiss could also be reconsidered since the mineral assemblage as well as the whole rock chemistry is mostly identical (Fig. 37, Fig. 38, Fig. 39, Fig. 40). In the description of a hypothetical summarized lithology (e.g. leucocratic Moldanubian granulite) it should be noted that the mineral assemblage is constant (e.g. leucocratic granulites and Gföhl gneiss) as well as the metamorphic grade (granulite facies) but the texture differs from gneissic to strongly foliated.

2. Gföhl gneiss and Moldanubian granulites are derived from the same magmatic setting but do not share a common metamorphic evolution. The idea is that of two paths that have a similar shape but different P-T conditions (Fig. 41). As the continental margin of the Rheic Ocean was subducted under the avalonian continent (Late Devonian to Early Carboniferous after *Kroner et al., 2007*) the common protolith of granulite and gneiss was part of the syn-

accretionary wedge and was dragged into the subduction channel. The lower portion of it reached ideal conditions that determined granulite facies metamorphism, the shallower part underwent instead slighltly lower-grade metamorphism. Now, based on the pressure range obtained in this work for the Gföhl gneiss and on previous petrological investigations of the Moldanubian granulite (*Schantl*, *2015*) the depth of formation can be roughly estimated: assuming the geostatic gradient for a subduction zone proposed by *Xiao et al.* (2012) the depth of formation of the Gföhl gneiss (8.5-9 kbar) is 27-29 km whereas the depth of formation of the Moldanubian granulite (14-16 kbar) is 45.5-52 km. Both units were exhumed at middle to lower crustal levels (*Finger et al., 2007*). Gneiss and granulite were consequently tectonically juxtaposed. The overthrusting of the Moldanubian granulite on the Gföhl gneiss (and moreover the thrust-system observed within the Bohemian Massif) is due to extension determined by the slab break-off and consequent fast exhumation during the Viséan (*Kroner et al., 2007*). At this time (post 340 Ma) the Gföhl gneiss was strongly metamorphic overprinted and lost its original petrographic features.

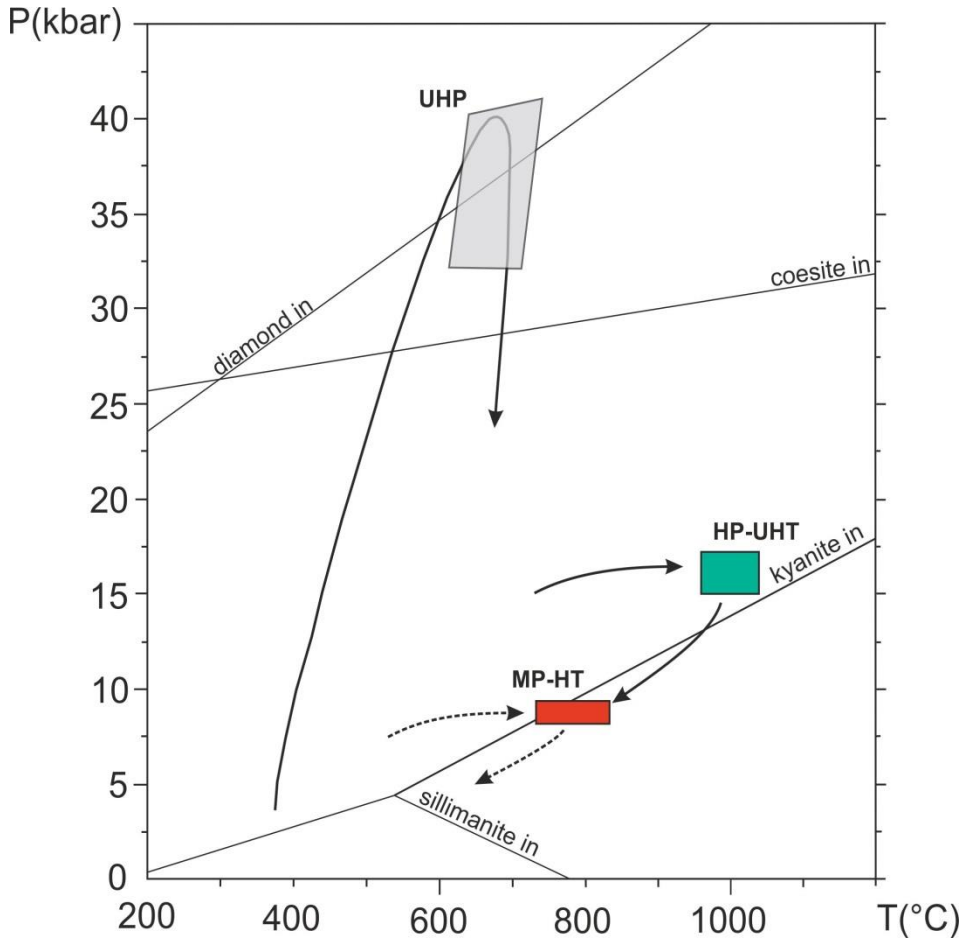

Fig. 41 Diagram showing an hypothetical PT evolution for the Gföhl gneiss (dashed line). As proposed in the discussion, the Gföhl gneiss could have followed a similar-shaped PT-path as the HP-UHT (UHT=Ultra-High Pressure) Moldanubian granulites (*Schantl, 2015*) at shallower depths. The path of both lithologies rejoins as the retrograde overprinting takes place. UHP-HT metamorphism (370 Ma, after *Kroner et al., 1988*)) is also depicted in Moldanubian granulites cropping out in the western sector of the moldanubian Zone (*Kutná Hora, Blanský les) in Czech Republic (Perraki and Faryad, 2014)*

REFERENCES

Benisek, A., Dachs, E. & Kroll, H. (2010), A ternary feldspar-mixing model based on calorimetric data: development and application. Contributions to Mineralogy and Petrology, 160, 327-337. http://dx.doi.org/10.1007/s00410-009-0480-8.

Burg, J. P., P. Bale, J. P. Brun, and J. Girardeau (1987), Stretching lineation and transport direction in the Ibero-Armorican arc during the Siluro-Devonian collision, Geodin. Acta, 1, 71–87.

Carswell, D.A. & O'Brien, P.J. (1993), Thermobarometry and geotectonic significance of high pressure granulites: examples from the Moldanubian Zone of the Bohemian Massif in Lower Austria. J. Petrol., 34, 427–459. http://dx.doi.org/10.1093/petrology/34.3.427 60.

Connolly, J.A.D. (2005), Computation of phase equilibria by linear programming: a tool for geodynamic modeling and its application to subduction zone decarbonation. Earth and Planetary Science Letters, 236, 524-541. http://dx.doi.org/10.1016/j.epsl.2005.04.033.

Cooke, R.A. (2000), High-pressure/temperature metamorphism in the St. Leonhard Granulite Massif, Austria: evidence from intermediate pyroxene-bearing granulites. Int. J. Earth. Sci., 89, 631-651. http://dx.doi.org/10.1007/s005310000123.

Cooke RA, O'Brien PJ (2001) Resolving the relationship between high p-T rocks and gneisses in collisional terranes: an example from the Gföhl gneiss-granulite association in the Moldanubian zone, Austria. Lithos 58:33–54

Cox, K. G., Bell, J. D., and Pankhurst, R. J. (1979), The interpretation of igneous rocks (p. 450). London: G. Allen and Unwin.

Dallmeyer, D., Franke, W. & Weber, K. (1995), Pre-Permian Geology of Central and Western Europe. Springer, Berlin, 579-593.

Dallmeyer, R.D., & Urban, M. (1998), Variscan vs Cadomian tectonothermal activity in northwestern sectors of the Teplá-Barrandian zone, Czech Republic: constraints from 40Ar/39Ar ages. Geologische Rundschau, 87, 94-106. http://dx.doi.org/10.1007/s005310050192.

de Capitani, C., and K. Petrakakis (2010), The computation of equilibrium assemblage diagrams with Theriak/Domino software, Am. Mineral., 95(7), 1006–1016, doi:10.2138/am.2010.3354.

Dudek, A. (1980), The crystalline basement block of the Outer Carpathians in Moravia: Bruno- Vistulicum. - Rozpr. Čs. Acad. Věd. Ř. mat přir. Věd, 90, 8, 1-85.

Dutch S., (1999), Exsolution, didactic material. Natural and Applied Sciences, University of Wisconsin - Green Bay

Elkins, L.T. and Grove, T.L. (1990), Ternary feldspar experiments and thermodynamic models. American Mineralogist, 75, 544–559.

Encyclopedia Britannica Online

Faryad, S., W. (2011), Distribution and Geological Position of High-/Ultrahigh-Pressure Units Within the European Variscan Belt: a Review

Fiala J., Fuchs G., Wendt J.I. (1995), Stratigraphy of the Moldanubian Zone. In: Dallmeyer RD, Franke W, Weber K. (eds) Pre-Permian Geology of Central and Eastern
Europe. Springer-Verlag, Berlin, pp 417–428.

Finger, F., Gerdes, A., Janousek, V., René, M., Riegler, G. (2007), Resolving the Variscan evolution of the Moldanubian sector of the Bohemian Massif: the significance of the Bavarian and the Moravo–Moldanubian tectonometamorphic phases. Journal of Geosciences, 52, 9–28.

Finger F., Krenn E. (2007), Three metamorphic monazite generations in a high-pressure rock from the Bohemian Massif and the potentially important role of apatite in stimulating polyphase monazite growth along a PT loop. Lithos 95: 103–115.

Finger F. (2015), Das Mineral Monazit ($CePO_4$): Der Frosch der sich in einen Prinzen verwandelt hat. Presentation held at University of Graz, December 2016.

Franke, W. (1984), Variszischer Deckenbau im Raume der Münchberger gneiss-masse, abgeleitet aus der Fazies. Deformation und Metamorphose im umgebenden Paläozoikum. Geotektonische Frosch., 68: 1-253.

Franke, W. (2000), The mid-European segment of the Variscides: tectono-stratigraphic units, terrane boundaries and plate tectonic evolution. Geol.Soc.London Spec.Publ., 179: 35-61.

Franz L. (2016), Geothermobarometrie - Vorlesungsunterlagen. Mineralogisch-Petographisches Institut, Universität Basel.

Frasl, G. (1968), The Bohemian Massif in Austria. - International Geological Congress XXIII Session, Guide to Exe. 32 C, Austria, 13-24.

Frasl, G. (1983), Einführung in die Geologie der Moravischen Zone. In Hock, V. et al.: Exk. der österr. Geol. Ges., 4-18.

Friedl G., McNoughton N., Fletcher I.R. and Finger F. (1998), New SHRIMP-zircon ages for orthogneisses from the south-eastern part of the Bohemian Massif (Lower Austria). Prag Acta Universitatis Carolinae, 42/2, 251-252.

Friedl, G., Cooke, R.A.; Finger, F., McNaughton, N.J., Fletcher, I. R. (2011), Timing of Variscan HP-HT metamorphism in the Moldanubian Zone of the Bohemian Massif: U-Pb SHRIMP dating on multiply zoned zircons from a granulite from the Dunkelsteiner Wald Massif, Lower Austria. Mineralogy and Petrology, 102, 63–75. http://dx.doi.org/10.1007/s00710-011-0162-x 62.

Fuchs G., (1971), Zur Tektonik des östlichen Waldviertels (N.Ö.). Verh. Geol. B.-A., 1971/3, 424–440, Wien.

Fuchs, G. (1976): Zur Entwicklung der Böhmischen Masse. Jb.Geol. B.-A., 119, 45–61, Wien.

Fuchs G. & Matura, A., 1980: Die Böhmische Masse in Österreich. In: Oberhauser, R. (Red.): Der geologische Aufbau Österreichs, 121–142, Wien (Geol. B.-A.).

Fuhrman, M.L. & Lindsley, D.H. (1988), Ternary-feldspar modeling and thermometry. American Mineralogist, 73, 201-215.

Gaidies, F., De Capitani, C., & Abart, R. (2008), THERIA_G: a software program to numerically model prograde garnet growth. Contributions to Mineralogy and Petrology, 155(5), 657-671.

Gerdes A, Friedl G, Parrish RR , Finger F (2003), High resolution geochronology of Variscan granite emplacement the South Bohemian Batholith. J Czech Geol. Soc. 48: 53–54.

Gratz, R. & Heinrich , W. (1997), Monazite-xenotime thermobarometry: Experimental calibration of the miscibility gap in the binary system CePO 4-YPO 4. - Amer. Miner., 82: 772-780.

Guidotti C.V.(1984) Micas in metamorphic rocks. In S.W. Bailey, Ed., Micas, vol. 13, p. 357–467. Reviews in Mineralogy, Mineralogical Society of America, Washington, D.C.

Henry D.J., Guidotti V.C. & Thomson A.J. (2005), The Ti-saturation surface for low to medium pressure metapelitic biotites: Implications for geothermometry and Ti-substitution mechanisms. *Amer. Mineralogist* 90, 316-328.

Hasalová P, Schulmann K, Lexa O, Štípská P, Hrouda F (2007), Origin of felsic migmatites by ductile shearing and melt infiltration: a new model based on quantitative microstructural analysis. J Metamorph Geol.

Hirsch D., Baldwin J., Perkins D., What are Pseudosections? From http://serc.carleton.edu/research_education/equilibria/pseudosections.html

Hoisch, T. D. (1990), Empirical calibration of six geobarometers for the mineral assemblage quartz + muscovite + biotite + plagioclase + garnet. Contributions to Mineralogy and Petrology 104 , 225.

Holland, T. & Powell, R. Contr. Mineral. and Petrol. (1991), 109: 265. doi:10.1007/BF00306484

Holland, T.J.B., Powell, R., 1998. An internally consistent thermodynamic data set for phases of petrological interest. J. Metamorph. Geol. 16 (3), 309-343.

Irvine, T.N., Baragar, W.R.A. (1971), A guide to the chemical classification of the common volcanic rocks. Can. J. Earth Sci. 8, 523–548.

Kossmat, F. (1927), Gliederung des varistischen Gebirgsbaues. Abhandlungen des Sächsischen Geologischen Landesamtes, 1, 1–39.

Kotkovă, J. (2007), High-pressure granulites of the Bohemian Massif: recent advances and open questions. Journal of Geosciences, 52, 45-71. http://dx.doi.org/10.3190/jgeosci.006.

Koziol, A.M., and Newton, Re. (1988), Redetermination of the anorthite breakdown reaction and improvement of the plagioclase-garnet-Al_2SiO_5,-quartz geobarometer. American Mineralogist, 73, 216-223.

Koziol, A.M. (1989), Recalibration of the gamet-plagioclase-AI2SiO5,-quartz (GASP) geobarometer and Applications for natural parageneses. EOS, 70, 493.

U. Kroner, T. Hahn, R.L. Romer, U. Linnemann (2007), The Variscan orogeny in the Saxo-Thuringian Zone—heterogenous overprint of Cadomian/Palaeozoic Peri-Gondwana crust in: U. Linnemann, R.D. Nance, P. Kraft, G. Zulauf (Eds.), The Evolution of the Rheic Ocean: From Avalonian–Cadomian Active Margin to Alleghenian-Variscan Collision. Geological Society of America Special Paper, 423, 153–172

Ledru, P., Lardeaux, J.-M. et al. (1989). Où sont les nappes dans le Massif Central français? Bulletin de la Société Géologique de France, 5, 605–618.

Matte, P. (1986), Tectonics and plate tectonics model for the Variscan belt of Europe. Tectonophysics 126, 329-374.

Matte, P. (1991), Accretionary history of the Variscan belt in Western Europe. Tectonophysics 196, 309-337.

Matura A. (1976), Hypothesen zum Bau und zur geologischen Geschichte des kristallinen Grunsgebirges von Südwestmähren und des niederösterreichischen Wald-viertels. Jb Geol B-A 119: 63–74

Matura A. (2003), Zur tektonischen Gliederung der variszischen Metamorphite im Waldviertel Niederösterreichs. Jb Geol B-A 143: pp 221–225

Matte, P. (2001), The Variscan collage and orogeny (480–290 Ma) and the tectonic definition of the Armorica microplate: a review. Terra Nova, 13: 122–128. doi:10.1046/j.1365-3121.2001.00327.x

Perraki, M. & Faryad, S.W. (2014), First finding of microdiamond, coesite and other UHP phases in felsic granulites in the Moldanubian Zone: Implications for deep subduction and a revised geodynamic model for Variscan Orogeny in the Bohemian Massif. Lithos, 202, 157-166. http://dx.doi.org/10.1016/j.lithos.2014.05.025

Petrakakis, K. (1997): Evolution of Moldanubian rocks in Austria: review and synthesis. Journal of Metamorphic Geology, 15, 203-222. http://dx.doi.org/ 10.1111/j.1525-1314.1997.00015.x

Putirka, K., *(2008) Thermometers and barometers for volcanic systems. In Putirka, K., and Tepley, F., Eds., Minerals, Inclusions and Volcanic Processes. Reviews in Mineralogy and Geochemistry, 69, 61–120.*

Pyle, J.M., Spear, F.S., Rudnick, R.L., McDonough, W.F., (2001). Monazite–xenotime–garnet equilibrium in metapelites and a new monazite–garnet thermometer. Journal of Petrology 42, 2083–2107.

Seston, R*,* Winchester, J.A*,* Piasecki, M.A.J*,* Crowley, Q.G*,* Floyd, P.A*., (*2000), A structural model for the Western-Central Sudetes: a deformed stack of Variscan thrust-bounded slices. J. Geol. Soc. London*,* 157*,* 1155–1167.

Schantl .P, (2015) Multistage Variscan metamorphism of the Moldanubian granulites from the Bohemian Massif (Austria). Unpublished MSc thesis, Institute of Earth Sciences of Graz.

Stosch, H.-G.; Lugmair, G.W. (1990), Geochemistry and evolution of MORB-type eclogites from the Münchberg Massif, southern Germany. Earth and Planetary Science Letters, 99, 230-249.

Suess, F.E. (1912), Die moravischen Fenster und ihre Beziehung zum Grundgebirge des hohen Gesenke. Denkschrift der kaiserlichen Akademie der Wissenschaft, Mathematisch-Naturwissenschaftliche Classe, 88, 541-631.

Suess, F.E. (1926), Intrusionstektonik und Wandertektonik im variszischen Grundgebirge. Geologiska Föreningen i Stockholm Förhandlingar, *48*, 607-609. http://dx.doi.org/10.1080/11035892609455322

Timmermann, H., *Štědrá*, V., Gerdes, A., Noble, S.R., Parrish, R.R., Dörr, W., (2004), The problem of dating high-pressure metamorphism: a U-Pb isotope and geochemical study on eclogites and related rocks of the Mari*á*nské L*á*zn*ě* Complex, Czech Republic. J. Petrol. 1311-1338.

Timmermann, M.J. (2008), Palaeozoic Magmatism. In: T.McCann T. (Ed.), The geology of Central Europe. Vol. 1: Pre-cambrian and Palaeozoic. The Geological Society of London, 665-748.

Tollmann (1982), Grossräumiger variszischer Deckenbau im Moldanubikum und neue Gedanken zum Variszikum Europas. Geotekt Forsch 64: 1–91

Tollmann A. (1995), Das Ausmass des variszischen Deckenbaues im Moldanubikum. Krystalinikum 18:117–132.

von Quadt A, Gebauer D (1993), Sm-Nd and U-Pb dating of eclogites and granulites from the Oberpfalz, NE Bavaria, Germany. Chem Geol 109: 317–339.

Waldmann, L. (1951), Das außeralpine Grundgebirge Österreichs. - in: F.X. Schaffer (Hg.): Geologie von Österreich, 2. Aufl., 1-105, Verl. Deuticke, Wien.

White, RW, Powell, R & Holland, TJB (2007), Progress relating to calculation of partial melting equilibria for metapelites. Journal of Metamorphic Geology, 25, 511-527. (from tx-NCKFMASHTO.txt in tc330 download.)! approximation, model in fsol fails Gibbs-Duhem.

Whitney, D.L. & Evans, B.W. (2010), Abbreviations for names of rock-forming minerals. American mineralogist, 95, 185. http://dx.doi.org/10.2138/am.2010.3371.

Y. Xiao, S. Lavis, Y. Niu, J.A. Pearce, H. Li, H. Wang, J. Davidson (2012), Trace-element transport during subduction-zone ultrahigh-pressure metamorphism: evidence from western Tianshan, China Geol. Soc. Am. Bull., 124, 1113–1129.

Zeitlhofer H, Schneider D, Grasemann B, Konstantin P, Thöni M (2013), Polyphase tectonics and late Variscan extension in Austria (Moldanubian Zone, Strudengau area). Int. J. Earth. Sci. 103:83–102.

DIGITAL APPENDIX